学位論文

Crystal size, photoluminescence and electroluminescence optimization of $MAPbBr_3$ perovskite microcrystals

($MAPbBr_3$ ペロブスカイト微結晶の結晶サイズ、フォトルミネッセンスおよびエレクトロルミネッセンスの最適化)

Division of Environmental Materials Science

Graduate School of Environmental Science

Hokkaido University

Japan

Dong Zhang

March 2024

Acknowledgment

I would like to express my sincere gratitude to my supervisor Professor Vasudevan Pillai Biju for providing guidance and support throughout my doctoral research. I am also thankful to Associate Professor Yuta Takano and Assistant Professor Takuya Okamoto for their support and active discussions. I thank Mrs. Atsuko Fujii for her administrative assistance. I also thank my lab members for their active discussion, valuable support and friendship. I thank Hokkaido University for providing me with a DX doctoral scholarship.

Finally, I express thanks to my parents for their constant support and love.

Abstract

Recently, lead halide perovskites are the most attractive semiconductor materials for light-harvesting and light-emitting applications, which is attributed to their excellent properties, such as high photoluminescence quantum yield, large absorption coefficient, low formation energy, and tunable bandgap. However, there are still issues limiting its large-scale applications, like instability and efficiency roll-off. In this thesis, I mainly focus on the study of isotropic and high-quality perovskite microcrystal synthesis, light-induced ion migration and its effect on electroluminescence blinking, and time-resolved electroluminescence of $MAPbBr_3$ microcrystals. The thesis is summarized in five chapters. In Chapter 1, I introduce the general information about halide perovskite. First, I introduce the structure of one unit cell, chemical compositions and stability factors. Following, I introduce different size halide perovskite synthesis methods, including micro-sized single crystal, nanocrystals and quantum dots. Then I introduce the characteristics of halide perovskite, including optical properties, bandgaps, charge carrier dynamics and blinking. Finally, I introduce applications of halide perovskites, especially to solar cells and light-emitting diodes. I also present my study motivation. In chapter 2, I introduce the materials, sample preparation methods and instruments I used throughout the studies. I show the synthesis the $MAPbBr_3$ microcrystals by various methods, such as room temperature crystallization (RTC), anti-solvent vapor-assisted crystallization (AVC), inverse temperature crystallization (ITC), modified-ITC and blade-coating methods. I investigate the properties of the microcrystals using optical microscopy and fluorescence microscopy. I study the photoluminescence and electroluminescence blinking of perovskite microcrystals using single particle micro spectroscope, and the photoluminescence and electroluminescence decays by time-resolved photoluminescence and electroluminescence spectroscopy. In chapter 3, I demonstrated the synthesis of isotropic high quality $MAPbBr_3$ microcrystals. I investigate the role of an additive *N*-Cyclohexyl-2-pyrrolidone and reaction temperature on the crystal size, shape, quality,

and density. I also discuss the crystal nucleation mechanism and crystal growth kinetics. Finally, I expand the modified ITC method to various types of halide perovskites. In chapter 4, I investigate the light-soaking effect on the photoluminescence lifetime and electroluminescence blinking of $MAPbBr_3$ microcrystals, the ON and OFF probability distribution of electroluminescence blinking statistics has been studied. The mechanism of light-induced halide ion migration and trap healing is correlated with the electroluminescence intensities and photoluminescence lifetime. In chapter 5, I investigate the time-resolved electroluminescence of $MAPbBr_3$ microcrystals. First, I measure the optical spectra and electroluminescence decay of commercial blue, green and red LEDs, and confirm the instrument reliability for time-resolved electroluminescence measurements. Then, I study the photoluminescence spectra, electroluminescence, and photoluminescence decays of $MAPbBr_3$ microcrystals. Finally, I investigate the influence of MABr treatment on electroluminescence and photoluminescence decays of $MAPbBr_3$ microcrystals, where Br vacancies are filled. The mechanism of halide ion vacancy filling enhanced electroluminescence and photoluminescence decays increase are discussed.

Abbreviations and symbols

AVC	Anti-solvent vapor-assisted crystallization
Å	Angstrom
τ_{av}	Average photoluminescence lifetime
BSSG	Bottom-seeded solution growth
CHP	*N*-Cyclohexyl-2-pyrrolidone
CBM	Conduction band minimum
°C	Degree Celsius
DCM	Dichloromethane
DMSO	Dimethyl sulfoxide
DMF	*N, N*-Dimethylformamide
EL	Electroluminescence
EMCCD	Electron-multiplying charge-coupled device
EIL	Electron injection layer
EQE	External quantum efficiency
EBL	Electron blocking layer
fs	Femtosecond
GBL	Gamma-butyrolactone
HI	Hot injection
ITC	Inverse temperature crystallization
ITO	Indium tin oxide

k_{nr}	Rate constant of nonradiative relaxation
k_r	Rate constant of radiative relaxation
LEDs	Light-emitting diodes
LHP	Lead halide perovskite
MABr	Methylammonium bromide
MCs	Microcrystals
MHP	Metal halide perovskite
M	Molar
NCs	Nanocrystals
OPA	Optical parametric amplifier
ODE	1-Octadecene
ps	Picosecond
PL	Photoluminescence
PCBM	(6,6)-Phenyl-C_{61}-butyric acid methyl ester
PEDOT:PSS	Poly(3,4-ethylenedioxythiophene)-poly(styrenesulfonate)
PeLEDs	Perovskite light-emitting diodes
PMMA	Polymethyl methacrylate
PCE	Power conversion efficiency
RTC	Room temperature crystallization
s	Second
SOC	Spin orbit coupling
T	Temperature

TCSPC	Time-correlated single photon counting
TRPL	Time-resolved photoluminescence
TREL	Time-resolved electroluminescence
TCO	Transparent conductive oxides
VBM	Valence band maximum
TSSG	Top-seeded solution growth
Vis	Visible
VBM	Valence band maximum

Table of contents

Chapter 1

Introduction

Abstract

Halide perovskites have been the most likely material to replace traditional materials as the next generation of photovoltaic and electronic devices. This is determined by its cost-effective synthesis and excellent optoelectronic properties. There are many application fields for halide perovskite material, but solar cells are the most investigated and promising applications. Beyond that, due to the demand for high-efficiency and low-price light-emitting diodes materials, researchers have been investigating halide perovskite-based light-emitting diodes for almost ten years. In addition, researchers have expanded its application to photodetectors, flexible optoelectronic devices, pressure-induced emission devices and lasers. Halide perovskite can be synthesized by a simple solution method in a few minutes into film, single crystal, nanocrystal, quantum dots. Halide perovskite-based devices have obtained great photoluminescence and electroluminescence efficiencies, however, due to the intrinsic and extrinsic properties, the stability and performance efficiency issues still block its large-scale applications. In this chapter, I introduce the fundamental information, chemical structure, synthesis method, optoelectronic property, applications, and unsolved issues of halide perovskites.

1.1 General introduction

Perovskites are materials that have a formular ABX_3. The BX_6 octahedra is shared by an A-site cation, which occupies the space between the BX_6 octahedra (Figure 1.1). It was discovered by Gustav Rose in 1839 as a $CaTiO_3$ mineral material and named after the Russian mineralogist Lev Perovski. When the A site is an inorganic ion, such as Cs^+, it is called inorganic perovskite. In the case of organic ions, such as methylammonium (MA^+) or formamidinium (FA^+), these are called hybrid perovskites. The B site is a divalent cation, such as Pb^{2+} or Sn^{2+}, and the X site is usually occupied by a halide ion (Cl^-, Br^-, or I^-). Owing to the cost-effective, simple synthesis, and distinctive optoelectronic features, metal halide perovskites have become more popular in recent years.

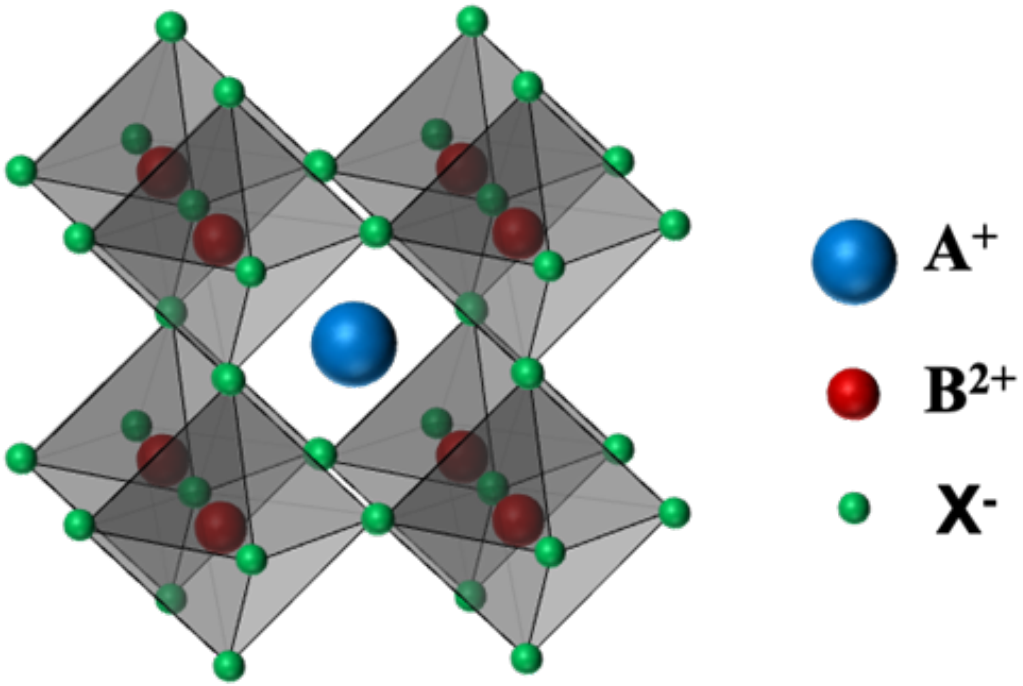

Figure 1.1. A halide perovskite unit cell.

The stability of the perovskite structure can be calculated by Goldschmidt tolerance factor (t) and octahedra factor:

$$t = \frac{r_A + r_X}{\sqrt{2}(r_B + r_X)}$$

In this equation, r_A, r_B and r_X are the ionic radii of A, B cations and X halogen ions, respectively.

$$\mu = \frac{r_B}{r_x}$$

The t factor is a proper value in the range of 0.76 to 1.13, and the μ factor is 0.44 to 0.90 for the stable perovskite and octahedra structure, respectively.

1.2 Synthesis of halide perovskites

1.2.1 Crystallization mechanism

Crystallization is a fundamental process in forming crystals, which are solid materials with a repeating, ordered atomic or molecular structure. It is the initial step in the crystallization process, where small clusters of atoms, ions, or molecules come together to form the nucleus of a crystal. Once the nucleus is formed, it can continue to grow as more particles join it, ultimately resulting in the growth of a larger crystal. The crystallization processes of materials typically include nucleation and growth.[1] In the case of halide perovskites (HPs), through the computation of the energy disparity between the fundamental constituents in their independent, unbound states and their aggregated form within a solid crystal. Uniform nucleation is when the components come from the entire parent phase to form a second phase, called uniform nucleation. It is unaffected by contaminants or exterior surfaces. Non-uniform nucleation occurs at preferred locations, such as surface, phase boundaries, or impurities.[2] Usually, the HPs crystallization takes place in a molten,[3] vapor system,[4] and solution system.[5]

1.2.2 Synthesis of halide perovskite single crystals

The inverse temperature crystallization (ITC) method relies on an inverse solubility of solute in particular solvents when the temperature arises while the solubility of solute declines.[6-13] Figure 1.2a describes an ITC method schematic diagram. Since inverse solubility causes crystallization in some organic materials, ITC technique heavily relies on temperature because of the inverse solubility of the solute in solvents. This method's growth process balances precipitation and dissolution. The solvent must be properly selected to generate a nice single crystal. For instance, Gamma-butyrolactone (GBL), dimethyl sulfoxide (DMSO) and *N, N*-dimethylformamide (DMF) are shown to be the most effective solvents for $MAPbBr_3$, $MAPbI_3$, and $MAPbCl_3$ correspondingly.[14] Utilizing this procedure, Saidaminov et al.[15] could build single-crystal perovskites as shown in Figure 1.2b. The inverse solubility phenomenon of perovskites is evaluated and confirmed by measuring it in various solvents and temperatures. DMF and GBL are identified as appropriate solvents to demonstrate the inverse solubility of bromide and iodine-based perovskites.

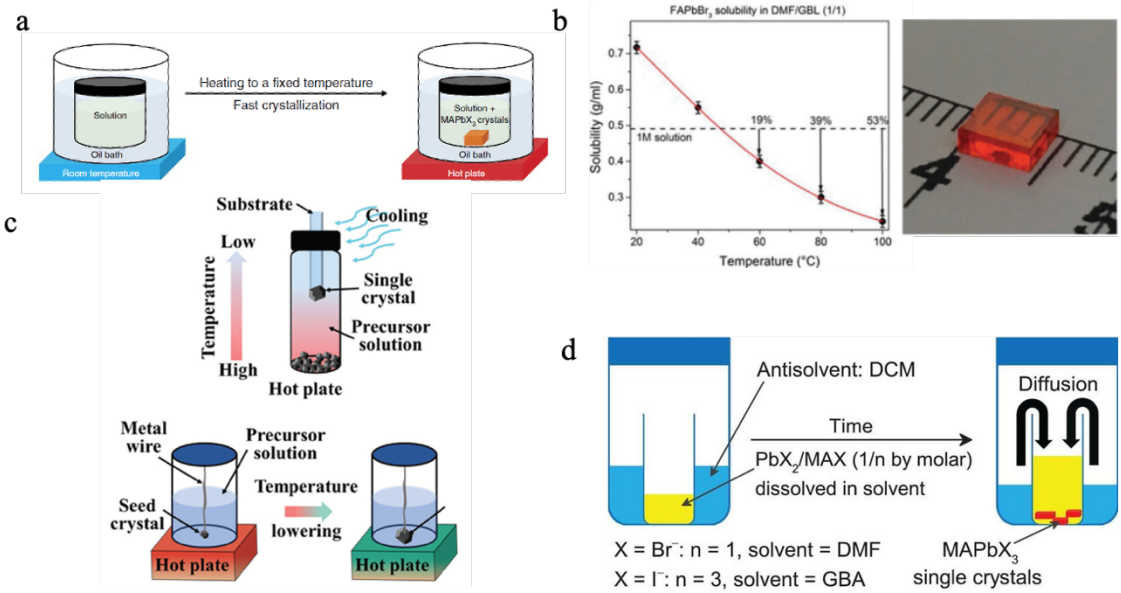

Figure 1.2. (a) (b). The scheme of ITC method and inverse solubility of $FAPbBr_3$ in DMF/GBL.[15] (c) The scheme of cooling method.[17] (d) The scheme of anti-solvent vapor assisted method.[16]

The antisolvent vapor-assisted crystallization (AVC) method was initially described by Shi and colleagues[16], who also successfully synthesized high-quality, millimeter-sized $MAPbBr_3$ and $MAPbI_3$ SCs. They employed dichloromethane (DCM), an antisolvent fully insoluble for precursors. To the precursors, MABr and $PbBr_2$ are mixed in DMF at a molar ratio of 1:1 and MAI and PbI_2 at a 3:1 molar ratio in GBL. The beaker containing the precursor is put in a bigger container containing the antisolvent. Subsequently, the system is sealed, allowing the DCM vapor to gradually dissolve into the mixture due to its effective miscibility with DMF or GBL. As illustrated in Figure 1.2d, adding DCM causes crystallization since it uses up the solvent and raises the concentration of precursors past the point at which they can no longer dissolve in solution. $PbBr_2$ separates more quickly than MABr when the antisolvent ingests into DMF. This nonequilibrium precipitation builds up, creating a nonstoichiometry single crystal surface that makes the crystal opaque.

When a hot saturated precursor solution is gradually cooled down, the solubility of solute is decreased and a single crystal forms. This process depends on temperature reduction, which decreases solubility. Dang claims that when a solution's temperature is lowered from around 100 °C to room temperature, $MAPbX_3$ single crystals begin to precipitate out in an equimolar ratio of MA, Pb^{2+}, and aqueous HX. The bottom-seeded solution growth (BSSG) usually utilizes the slow-cooling method to prepare bulk crystals, and the top-seeded solution growth (TSSG) usually utilizes the slow-cooling method. As shown in Figure 1.2c, TSSG expedites the process of producing large single crystals by positioning the seed crystal on the solution’s surface, in contrast to BSSG, where the seed crystal is suspended in a saturated solution at the container's bottom.[17]

1.2.3 Synthesis of halide perovskite nanocrystals

The hot-injection (HI) method includes the precursor injection within a short time into a heated mixture containing the rest of the ligands, precursors, and solvents.[18-19] This

method is divided into nuclei formation and crystal growth. The HI technique usually facilitates the fine size particles, like nanocrystal and quantumdots.[20] Immediately after

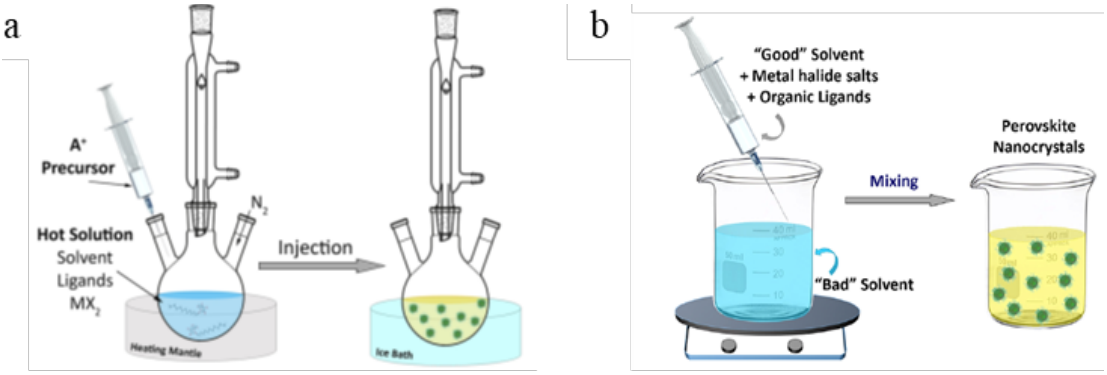

Figure 1.3. Synthesis method scheme of (a) Hot-injection and (b) LARP methods.[18]

injection, there is a swift burst of nucleation and simultaneous generation of tiny nuclei. During the nucleation process, due to the rapid consumption of single nuclei, the formed nuclei keep growing, preferably without forming new nuclei. This causes the gradual improvement of the nanocrystal, which is studied in a unique size range. It occurs when the reaction is halted while still within the size-focusing phase or when there is an ample supply of nuclei.[21] The essential characteristics that allow for size and size-distribution, controlling of nanocrystals are, surfactants ratio to precursors, injection temperature, reaction speed, and precursor concentration. To be able to produce the colloidal cesium halide perovskite nanocrystals ($CsPbX_3$, X = Cl, Br, and I), in 2015, Protesescu et al. expanded the hot-injection method by introducing Cs-oleate to a heated solution containing PbX_2 (X = Cl, Br, I). These chemicals are functionalized as the origins of Pb^{2+} and X, followed by the addition of acids, amines, and octadecene. This synthesis yielded $CsPbX_3$ nanocrystals (Figure 1.3a).

In the ligand-assisted reprecipitation (LARP) method for perovskite synthesis, the necessary precursor chemicals were first be dissolved in a suitable polar solvent, like DMSO, DMF, etc. (Figure 1.3b), before being mixed with a suitable solvent, such as toluene or hexane. In the LARP technique, the chemicals MX_2 (M = Pb, Sn, etc.), CsX, MAX, and FAX are frequently utilized, in which X denotes Cl, Br, and I. Combining the

two solvents leads to a supersaturation reaction, triggering the formation and proliferation of perovskite nanocrystals. The advantage of the LARP synthesis method is it can be performed in ambient air using a relatively simple procedure, in contrast to the hot-injection approaches. This implies that LARP can be rapidly applied, facilitating the mass production of metal halide perovskite nanocrystals.[22-24] In 2012, Papavassiliou et al. dissolved $MAPbX_3$ (X = Br, Cl, or I) and other salts in DMF or other solvents. Subsequently, they introduced the resulting solutions into toluene or toluene/polymethyl methacrylate by dropping them.[25] They saw the emergence of luminescent nanocrystals with diameters between 30 and 160 nm with PL intensities significantly higher than those predicted for the bulk $MAPbX_3$. After decades, the LARP method was applied to synthesis organic-inorganic $MAPbX_3$ NCs, followed by expanding to ABX_3 NCs (A = MA, FA, or Cs; B = Pb, Sn, Bi, or Sb; X = Cl, Br, or I).

1.3 Characterization of halide perovskites

1.3.1 Optical properties

Halide perovskites display a tunable emission wavelength by varying halide compositions and exhibit a singular peak within the UV–vis absorption and PL spectra (Figure 1.4a,b). The single-halide $FAPbX_3$ (X = Cl, Br, I) nanocrystals demonstrate a blue shift in both the optical absorption wavelength and emission bands compared to bulk materials. This shift can be attributed to the quantum size effect, as illustrated in Figure 1.4b. While $FAPbCl_3$ shows a PL quantum yield (PLQY) of less than 1%, $FAPbI_3$ and $FAPbBr_3$ nanocrystals after purification in toluene show higher PLQYs. The efficiency of mixed halide samples, such as $FAPbCl_{1.5}Br_{1.5}$ or $FAPbBr_{1.5}I_{1.5}$ NCs also shows a high PLQYs.

Additionally, several factors influence the bandgap of LHPs, such as crystal phase, octahedral tilt, temperature, pressure, and crystal size. While the Pb-X-Pb dihedral angle rises, the A-site cation size also increases, and the octahedral tilt becomes apparent. For instance, when FA^+ replaces Cs^+, the Pb-I-Pb angle rises from 153.2 to 179.9°.[26] Due to

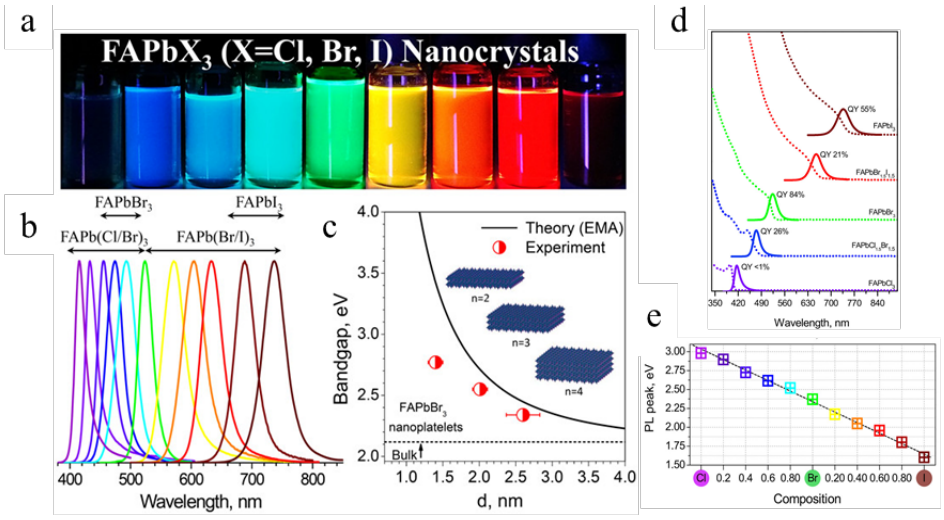

Figure 1.4. Characteristics of $FAPbX_3$ colloidal PNC solutions. (a) Photoexcited luminescence image of halide perovskite solution. (b) The tunable wavelength with bromide ratio variation in mixed halide perovskite. (c) Comparison between the theoretical and experimental band gap of $FAPbBr_3$ nanoplatelet in relation with thicknesses. (d) Absorption and PL spectra. (e) Compositional PL tuning diagram.[28]

decreased orbital overlapping and an increase in the bandgap, the octahedral tilt is also to blame for reducing the weakness of the spin-orbit coupling (SOC). The crystal structure is a four-direction square summation cube (or other aspects), and the change is the guiding octahedron and the diagonal two factors. Most of the time, the cubic phase is stable for LHPs, where the strong SOC minimizes the octahedral tilt.

1.3.2 Bandgaps

The band structures and the density of the state mainly control the optical characteristics of halide perovskites. It is, therefore, vital to investigate their electronic structure abnormalities, dimensionality, and material composition to enhance optoelectronic applications.[27-29] By modifying the structural framework, it becomes feasible to alter the predominant optoelectronic features of halide perovskites, including charge carrier lifetime, mobility, recombination kinetics, and carrier concentration. For the bandgap

formation of halide perovskites, the CBM is created by bonding the 6p-orbitals of Pb and the s- and p-orbitals of the halide. The VBM is created by the 6p- and 6s-orbitals of Pb and the s- and p-orbitals of the halide. The bandgaps of these materials can be easily tuned by varying the halide ratio. Figure 1.5a shows the energy level of the lead halide perovskite band-edge.

Halide perovskites are known for their well-defined direct band-gap structure. However, recent observations of a noncentrosymmetric lattice have suggested the possibility of Rashba or Dresselhaus band splitting in these materials.[30] In the case of carrier inter exchange reaction is the leading reaction, halide perovskites don't show

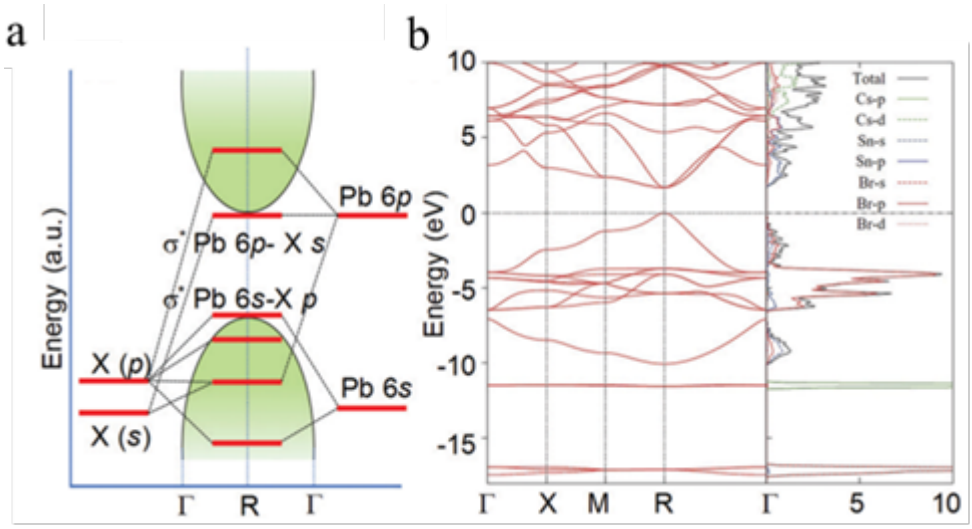

Figure 1.5. (a) Band-edge states of lead halide perovskites. (b) partial density of states and band structure of $CsSnBr_3$ perovskite.[42]

obvious quantum confinement, and the attainment of exciton states with values such as 0 or 1 can be largely attributed to the Rashba effect, resulting from inversion symmetry breaking. This spin-orbital coupling, which differentiates exciton states into singlet and triplet levels, is induced by the strong momentum-dependent interaction between the lead atom and the heavy nucleus.[31] Figure 1.5b shows that lead-free perovskites resemble lead halide perovskites of the band-edge structure. For example, the CBM is primarily composed of 5p-orbitals of Sn. Still, the VBM antibonding state consists of 4p-orbitals of

Br and 5s orbitals of Sn in $CsSnBr_3$ perovskite cubic crystal.[32] In this scenario, the CBM is initially triple degenerate, even without assistance from SOC, while the VBM remains nondegenerate. When a significant SOC is introduced, the crystal field splitting in CBM is disrupted, leading to the emergence of spin-orbit split doublet and quadruplet states. Optical transitions from the VBM to these spin-orbit split states and quadruplet states result in the favorable optical absorption characteristics of halide perovskites.

1.3.3 Charge carrier dynamics

When perovskite materials absorb light, the incident photons elevate charge carriers to higher energy levels, leaving the ground state with a hole. The optoelectronic characteristics of the perovskite depend on what happens to these charge carriers. Depending on the composition of the material, the photogenerated charge carriers may function as free carriers or excitons. Generating free carriers with extremely low binding energies is preferred for solar cell applications. In contrast, excited-state species with large exciton binding energies will increase the likelihood of radiative relaxation for light-emitting devices.

Figure 1.6 shows different recombination ways of charge carriers. The following represents the recombination rate equation with a charge carrier density of n (t). Here, it is considered that free carriers are created following photo- or electro-excitation.

$$\frac{dn}{dt} = -k_3 n^3 - k_2 n^2 - k_1 n$$

where k_1 is the rate constant for excitonic recombination or trap-assisted recombination, two types of monomolecular recombination. The concentration of any of the two species is the only factor affecting this recombination. The rate constant for an electron-hole pair-involving bimolecular recombination is k_2. The Auger recombination rate constant is called k_3. There are numerous species and phases in the Auger process. The effectiveness of these processes in applications such as lasers, LEDs, or solar cells depends on how much each contributes the others.

The three recombination processes combine to provide the total rate constant r(n), which is known to have an impact on the diffusion length, L_D as follows:

$$L_D(n) = \sqrt{\frac{\mu k_B T}{\gamma(n) e}}$$

where e is the electronic charge, T is the temperature, k_B is the Boltzmann constant, and μ is the mobility of charge carriers.

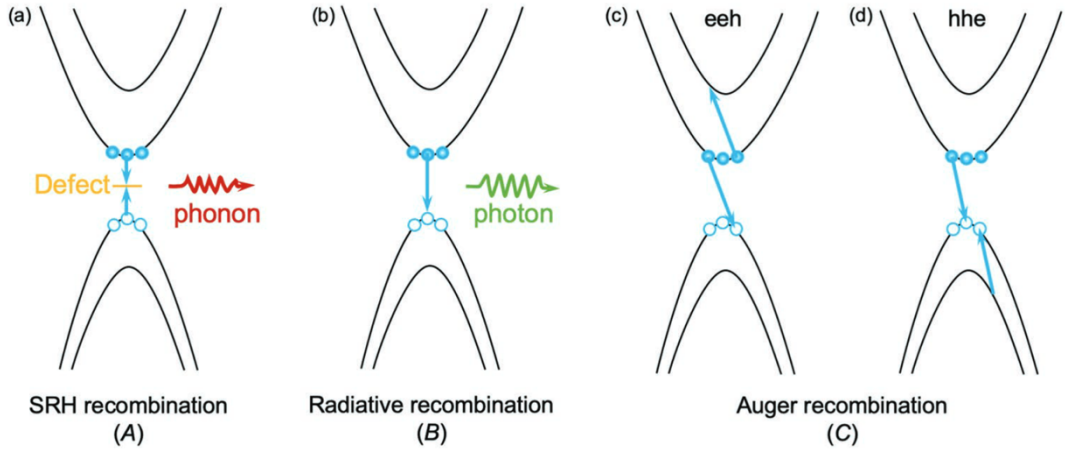

Figure 1.6. Several schemes of recombination processes. (a) Shockley-Read-Hall (SRH) recombination. (b) radiative recombination. (c) (d) Auger recombination.[33]

1.4 Halide perovskite blinking

1.4.1 Electroluminescence blinking

EL blinking from $MAPbBr_3$ single crystals is reported by Nguyen et al.[34] The single-crystal is fabricated by a cast-capping method between two ITO glasses. Figure 1.7a depicts the EL blinking images as determined from a $MAPbBr_3$ single crystal with increased bias from 2 to 4 V. Figure 1.7b shows the EL trajectories obtained from $MAPbBr_3$ single crystal. The intermittent emission behavior in EL has been suggested to be possibly explained by the entrapment of charge carriers in sub-bandgap trap states. These trap states may form at the surface or boundary of the crystal. The conflicting of

radiative and nonradiative processes produce EL blinking.

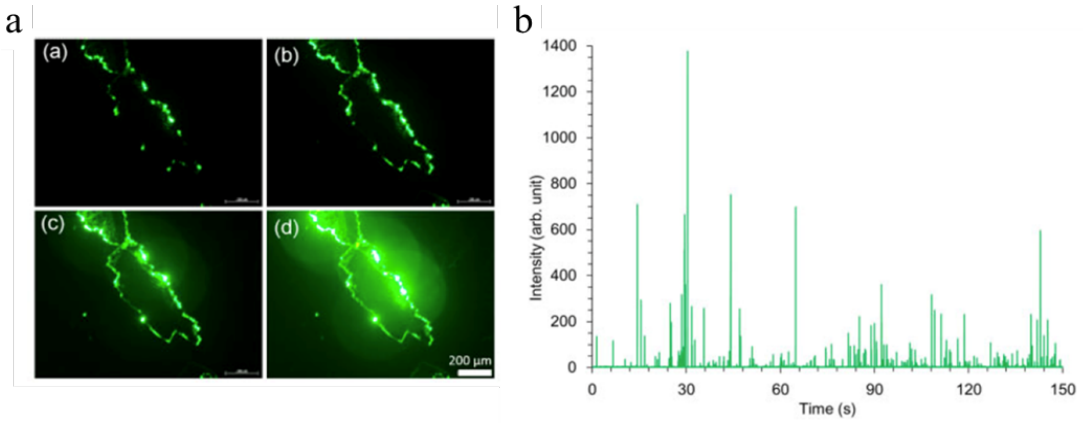

Figure 1.7. (a) A vivid green luminescence is observed in the single-crystal $MAPbBr_3$ under increasing bias voltage, ranging from 2 to 4 V. (b) A time profile displaying EL blinking, measured at a wavelength of $\lambda = 549.4$ nm.[34]

Vacha and colleagues publish an other research from $CsPbBr_3$ nanocrystal aggregates on EL blinking.[35] In this case, EL blinking behavior results from charge carriers funneling to big nanocrystals and recombining with one another. Here, the carrier recombination's particle-selective nature results in an EL blinking process. Figure 1.8a displays the EL trajectories obtained from the nanocrystal aggregates, and Figure1.8b displays the trajectories of aggregates at different excitation modes.

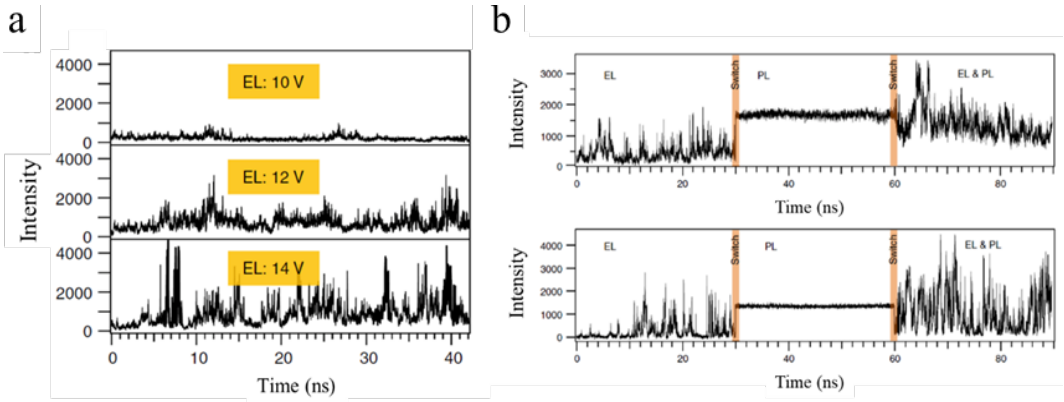

Figure 1.8. (a) EL from $CsPbBr_3$ nanocrystal aggregates at various voltages. (b) Time-traces of emission intensity captured from two distinct single aggregates while switching between excitation modes.[35]

1.4.2 Photoluminescence blinking

Nirmal et al. investigate the initial observation of the PL blinking phenomenon while studying isolated CdSe NCs under steady-state laser excitation circumstances.[36] A fluorescent image of a single 21-Å-radius CdSe nanocrystal placed in a thin polyvinylbutyral film at room temperature is shown in Figure 1.9a. The nanocrystal emission lifetimes discretely flip on and off, and their poorer quantum yield compared to neutral nanocrystals cause the streaks in the image that result from raster scanning the sample over a diffraction-limited laser spot. They note that the ionization rate-dependent average on period scales linearly with intensity. In Figure 1.9b, the trace of fluorescence intensity plotted against the time of a "bare" particle and an overcoated particle (with seven monolayers of ZnS) are contrasted at the same excitation intensity. Due to ZnS's greater bandgap than CdSe (by about 2 eV), it should be able to effectively block ionization and neutralization and passivate potential surface trap sites.

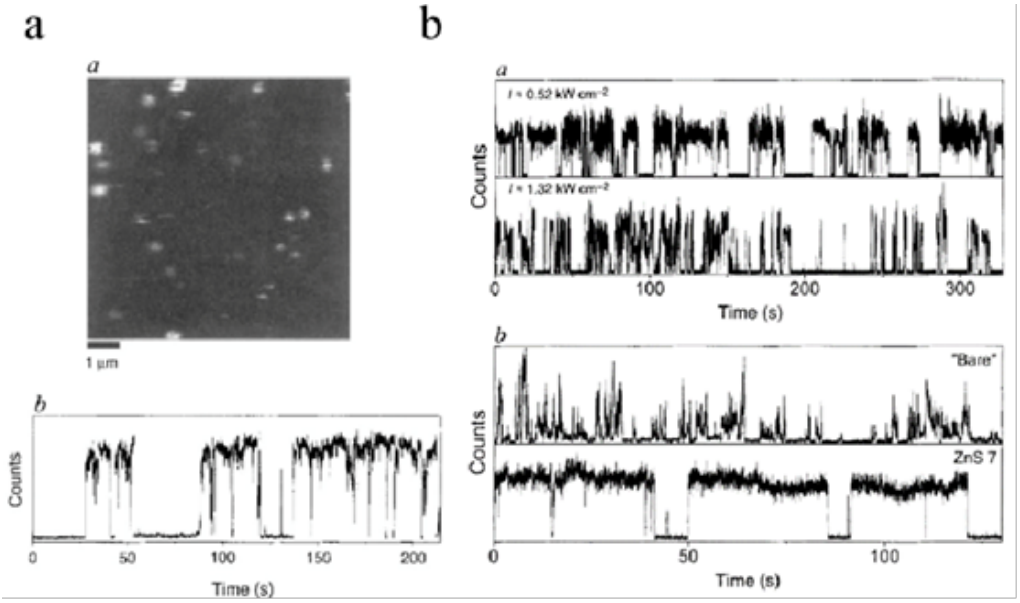

Figure 1.9. (a) a) Photograph of CdSe nanocrystals. b) The trace of fluorescence intensity over time. (b) a) Fluorescence intensity and time traces relationship. b) A fluorescence intensity versus time trace for a 'bare' nanocrystal.[36]

The original report of PL blinking in $MAPbI_3$ PNCs and microcrystals has reported multi-state blinking with significant amplitudes (Figure 1.10).[37] While LHPs, unlike QDs, exhibit enhanced blinking at lower excitation intensities, chalcogenide QDs exhibit enhanced blinking with increasing excitation intensity. A super-resolution microscopy approach was employed to detect this PL behavior. It is discovered that multi-state blinking results from variations in emission localization points, or quenching sites, in the crystal.

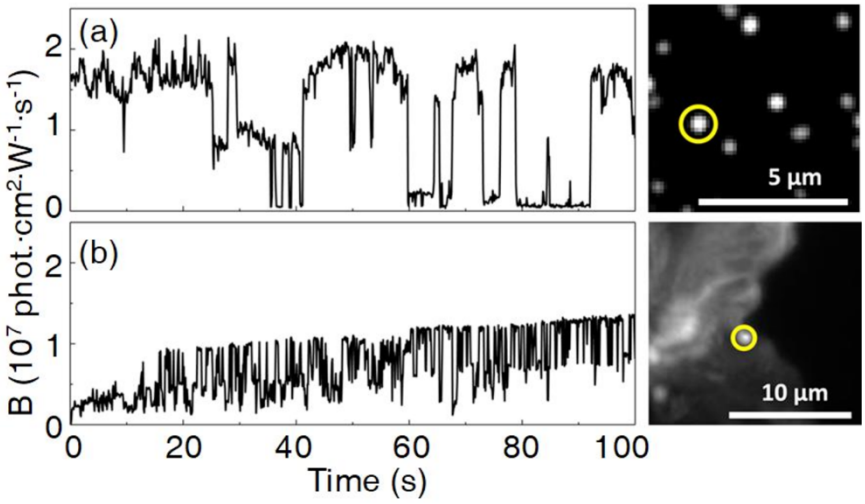

Figure 1.10. Two types of PL blinking of (a) $MAPbI_3$ PNC and (b) a $MAPbI_3$ film.[37]

The 'Quenching site model' or 'Emitting site model' was considered as the mechanism for such PL blinking. The crystal contains several charge carrier traps that are linked to chemical flaws or structural flaws like ion vacancies. In this case, blinking is caused by the activation and deactivation of such faults or trap states (Figure 1.11).[38]

There have been many different kinds of studies to passivate PL blinking. The surface modification by post-treatment for blinking suppression is one illustration. It is discovered that NaSCN surface treatment of $FAPbBr_3$ NCs suppressed PL flickering.[38] The core-shell structure QDs ($CsPbBr_3$-CdS) exhibits good stability and does not show blinking.[39] It can be compared with traditional core-shell QDs that offer fewer defects and are more stable. At a low temperature of 6K, no blinking photoluminescence trajectories

are produced in single halide nanocrystals based on Cs.[40] Recent research has also shown that adjusting perovskite by changing the halide content affects blinking behavior.[41]

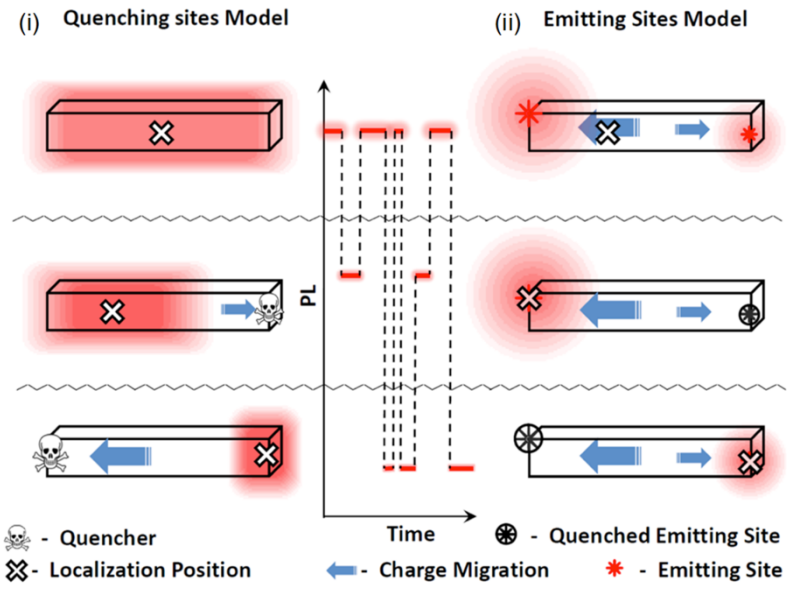

Figure 1.11. Illustration of PL blinking mechanism in PNCs. (a) The quenching-site model and (b) the emitting-site model.[38]

1.5 Applications of halide perovskites

1.5.1 Principles of solar cells

Halide perovskites have become a focal point in solar cell research due to their exceptional photovoltaic characteristics, including high luminescence efficiency, tunable bandgaps, extensive carrier mobility, and large absorption cross-sections.[42-45] Currently, they stand as the most promising semiconductors for solar cells. Increased perovskite solar cell technology advancement can be largely attributed to their unique bandgap feature, high charge carrier diffusion rate, and low Urbach energy. Additionally, their straightforward solution-processed fabrication of high-quality thin films contributes to their popularity. In 2009, Miyasaka et al. conducted a pioneering study on halide perovskite-based solar cells, creating a solar cell with mixed organic-inorganic perovskite

as the absorbance material, and it obtained a high PCE at that time.[46] Despite the initial stability and power conversion efficiency challenges, this work laid the foundation for exploring halide perovskites in solar cells. The field witnessed significant progress with the introduction of mesostructured perovskite solar cells by Snaith et al. in 2012.[47] They utilize TiO_2 and spiro-OMeTAD as the ETL and HTL materials, and these solar cells achieved high-performance productivity. Notably, they further enhanced the performance productivity by replacing TiO_2 to Al_2O_3. Halide perovskites have since emerged as a leader among photovoltaic materials, showcasing the potential to achieve PCE exceeding 25%.

As depicted in Figure 1.12a, a standard perovskite solar cells (PSCs) configuration comprises a perovskite layer functioning as the intrinsic semiconductor for light absorption. This layer is stuck between an ETM and a HTM, all situated on either FTO or ITO glass substrate. A typical n-type ETM is TiO_2, also known as PCBM, and Spiro-OMTAD or PEDOT:PSS. The electrons excited by light diffuse to the ETM's conduction band and then to FTO/ITO after the perovskite layer absorbs light. The HTM's valence band receives holes before the Au/Ag layer. One can create effective solar cells by choosing perovskites, HTMs, and ETMs by using the energy states and bandgaps (Figure 1.12C).

As depicted in Figure 1.12b, the architecture of PSCs can generally be classified into two kinds: direct and inverted. For the direct (n-i-p), the materials ordered from the bottom are transparent anode (ITO or FTO), ETL, perovskite, HTM and the top electrode. In the inverted (p-i-n) type, the materials order from the bottom are transparent cathode (ITO or FTO), HTL, perovskite, ETM, and top electrode. For efficient electron transport, it is crucial to align the conduction band of the ETL with the perovskite to absorb the electron. In the inverted device architecture, the conduction band should match the top electrode, while in the direct device architecture, it should be aligned with the TCO.[48] These considerations highlight the significance of energy alignment in determining the success of the device architecture.

The light-harvesting layer of perovskite solar cells, which absorbs light and starts carriers' generation. The ETL and HTL are commonly necessary for the perovskite solar cells, since the function of ETL is electron collecting and HTL is hole colleting. The perovskite active layer is crucial for producing the recombination of the carries and transportation to the appropriate materials, and for light harvesting.[49] In the perovskite/HTL interface, HTL collects holes, and HTL candidates must fulfill certain requirements to be chosen. As indicated in Figure 1.12c, the HTL should possess certain characteristics for effective device performance, such as a highly mobile rate of hole and electron, matched energy bands, and high stability to enhance the feasibility and economic viability of the device. These characteristics collectively contribute to the optimal functioning of the HTL in perovskite solar cells (PSCs).

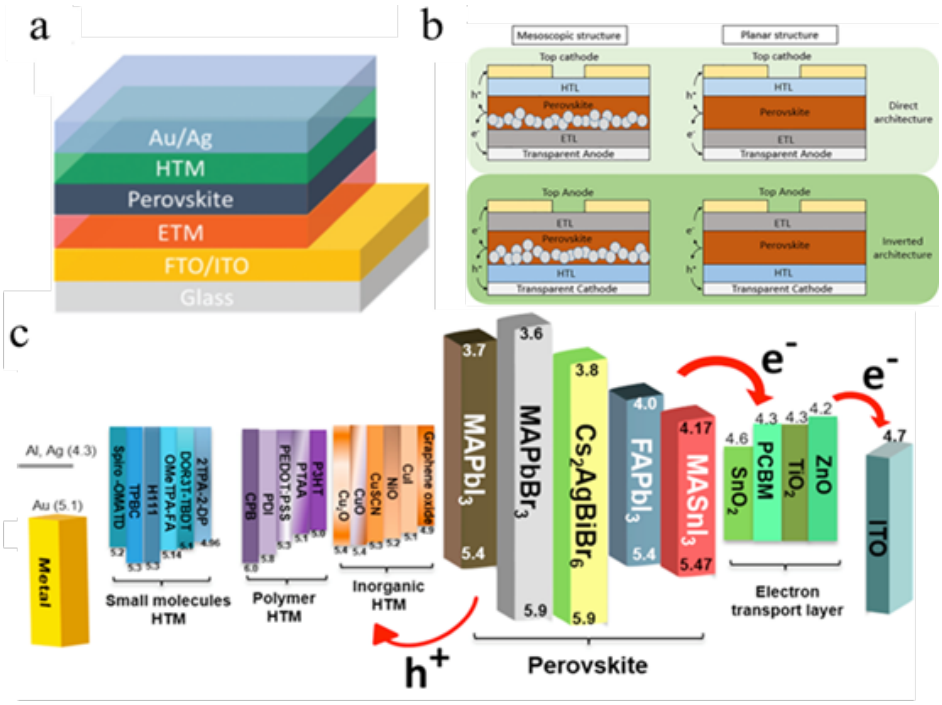

Figure 1.12. (a) perovskite solar cell structure composition.[41] (b) The illustration depicts the components of a perovskite solar cell. The diagram showcases both direct and inverted architectures in the vertical orientation, as well as planar and mesoscopic structures in the horizontal orientation. (c) The energy diagram of various ETL, HTL, perovskite and electrode materials.[48]

1.5.2 Principles of LEDs

A conductive electrode without color, such as FTO or ITO, is placed on top of a glass substrate to fabricate LED devices. A perovskite emissive layer is a middle of HIL and EIL, which also function as blocking materials of charge carriers (Figure 1.13a, b). The deposited metallic film is the rear contact to enclose the LEDs electrically. An external bias is applied to introduce carriers to the working LEDs. The device architecture is arranged to facilitate radiative interaction between electrons and holes in the perovskite emissive layer, aiming to generate EL. Achieving high efficiency requires tuning the perovskite emissive layer, and addressing factors like appropriate outcoupling designs, band alignment and interfacial engineering, which are crucial for pushing the efficiency limits of PeLEDs.

Perovskite light-emitting diodes have device architectures that include multi- and mono-layer configurations. Usually, the multi-layer device is consisted of the transparent electrode (FTO or ITO), HBL, EBL, a perovskite emitter, and an electrode. The HBL, perovskite and EBL produce a heterojunction structure, which helps limit injected charges and enhance light emission. Upon applying voltage, electrons and holes introduced to the perovskite layer through the transporting layers. Multi-layer PeLEDs can have conventional or inverted device structures. In contrast, a single-layer device is fabricated with perovskite sandwiched within electrodes. While recent investigations have explored mixed-cation PeLEDs, the most widely used perovskite emitters are based on the $MAPbX_3$ and $CsPbX_3$ (X = Cl, Br, I, or a combination) family of halide perovskites.[52]

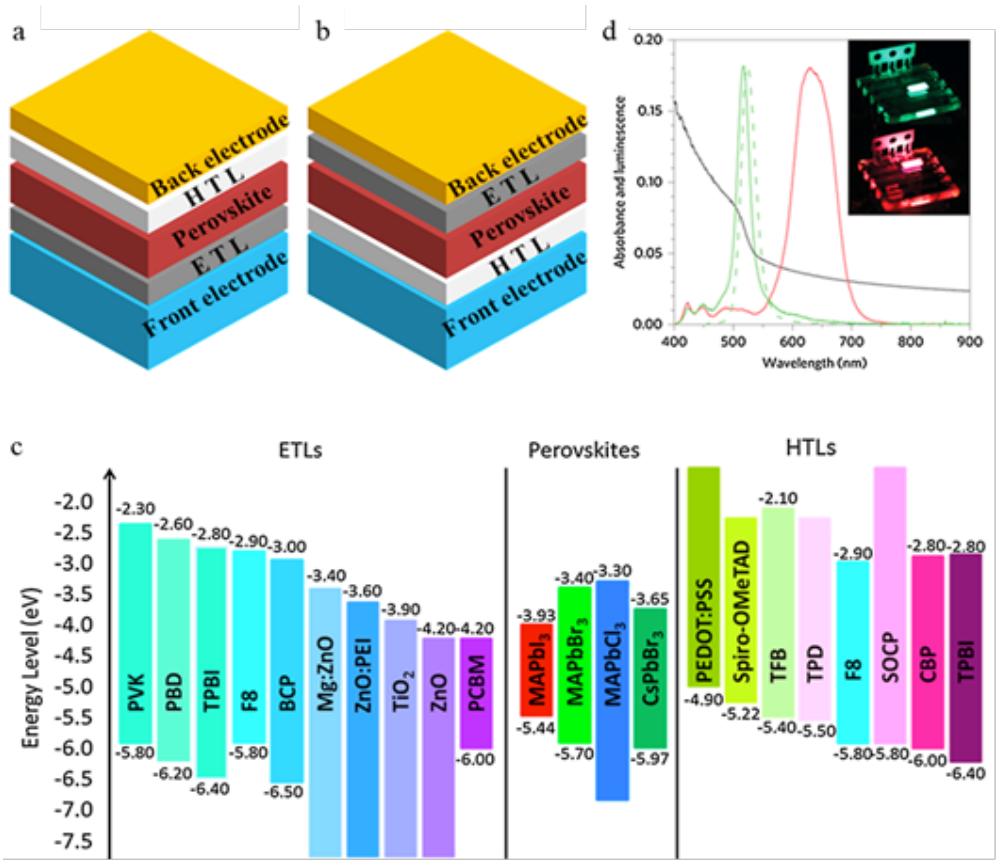

Figure 1.13. (a) (b) Schematic diagrams of the composition of conventional and inverted perovskite light-emitting diodes, respectively. (c) The energy level of different materials utilized as perovskites, ETL and HTL. (d) The optical absorption, normalized electroluminescence and photoluminescence spectra of $MAPbBr_3$ perovskite. The red line is the normalized electroluminescence spectrum of $MAPbBr_2I$ mixed halide perovskite. The inset image is a high EL emission for the device. [50]

The research history of lead halide perovskites is extensive, with the creation of lead halide perovskite dating back to 1892 by Wells.[52] However, it did not gain widespread attention until 1994,[53] when M. Era et al. explored the electrical characteristics of 2D layered halide perovskite. The journey into the application of lead halide perovskites in solar cells began in 2009 when Miyasaka et al. achieved a power conversion efficiency

(PCE) of 3.8% using methyl ammonium lead iodide ($MAPbI_3$) as the sensitizer in dye-sensitized solar cells.[46] This groundbreaking study led to numerous investigations on perovskite solar cells (PSCs), which show a high efficiency 26.0%, encouraging efforts toward commercialization.[54]

The application of perovskites as electroluminescent materials for perovskite light-emitting diodes (LEDs) predates their use in solar cells. However, significant progress in perovskite LEDs began in 2014. Friend et al. developed $MAPbX_3$ thin film to fabricate perovskite LEDs. It displayed a small EQE. Over about 10 years of development,[55-56] the EQE of commercial LEDs has exceeded 20%; among them, green LEDs have the highest 28.9 % EQE. [57]

Perovskite LED's efficiency has been increased throughout time using solvent engineering and defect passivation techniques.[58-61] Perfect films with fewer flaws had been formed by depositing of precursors in the solution or evaporated gas. The instability and degradation under high humidity or oxygen environment, or Joule heating, are some other problems impeding the commercialization of PeLEDs in addition to EQE.[62] Unconventionally, dampness is known to cure surface flaws and enhance their performance at controlled levels.[63] The efficiency of LEDs made from organic semiconductors, various inorganic QD semiconductors, and perovskites are compared in Figure 1.14. As can be observed, perovskite has improved in efficiency more quickly than its rivals in a short amount of time.

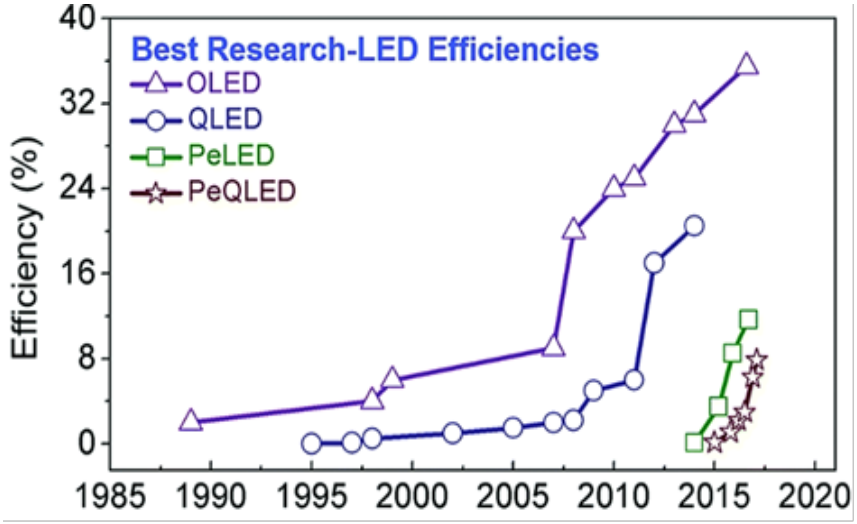

Figure 1.14. The evaluated performance efficiencies of organic and inorganic quantum dot, perovskite and perovskite quantum dot LEDs.[57]

1.6 Motivation and objectives

The halide perovskite subject is a hot domain due to exceptional attributes, such as affordability, straightforward synthesis, strong light absorption, adjustable emission wavelengths, and high photoluminescence quantum yield. Researchers have extensively explored various aspects of these materials, including synthesis methods, luminescence enhancement, and efficiency improvement. However, challenges persist in understanding EL in halide perovskites, particularly regarding the EL blinking mechanism in perovskite single crystals and techniques to enhance such blinking. This stands in contrast to the progress made in understanding photoluminescence, where many key issues have been addressed. My research motivation is to better understand the electroluminescence blinking mechanism and enhancement methods in halide perovskite single crystals. I focus on synthesizing uniform, well-shaped, and high-quality perovskite single crystals and investigating the electroluminescence blinking mechanism and enhancement techniques specific to these crystals. Additionally, I study the time-resolved electroluminescence of commercial LEDs and perovskite $MAPbBr_3$ microcrystals and the effect of halide vacancy filling on the PL and EL decays of $MAPbBr_3$ MCs.

References

1. Keith, H. D.; Padden, F. J. Jr. A Phenomenological Theory of Spherulitic Crystallization. *J. Appl. Phys*. **1963**, *34*, 2409–2421.
2. Pennings, A. J. Bundle-like nucleation and longitudinal growth of fibrillar polymer crystals from flowing solutions. *J. Polym. Sci. Polym. Symp*. **1977**, *59*, 55-86.
3. Liang, C.; Gu, H.; Xia, Y.; Wang, Z.; Liu, X.; Xia, J.; Zou, S.; Hu, Y.; Gao, X.; Hui, W.; Chao, L.; Niu, T.; Fang, M.; Lu, H.; Dong, H.; Yu, H.; Chen, S.; Ran, X.; Song, L.; Li, B.; Zhang, J.; Peng, Y.; Shao, J.; Wang, J.; Chen, Y.; Xing, G.; Huang, W. Two-dimensional Ruddlesden–Popper layered perovskite solar cells based on phase-pure thin films. *Nat. Energy* **2021**, *6*, 38-45.
4. Zhong, Y.; Liao, K.; Du, W.; Zhu, J.; Shang, Q.; Zhou, F.; Wu, X.; Sui, X.; Shi, J.; Yue, S.; Wang, Q.; Zhang, Y.; Zhang, Q.; Hu, X.; Liu, X. Large-scale thin $CsPbBr_3$ single-crystal film grown on sapphire via chemical vapor deposition: Toward laser array application. *ACS Nano* **2020**. *14*, 15605-15615.
5. Hou, Y.; Aydin, E.; De Bastiani, M.; Xiao, C.; Isikgor, F. H.; Xue, D. J.; Chen, B.; Chen, H.; Bahrami, B.; Chowdhury, A. H.; Johnston, A.; Baek, S.-W.; Huang, Z.; Wei, M.; Dong, Y.; Troughton, J.; Jalmood, R.; Mirabelli, A. J.; Allen, T. G.; Kerschaver, E. V.; Saldaminov, M. I.; Baran, D.; Qiao, Q.; Zhu, K.; Wolf, S. D.; Sargent, E. H. Efficient tandem solar cells with solution-processed perovskite on textured crystalline silicon. *Science* **2020**, *367*, 1135-1140.
6. Frenkel, J.; A General Theory of Heterophase Fluctuations and Pretransition Phenomena. *J. Chem. Phys*. **1939**, *7*, 538–547.
7. Chen, L.; Tan, Y. Y.; Chen, Z. X.; Wang, T.; Hu, S.; Nan, Z. A.; Xie, L. Q.; Hui,

Y.; Huang, J. X.; Zhan, C.; Wang, S. H.; Zhou, J. Z.; Yan, J. W.; Mao, B. W.; Tian, Z. Q. Toward long-term stability: single-crystal alloys of cesium-containing mixed cation and mixed halide perovskite. *J. Am. Chem. Soc*. **2019**. *141*, 1665-1671.

8. Saidaminov, M. I.; Adinolfi, V.; Comin, R.; Abdelhady, A. L.; Peng, W.; Dursun, I.; Yuan, M.; Hoogland, S.; Sargent, E. H.; Bakr, O. M. Planar-integrated single-crystalline perovskite photodetectors. *Nat. Commun*. **2015**, *6*, 8724.
9. Maculan, G.; Sheikh, A. D.; Abdelhady, A. L.; Saidaminov, M. I.; Haque, M. A.; Murali, B.; Alarousu, E.; Mohammed, O. F.; Wu, T.; Bakr, O. M. $CH_3NH_3PbCl_3$ single crystals: inverse temperature crystallization and visible-blind UV-photodetector. *J. Phys. Chem. Lett*. **2015**, *6*, 3781–3786.
10. Volmer, M.; Weber, A. Keimbildung in übersattigten gebilden. Z. *Phys. Chem.* **1926**, *119*, 277–301.
11. Tan, Z. K.; Moghaddam, R.S.; Lai, M. L.; Docampo, P.; Higler, R.; Deschler, F.; Price, M.; Sadhanala, A.; Pazos, L. M.; Credgington, D.; Hanusch, F. Bright light-emitting diodes based on organometal halide perovskite. *Nat. Nanotechnol*. **2014**, *9*, 687–692.
12. Lee, M. M.; Teuscher, J.; Miyasaka, T.; Murakami, T. N.; Snaith, H. J. Efficient hybrid solar cells based on meso-superstructure organometal halide perovskites. *Science* **2012**, *338*, 643–647.
13. Kawachi, S.; Atsumi, M.; Saito, N.; Ohashi, N.; Murakami, Y.; Yamaura, J. I. Structural and thermal properties in formamidinium and Cs-mixed lead halides. *J. Phys. Chem. Lett*. **2019**, *10*, 6967–6972.
14. Liu, Y.; Yang, Z.; Cui, D.; Ren, X.; Sun, J.; Liu, X.; Zhang, J.; Wei, Q.; Fan, H.; Yu, F.; Zhang, X. Two-inch-sized perovskite $CH_3NH_3PbX_3$ (X= Cl, Br, I) crystals:

growth and characterization. *Adv. Mater*. **2015**, *27*, 5176–5183.

15. Saidaminov, M. I.; Abdelhady, A. L.; Maculan, G.; Bakr, O. M. Retrograde solubility of formamidinium and methylammonium lead halide perovskites enabling rapid single crystal growth. *Chem. Commun*. **2015**, *51*, 17658–17661.
16. Shi, D.; Adinolfi, V.; Comin, R.; Yuan, M.; Alarousu, E.; Buin, A.; Chen, Y.; Hoogland, S.; Rothenberger, A.; Katsiev, K.; Losovyj, Y.; Zhang, X.; Dowben, P. A.; Mohammed, O. F.; Sargent, E. H.; Bakr, O. M. Low Trap-State Density and Long Carrier Diffusion in Organolead Trihalide Perovskite Single Crystals. *Science* **2015**, *347*, 519–522.
17. Yan, J.; Li, H.; Aldamasy, M. H.; Frasca, C.; Abate, A.; Zhao, K.; Hu, Y. Advances in the Synthesis of Halide Perovskite Single Crystals for Optoelectronic Applications. *Chem. Mater*. **2023**, *35*, 2683–2712.
18. Shamsi, J.; Urban, A. S.; Imran, M.; De Trizio, L.; Manna, L. Metal Halide Perovskite Nanocrystals: Synthesis, Post-Synthesis Modifications, and Their Optical Properties. *Chem. Rev*. **2019**, *119*, 3296–3348.
19. Deka, S.; Genovese, A.; Zhang, Y.; Miszta, K.; Bertoni, G.; Krahne, R.; Giannini, C.; Manna, L. Phosphine-Free Synthesis of p-Type Copper(I) Selenide Nanocrystals in Hot Coordinating Solvents. *J. Am. Chem. Soc*. **2010**, *132*, 8912–8914.
20. Li, X.; Zhang, K.; Li, J.; Chen, J.; Wu, Y.; Liu, K.; Song, J.; Zeng, H. Heterogeneous Nucleation toward Polar-Solvent-Free, Fast, and One-Pot Synthesis of Highly Uniform Perovskite Quantum Dots for Wider Color Gamut Display. *Adv. Mater. Interfaces* **2018**, *5*, 1800010.
21. Manna, L.; Milliron, D. J.; Meisel, A.; Scher, E. C.; Alivisatos, A. P. Controlled

growth of tetrapod-branched inorganic nanocrystals. *Nat. Mater*. **2003**, *2*, 382– 385,

22. Shamsi, J.; Rastogi, P.; Caligiuri, V.; Abdelhady, A. L.; Spirito, D.; Manna, L.; Krahne, R. Bright-Emitting Perovskite Films by Large-Scale Synthesis and Photoinduced Solid-State Transformation of $CsPbBr_3$ Nanoplatelets. *ACS Nano* **2017**, *11*, 10206–10213,

23. Wei, S.; Yang, Y.; Kang, X.; Wang, L.; Huang, L.; Pan, D. Room-temperature and gram-scale synthesis of $CsPbX_3$ (X = Cl, Br, I) perovskite nanocrystals with 50–85% photoluminescence quantum yields. *Chem. Commun*. **2016**, *52*, 7265–7268.

24. Wang, K. H.; Wu, L.; Li, L.; Yao, H. B.; Qian, H. S.; Yu, S. H. Large-Scale Synthesis of Highly Luminescent Perovskite-Related $CsPb_2Br_5$ Nanoplatelets and Their Fast Anion Exchange. *Angew. Chem. Int. Ed*. **2016**, *55*, 8328– 8332.

25. Papavassiliou, G. C.; Pagona, G.; Karousis, N.; Mousdis, G. A.; Koutselas, I.; Vassilakopoulou, A. Nanocrystalline/microcrystalline materials based on lead-halide units. *J. Mater. Chem*. **2012**, *22*, 8271– 8280.

26. Stoumpos, C. C.; Kanatzidis, M. G. The renaissance of halide perovskites and their evolution as emerging semiconductors. *Acc. Chem. Res*. **2015**, *48*, 2791-2802.

27. Tong, Y. L.; Zhang, Y. W.; Ma, K.; Cheng, R.; Wang, F.; Chen, S. One-Step Synthesis of FA-Directing $FAPbBr_3$ Perovskite Nanocrystals toward High-Performance Display. *ACS Appl. Mater. Interfaces* **2018**, *10*, 31603–31609.

28. Levchuk, I.; Osvet, A.; Tang, X.; Brandl, M.; Perea, J. D.; Hoegl, F.; Matt, G. J.; Hock, R.; Batentschuk, M.; Brabec, C. J. Brightly Luminescent and Color-Tunable Formamidinium Lead Halide Perovskite $FAPbX_3$ (X = Cl, Br, I) Colloidal Nanocrystals. *Nano Lett*. **2017**, *17*, 2765–2770.

29. Im, J.; Stoumpos, C. C.; Jin, H.; Freeman, A. J.; Kanatzidis, M. G. Antagonism

between Spin–Orbit Coupling and Steric Effects Causes Anomalous Band Gap Evolution in the Perovskite Photovoltaic Materials $CH_3NH_3Sn_{1-x}Pb_xI_3$. *J. Phys. Chem. Lett*. **2015**, *6*, 3503–3509.

30. Lee, S. W.; Kim, S.; Bae, S.; Cho, K.; Chung, T.; Mundt, L. E.; Lee, S.; Park, S.; Park, H.; Schubert, M. C.; Glunz, S. W.; Ko, Y.; Jun, Y.; Kang, Y.; Lee, H. S.; Kim, D. UV Degradation and Recovery of Perovskite Solar Cells. *Sci. Rep*. **2016**, *6*, 38150.

31. Deng, Y.; Peng, E.; Shao, Y.; Xiao, Z.; Dong, Q.; Huang, J. Scalable Fabrication of Efficient Organolead Trihalide Perovskite Solar Cells with Doctor-Bladed Active Layers. *Energy Environ. Sci*. **2015**, *8*, 1544–1550.

32. Huang, L. Y.; Lambrecht, W. R. Electronic band structure, phonons, and exciton binding energies of halide perovskites $CsSnCl_3$, $CsSnBr_3$, and $CsSnI_3$. *Phys. Rev. B* **2013**, *88*, 165203.

33. Zhang, X.; Shen, J.; Van De Walle, C. G. First-Principles Simulation of Carrier Recombination Mechanisms in Halide Perovskites. *Adv. Energy Mater*. **2020**, *10*, 1902830.

34. Nguyen, V. C.; Katsuki, H.; Sasaki, F.; Yanagi, H. Single-Crystal Perovskite $CH_3NH_3PbBr_3$ Prepared by Cast Capping Method for Light-Emitting Diodes. *Jpn. J. Appl. Phys*. **2018**, *57*, 04FL10.

35. Sharma, D. K.; Hirata, S.; Vacha, M. Single-particle electroluminescence of $CsPbBr_3$ perovskite nanocrystals reveals particle-selective recombination and blinking as key efficiency factors. *Nat. Commun*. **2019**, *10*, 4499.

36. Nirmal, M.; Dabbousi, B. O.; Bawendi, M. G.; Macklin, J. J.; Trautman, J. K.; H.; Harris, T. D.; Brus, L. E. Fluorescence intermittency in single cadmium selenide

nanocrystals. *Nature* **1996**, *383*, 802-804.

37. Tian, Y.; Merdasa, A.; Peter, M.; Abdellah, M.; Zheng, K.; Ponseca, C. S.; Pullerits, T.; Yartsev, A.; Sundström, V.; Scheblykin, I. G. Giant Photoluminescence Blinking of Perovskite Nanocrystals Reveals Single-Trap Control of Luminescence. *Nano Lett*. **2015**, *15*, 1603–1608.

38. Jiang, L.; Liu, R.; Su, R.; Yu, Y.; Xu, H.; Wei, Y.; Zhou, Z. K.; Wang, X. Continuous Wave Pumped Single-Mode Nanolasers in Inorganic Perovskites with Robust Stability and High Quantum Yield. *Nanoscale* **2018**, **10**, 13565-13571.

39. Yarita, N.; Tahara, H.; Saruyama, M.; Kawawaki, T.; Sato, R.; Teranishi, T.; Kanemitsu, Y. Impact of Postsynthetic Surface Modification on Photoluminescence Intermittency in Formamidinium Lead Bromide Perovskite Nanocrystals. *J.* P*hys. Chem. Lett*. **2017**, *8*, 6041–6047.

40. Tang, X.; Yang, J.; Li, S.; Liu, Z.; Hu, Z.; Hao, J.; Du, J.; Leng, Y.; Qin, H.; Lin, X.; Lin, Y.; Tian, Y.; Zhou, M.; Xiong, Q. Single Halide Perovskite/Semiconductor Core/Shell Quantum Dots with Ultrastability and Nonblinking Properties. *Adv. Sci*. **2019**, *6*, 1900412.

41. Rainoì, G.; Nedelcu, G.; Protesescu, L.; Bodnarchuk, M. I.; Kovalenko, M. V.; Mahrt, R. F.; Stöferle, T. Single Cesium Lead Halide Perovskite Nanocrystals at Low Temperature: Fast Single-Photon Emission, Reduced Blinking, and Exciton Fine Structure. *ACS Nano* **2016**, *10*, 2485–2490.

42. Zhang, A.; Dong, C.; Ren, J. Tuning Blinking Behavior of Highly Luminescent Cesium Lead Halide Nanocrystals through Varying Halide Composition. *J. Phys. Chem. C* **2017**, *121*, 13314–13323.

43. Chouhan, L.; Ghimire, S.; Subrahmanyam, C.; Miyasaka, T.; Biju, V. Synthesis,

Optoelectronic Properties and Applications of Halide Perovskites. *Chem. Soc. Rev*. **2020**, *49*, 2869–2885.

44. Zhu, X.; Ge, L.; Wang, Y.; Li, M.; Zhang, R.; Xu, M.; Zhao, Z.; Lv, W.; Chen, R. Recent Advances in Enhancing and Enriching the Optical Properties of Cl-Based $CsPbX_3$ Nanocrystals. *Adv. Opt. Mater*. **2021**, *9*, 2100058.

45. Lignos, I.; Stavrakis, S.; Nedelcu, G.; Protesescu, L.; Demello, A. J.; Kovalenko, M. V. Synthesis of Cesium Lead Halide Perovskite Nanocrystals in a Droplet-Based Microfluidic Platform: Fast Parametric Space Mapping. *Nano Lett*. **2016**, *16*, 1869–1877.

46. Kojima, A.; Teshima, K.; Shirai, Y.; Miyasaka, T. Organometal Halide Perovskites as Visible-Light Sensitizers for Photovoltaic Cells. *J. Am. Chem. Soc*. **2009**, *131*, 6050– 6051.

47. Micheal, L.; Joel, T.; Tsutomu, M.; Takurou, N. M.; Henry, J. S. Efficient Hybrid Solar Cells based on Meso-Superstructured Organometal Halide Perovskites. *Science* **2012**, *338*, 643–647.

48. Safie, N. E.; Azam, M. A.; Aziz, M. F. A.; Ismail, M. Recent Progress of Graphene-based Materials for Efficient Charge Transfer and Device Performance Stability in Perovskite Solar Cells. *Int. J. Energy Res*. **2021**, *45*, 1347–1374.

49. Peng, J.; Chen, Y.; Zheng, K.; Pullerits, T.; Liang, Z. Insights into charge carrier dynamics in organo-metal halide perovskites: from neat films to solar cells. *Chem. Soc. Rev*. **2017**, *46*, 5714-5729.

50. Tan, Z. K.; Moghaddam, R. S.; Lai, M. L.; Docampo, P.; Higler, R.; Deschler, F.; Price. M.; Sadhanala. A.; Pazos, L. M.; Credgington, D.; Hanusch, F.; Bein, T.; Snaith, H. J.; Friend, R. H. Bright light-emitting diodes based on organometal

halide perovskite. *Nat. Nanotechnol*. **2014**. *9*, 687-692.

51. Byun, J.; Cho, H.; Wolf, C.; Jang, M.; Sadhanala, A.; Friend, R. H.; Yang, H.; Lee, T. W. Efficient visible quasi-2D perovskite light-emitting diodes. *Adv. Mater*. **2016**, *28*, 7515-7520.

52. Wells, H. L. Über die cäsium-und kalium-bleihalogenide. *Z. Anorg. Chem.* **1893**, *3*, 195-210.

53. Era, M.; Morimoto, S.; Tsutsui, T.; Saito, S. Organic-inorganic heterostructure electroluminescent device using a layered perovskite semiconductor $(C_6H_5C_2H_4NH_3)_2PbI_4$. *Appl. Phys. Lett*. **1994**, *65*, 676-678.

54. Dale, P. J.; Scarpulla, M. A. Efficiency versus Effort: A Better Way to Compare Best Photovoltaic Research Cell Efficiencies? *Sol. Energy Mater. Sol. Cell*. **2023**, *251*, 112097.

55. Chiba, T.; Hayashi, Y.; Ebe, H.; Hoshi, K.; Sato, J.; Sato, S.; Pu, Y. J.; Ohisa, S.; Kido, J. Anion-exchange red perovskite quantum dots with ammonium iodine salts for highly efficient light-emitting devices. *Nat. Photon*. **2018**, *12*, 681-687.

56. Zhu, L.; Cao, H.; Xue, C.; Zhang, H.; Qin, M.; Wang, J.; Wen, K.; Fu, Z.; Jiang, T.; Xu, L.; Zhang, Y.; Cao, Y.; Tu, C.; Zhang, J.; Liu, D.; Zhang, G.; Kong, D.; Fan, N.; Li, G.; Yi, C.; Peng, Q.; Chang, J.; Liu, X.; Wang, N.; Huang, W.; Wang, J. Unveiling the additive-assisted oriented growth of perovskite crystallite for high performance light-emitting diodes. *Nat. Commun*. **2021**, *12*, 5081.

57. Kim, J. S.; Heo, J. M.; Park, G. S.; Woo, S. J.; Cho, C.; Yun, H. J.; Kim, D. H.; Park, J.; Lee, S. C.; Park, S. H.; Yoon, E.; Greenham, N. C.; Lee, T. W. Ultra-bright, efficient and stable perovskite light-emitting diodes. *Nature* **2022**, *611*, 688-694.

58. Deng, W.; Fang, H.; Jin, X.; Zhang, X.; Zhang, X.; Jie, J. Organic-inorganic hybrid

perovskite quantum dots for light-emitting diodes. *J. Mater. Chem. C* **2018**, *6*, 4831-4841.

59. Cho, H.; Kim, Y. H.; Wolf, C.; Lee, H. D.; Lee, T. W. Improving the stability of metal halide perovskite materials and light-emitting diodes. *Adv. Mater*. **2018**, *30*, 1704587.

60. Wei, Z.; Xing, J. The rise of perovskite light-emitting diodes. *J. Phys. Chem. Lett*. **2019**, *10*, 3035-3042.

61. Jeon, N. J.; Noh, J. H.; Kim, Y. C.; Yang, W. S.; Ryu, S.; Seok, S. I. Solvent engineering for high-performance inorganic–organic hybrid perovskite solar cells. *Nat. Mater*. **2014**, *13*, 897-903.

62. Wozny, S.; Yang, M.; Nardes, A. M.; Mercado, C. C.; Ferrere, S.; Reese, M. O.; Zhou, W.; Zhu, K. Controlled humidity study on the formation of higher efficiency formamidinium lead triiodide-based solar cells. *Chem. Mater*. **2015**, *27*, 4814-4820.

63. You, J.; Yang, Y. M.; Hong, Z.; Song, T. B.; Meng, L.; Liu, Y.; Jiang, C.; Zhou, H.; Chang. W. H.; Li, G.; Yang, Y. Moisture assisted perovskite film growth for high performance solar cells. *Appl. Phys. Lett*. **2014**, *105*, 183902.

Chapter 2

Experiments

Abstract

This chapter introduces the experimental methods I used for synthesizing the perovskite materials, including different conventional and modified methods. The characteristics of perovskites is measured by spectroscopic methods and instrumentations. The different crystallization procedures to prepare lead halide perovskite microcrystals. A modified ITC method is utilized to prepare the uniform size, shape, and high-quality single crystal. The crystal shape and photoluminescence images are measured using a microscope and laser. The PL lifetime is measured using a time-correlated single photon counting-based lifetime system. The EL blinking behavior of single crystal is recorded by the single particle system with a 405 nm laser excitation. The LED device is fabricated between two ITO glass sheets with $MAPbBr_3$ MCs in the middle. Time-resolved fluorescence spectroscopy with a picosecond laser is used to study the carrier dynamics of photoexcitation and electronic excitation. For time-resolved electroluminescence measurements, a ps laser is replaced with a function generator as the power source.

2.1 Materials

The chemicals and materials that I used for these studies are as follows. Lead bromide ($PbBr_2$, ≥98%, Aldrich), formamidinium bromide (FABr, >98%, Tokyo Chemical Industry (TCI)), methylammonium bromide (MABr, >98%, (TCI)), lead iodide (PbI_2, >99%, Aldrich), *N*-Cyclohexyl-2-pyrrolidone (CHP) (98%, Aldrich), *N,N*-dimethylformamide (DMF, FUJIFILM Wako Pure chemical Corporation (WAKO)), γ-butyrolactone (GBL, ≥99%, FUJIFILM Wako Pure chemical Corporation (WAKO)), dichloromethane (DCM, WAKO), 1-hexanedence (HDC, TCL, >90%), isopropanol (C_3H_8O, 99.7%, WAKO), toluene (99.5%, WAKO), PAR (4-(2-pyridyl azo) resorcinol (Sigma-Aldrich), ITO coated microscope glass (surface resistivity 14-16 Ω/sq. Ossila). ITO-coated microscope glass substrates are used after water and acetone cleaning and finally dried. All the other chemicals were used as such or after drying it under an inert atmosphere.

2.2 Methods

2.2.1 Synthesis of $MAPbBr_3$ single crystals

Room temperature crystallization (RTC) method

The $MAPbBr_3$ microcrystals are synthesized by mixing equal volumes of 1 M MABr and 1 M $PbBr_2$ precursors in DMF to produce a $MAPbBr_3$ precursor solution. Then, an equal volume of 1 M $MAPbBr_3$ solution with GBL is well mixed to form the $MAPbBr_3$-GBL precursor solution.[1-2] Subsequently, a small amount (20 μL) of this precursor is dropped onto an ITO glass. Spontaneous crystallization occurs in a few minutes, and $MAPbBr_3$ microcrystals of plate- cubic- and rod-shape are formed. The resultant crystals continuously grow under the supersaturated condition (Figure 2.1a).

Antisolvent vapor-assisted crystallization (AVC) method

The procedure created by Schmidt et al. is used to prepare the microcrystals.[3] 5 mL DMF

was used to dissolve $PbBr_2$ (690 mg) and MABr (210 mg) separately to create the precursor solution, 1 mL from each solution was well mixed to obtain the precursor solution. In a beaker, an ITO glass was dropped with 100 µL of this precursor solution and put on a silicon stage in the beaker. An antisolvent (DCM) for perovskite was prefilled into the beaker to a level below the stage. The nucleation occurs within a short time, and the crystal grows until the following day. This technique produced perovskite microcrystals with sizes ranging from 40 to 150 m. We can regulate the crystal size by adjusting the precursor solution concentration or growth time.[4-5] Figure 2.1b depicts the synthesis scheme.

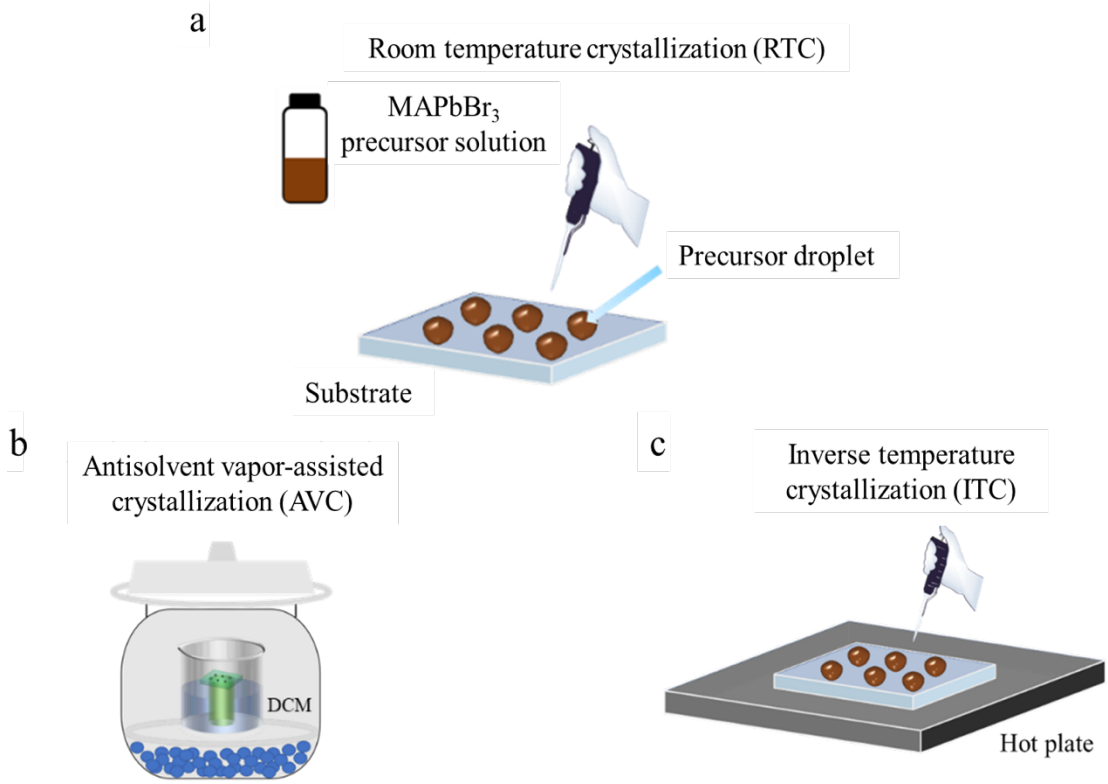

Figure 2.1. Single crystal crystallization method. (a) RTC (b) AVC and (c) ITC methods.

Inverse temperature crystallization (ITC) method

To create a 0.01 M solution, $PbBr_2$ and MABr were dissolved in DMF. An ITO glass on a hot plate that has been preheated to 200 °C. 2 µL of this solution was dropped on it.

$MAPbBr_3$ microcrystals nucleated and grew to 10 μm size crystals in seconds. This method allows for the production of large irregular microcrystals. The scheme of this process is depicted in Figure 2.1c.[6]

Modified inverse temperature crystallization (ITC) method

To produce a 0.01 M solution, $PbBr_2$ and MABr are dissolved in DMF. *N*-cyclohexyl-2-pyrrolidone (CHP) was added to the mixture at different concentrations (2, 5, 10, 20% volume ratio) to regulate crystal development and size. On an ITO glass on a hot plate preheated to different temperatures (80, 100, 120, 140, 160, 180 and 200 °C), 2 μL of as-prepared precursor solutions were dropped. $MAPbBr_3$ microcrystals nucleated and grew in seconds or minutes. This method allows for producing microcrystals of various sizes by controlling the CHP ratio and reaction temperature. The polar ring, low vapor pressure, and high boiling point of the additive are all helpful in regulating the kinetics of crystal formation and size. The process for creating perovskite microcrystals using the ITC approach is depicted in Figure 2.2.[7]

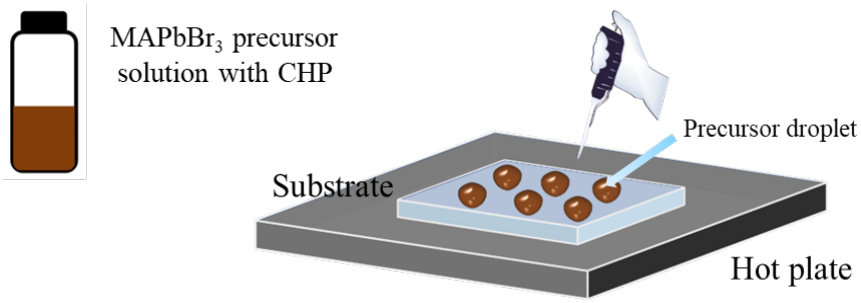

Figure 2.2. The scheme of modified-ITC method.

Doctor-blading method

The doctor-blading method is a cost-effective and fast crystallization procedure for synthesizing perovskite crystals. By varying the temperature, the film with different grain sizes can be obtained. As shown in Figure 2.3, a substrate (ITO) is heated at 100-160 °C, and then, a precursor solution is dropped on the substrate and bladed by a glass sheet quickly. After that, a thin soliton film is formed on the substrate, and as a result of the

heating-induced solvent evaporation, the perovskite polycrystalline film is obtained a few minutes later.[8]

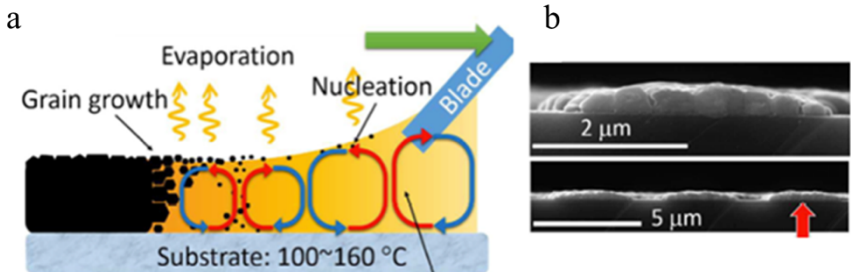

Figure 2.3. The scheme of doctor-blading method.

The precursor is prepared by mixing the equal volume of 1 M MABr and $PbBr_2$ solutions, respectively. Then, an equal volume of as-prepared precursor was mixed with GBL and sonicated for several seconds to dissolve completely. It is labeled as $MAPbBr_3$-GBL precursor solution. Drop 20 µL $MAPbBr_3$-GBL precursor on the ITO glass, blade by another fresh ITO glass several times to form a s smooth solution film with no bubble inside. After waiting for 30 minutes, the crystallization was completed, and $MAPbBr_3$ single crystals were obtained (Figure 2.4).

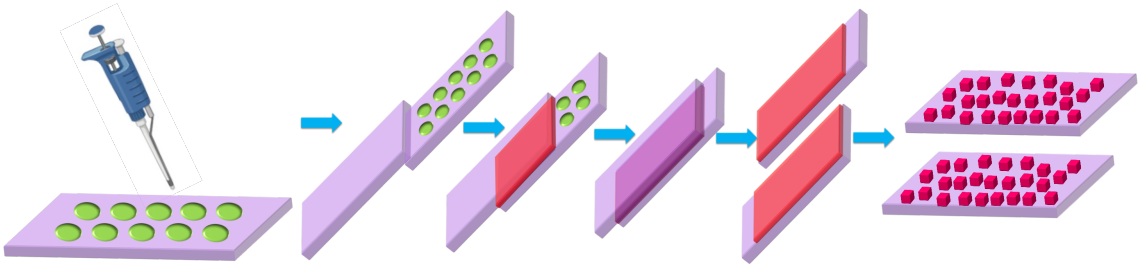

Figure 2.4. Doctor-blading method to synthesize perovskite microcrystal.

2.2.2 LED device fabrication

The LED device is prepared by capping one fresh ITO on another ITO with the as-synthesized $MAPbBr_3$ single crystal, stabilizing these two ITOs with small clips, and then electrically connected with the power supply to carry out the following experiments at various voltages (3 V to 10 V) (Figure 2.5). The conductive copper tape is used to connect

the metal clips with two ITO glasses to enhance the stability and conductivity.

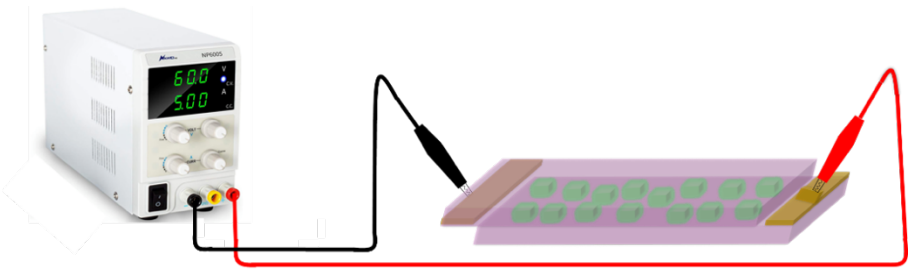

Figure 2.5. $MAPbBr_3$ MCs LED device set up with power supply.

2.2.3 Instruments

Beer-Lambert law and UV-vis spectrophotometry

The Beer-Lambert law, an empirical law in physics, establishes a connection between the characteristics of the material through which light passes and its extinction or attenuation. Initially applied to astronomical extinction, the Beer-Lambert law now has broader applications. In physical optics, the extinction law is also employed to understand attenuation for photons, neutrons, or rarefied gases. Chemical analysis measurements typically determine the concentration of a chemical species that absorbs light following the Beer-Lambert law. Lambert's law states the amount of light absorbed by a sample is directly proportional to the thickness of the sample. Beer's law states the absorbance of a sample is proportional to the concentration of the sample.

A spectrophotometer helps measure the intensity of light passing through a sample against a reference for each wavelength, following the Beer-Lambert Law: A= εlc, the constant ε is called molar absorptivity or molar extinction coefficient and is a measure of the probability of the electronic transition.

The overall light intensity change due to absorption by a sample is given by (eq.1) for a small intensity change dI for light passing a small sample thickness dx.

$$\int_{I0}^{I} \frac{dI}{I} = -\beta c \int_{0}^{\ell} dx \qquad ------(1)$$

where C is the sample concentration and β is a constant. For the light intensity change from I0 to I for a path length change from 0 to l, eq. 1 modifies into eq. 2.

$$-\int_{I0}^{I}\frac{dI}{I}=\beta c\int_{0}^{\ell}dx=\beta c\int_{0}^{\ell}x^{0}dx------(2)$$

From the integral power law ($\int x^{n}dx=\frac{x^{n+1}}{n+1}+C$) and the fundamental theorem of calculus [$\int_{0}^{\ell}f(x)dx=f(\ell)-f(0)$]. Therefore,

$$\beta c\int_{0}^{\ell}x^{n}dx=\beta cx]\ \ =\beta c\ell,\qquad and-\int_{I0}^{I}\frac{dI}{I}=ln\frac{I_0}{I}$$

Or, $ln\frac{I_0}{I}=\beta c\ell$, or $A=\varepsilon c\ell$; A = $ln\frac{I_0}{I}$ and $\varepsilon=\beta/2.30258$

I investigated the optical excitation characteristics of the PNCs or PQDs using absorption spectroscopy. Thermo Fischer Scientific's Evolution 220 UV-vis spectrophotometer was used to record the absorption spectra of a suspension of PNCs (or PQDs) contained in toluene. Also, it was used to estimate the concentration changes of MC precursor solutions while evaluating the crystal nucleation-growth kinetics. Figure 2.6 depicts the detection method for samples' optical absorption. Typically, an excitation source (wavelength 190–900 nm) is employed to measure absorbance. A monochromator was used to select the excitation coming from the source.

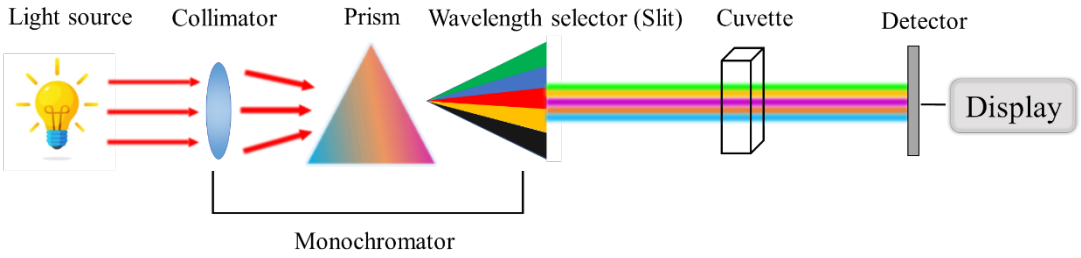

Figure 2.6. Single-beam UV-vis absorption spectrophotometer scheme.

Steady-state fluorescence spectroscopy

Steady-state PL spectroscopy was used to study the photoluminescence from a perovskite solution, corresponding to the radiative relaxation of excited-state charge carriers. For this, I utilized a Hitachi FL-4500 fluorescence spectrophotometer. Below is a diagram (Figure 2.7) of the spectrophotometer's optical configuration: A xenon lamp serving as the excitation source offers a variety of wavelengths. A diffraction grating or a monochromator can be used to choose the ideal wavelength for excitation. The detector only captures the fluorescence light. This is achieved by collecting the emitted light at the right angle, using a photomultiplier tube as the detector. The detector collects the emitted light, and the signal was plotted as intensity vs wavelength.

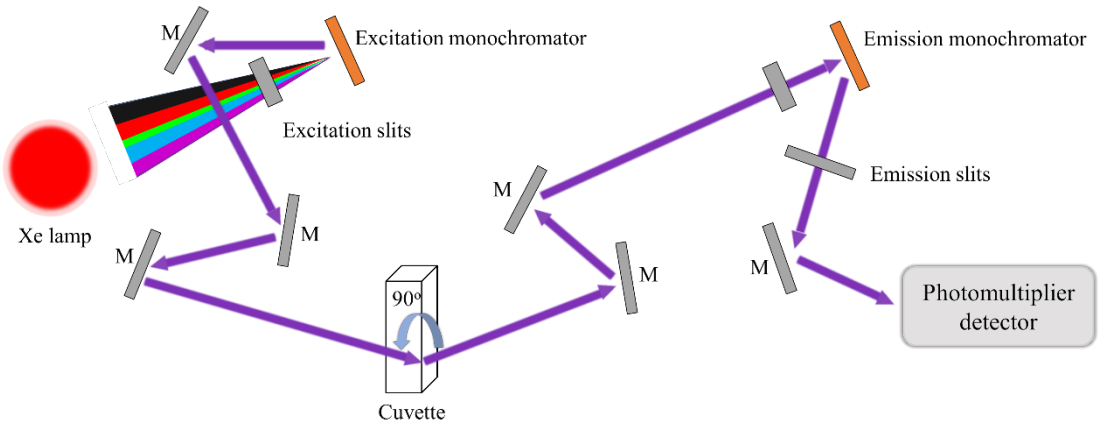

Figure 2.7. A scheme of a steady-state fluorescence spectrometer.

Time-resolved fluorescence spectroscopy

Time-resolved fluorescence spectroscopy is a powerful technique to study the dynamics of fluorescence emission. Unlike steady-state fluorescence measurements, which provide information about the overall fluorescence intensity and spectral characteristics, time-resolved fluorescence spectroscopy allows researchers to investigate the temporal aspects of fluorescence phenomena.

In this method, a pulsed light source, often a laser, is used to excite the sample, leading to the generation of fluorescence. The fluorescence emission is then monitored

over time using a detector. By precisely controlling the timing of the excitation pulses and recording the fluorescence signal at various time delays, researchers can obtain detailed information about the lifetimes of fluorescent species, their decay kinetics, and interactions within a system. Time-resolved fluorescence spectroscopy is particularly precious in many research areas, such as chemistry, physics, biology, and materials science. It enables the characterization of molecular processes, such as energy transfer, molecular dynamics, and reactions, on timescales ranging from picoseconds to milliseconds. This technique has applications in studying the behavior of fluorophores, probing structural changes, and understanding the underlying mechanisms of complex systems.[9-12]

Here are some key concepts and components of time-resolved fluorescence spectroscopy: Pulsed light source: time-resolved fluorescence spectroscopy typically involves using a picosecond laser. Fluorescence Emission: the excited molecules/materials relax to their ground state by radiative or nonradiative pathways. This emission is typically at a longer wavelength than the excitation light due to internal conversion in the excited state and as an effect of Kasha's rule. Detector: A detector used to measure the fluorescence emission may be a photomultiplier tube (PMT), a photodiode, or other microchannel plates/modules capable of detecting weak light signals.[10]

The key feature of time-resolved fluorescence spectroscopy is the ability to measure the emitted fluorescence at various time delays after the excitation pulse. This is achieved using a time-delay unit between excitation and emission. The resulting data or a fluorescence decay curve represents the intensity of the emitted fluorescence as a function of time. The fluorescence lifetime is the average value of a molecule that remains excited before relaxing to the ground state. Different fluorescent species within the sample may have distinct fluorescence lifetimes. Time-resolved fluorescence spectroscopy setups can vary, but they often include components such as monochromators or filters to isolate specific wavelengths, detectors for measuring fluorescence, and electronics for controlling the timing and data acquisition.[11-12]

The main characteristics of fluorescence or photoluminescence are the quantum efficiency Φ_F.

$$\Phi_F = \frac{The\ number\ of\ emitted\ photons}{The\ number\ of\ absorbed\ photons}$$
$$= \frac{k_r}{k_r + k_{nr}}$$

Where k_r is the rate of radiative relaxation and k_{nr} is the rate of nonradiative relaxation.

Also, the fluorescence or photoluminescence lifetime τ is given by

$$\tau = \frac{1}{k_r + k_{nr}}$$

When $k_r >> k_{nr}$,

$$\tau = \frac{1}{k_r}\ or\ \Phi_F \approx 1$$

The excited species relaxes to the ground state, following a first-order process obtained as follows.

The rate at the excited state population (N) decreases is proportional to the population.

$$\frac{dN}{dt} \propto -N$$

For the population decrease from N_0 to N during the time t,

$$\int_{N0}^{N} \frac{dN}{N} = -(k_r + k_{nr}) \int_0^t dt$$

$$\frac{N}{N_0} = e^{-(k_r + k_{nr})t}$$

$$N = N_0\, e^{-(k_r + k_{nr})t}$$

$$\text{Or } N = N_0\, 0\, e^{-t/\tau}$$

I fitted the PL decay plots using the third exponential equation as below:

$$\gamma(t) = \alpha_0 + \alpha_1 e^{(-t/\tau_1)} + \alpha_2 e^{(-t/\tau_2)} + \alpha_3 e^{(-t/\tau_3)}$$

Here, α_0 is a constant, and α_1, α_2, and α_3 are the amplitudes, while τ_1, τ_2, and τ_3 represent different lifetime components. Typically, the initial component is associated with radiative recombination, while the other two components originate from non-radiative recombination.

Time-correlated single-photon counting (TCSPC) system

Time-correlated single-photon counting (TCSPC) stands as a foundational technique in fluorescence spectroscopy, offering unparalleled precision in measuring fluorescence lifetimes. As a fundamental tool in various scientific disciplines, TCSPC enables researchers to delve into the dynamics of excitonic processes in molecules and materials.[13-14]

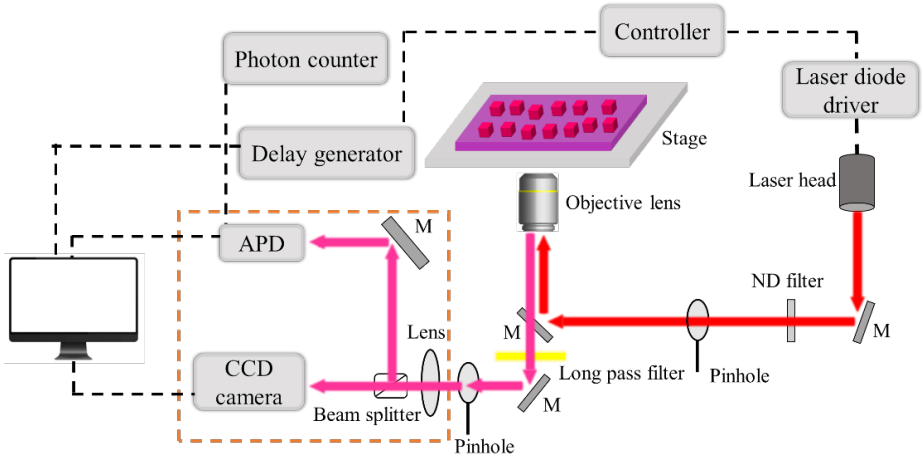

Figure 2.8. The optical setup of TCSPC.

I utilize a TCSPC system with a 465 nm picosecond laser system (Advanced Laser Diode, 1 MHz, 45 ps) to analyze the photoluminescence lifetimes of microcrystals. Figure 2.8 illustrates the optical setup. The sample was placed on the stage of an Olympus IX71 confocal microscope. The excitation light source was a 465 nm picosecond laser with a 1 MHz repetition rate. Just before the sample on the laser direction, a dichroic mirror with 90% transmission in the 460 nm–700 nm range was inserted to filter the laser off. The emitted light was collected using an objective lens (40x, 0.75 NA, UPLanFLN). An avalanche photodiode (APD, PerkinElmer AQR 15) with a single-photon counting module (SPC-830, Becker & Hickl GmBH) was used for photon counting.

Single-particle micro spectroscopy

I examined the PL and EL from single crystals using single-particle microspectroscopy in a wide-field illumination optical arrangement. Contrary to confocal fluorescence spectroscopy, wide-field fluorescence spectroscopy produces a wider focal spot, allowing for the acquisition of collective fluorescence from an entire microcrystal in the field of view. For single particle imaging, a cw laser (450 nm) was used to photoexcite the sample placed on an XY stage attached to an inverted optical microscope (IX71, Olympus). The microscope was equipped with an electron-multiplying charge-coupled device (EMCCD, iXON, Andor Technology) and an objective lens (40x, 0.60 NA, Olympus) (Figure 2.9).

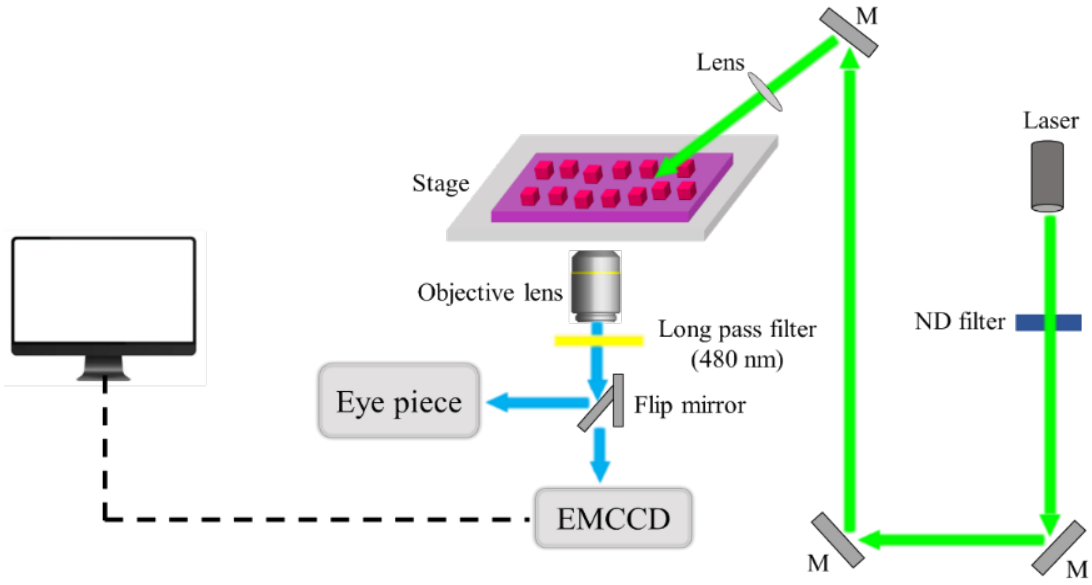

Figure 2.9. The optical setup of a single particle fluorescence microscope.

References

1. Shahjahan, M.; Yuyama, K. I.; Okamoto, T.; Biju, V. Heterojunction Perovskite Microrods Prepared by Remote-Controlled Vacancy Filling and Halide Exchange. *Adv. Mater. Technol*. **2021**, *6*, 2000934.
2. Okamoto, T.; Shahjahan, Md.; Biju, V. Shap-Dependent Kinetics of Halide Vacancy Filling in Organolead Halide Perovskites. *Adv. Opt. Mater*. **2021**, *9*, 2100355.
3. Schmidt, L. C.; Pertegás, A.; Gonzalez-carrero, S.; Malinkiewicz, O.; Agouram, S.; Espallargas, G. M.; Bolink, H. J.; Galian, R. E.; Pérez-prieto, J.; González- carrero, S. Non-Template Synthesis of $CH_3NH_3PbBr_3$ Perovskite Nanoparticles. *J. Am. Chem. Soc*. **2014**, *136*, 850−853
4. Bauzá, A.; Mooibroek, T. J.; Frontera, A. Towards Design Strategies for Anion–π Interactions in Crystal Engineering. *CrystEngComm* **2016**, *18*, 10–23.
5. Muslimawati, R. M.; Manawan, M.; Bahtiar, A. Synthesis of Single Crystal Perovskite $MAPbBr_3$ by Using Anti-Solvent Vapor-Assisted Crystallization Method for X-Ray Photodetector Application. *J. Phys. Conf. Ser*. **2022**, *2344*, 012002.
6. Tauc, J.; Grigorovici, R.; Vancu, A. Optical Properties and Electronic Structure of Amorphous Germanium. Phys. *Status Solidi B* **1966**, *15*, 627–637.
7. Zhang, D.; Okamoto, T.; Biju, V. Thermodynamically and Kinetically Controlled Nucleation and Growth of Halide Perovskite Single Crystals. *Small* **2023**, 2304900.
8. Deng, Y. H.; Wang, Q.; Yuan, Y. B.; Huang, J. S. Vividly colorful hybrid perovskite solar cells by doctor-blade coating with perovskite photonic nanostructures. *Mater. Horiz*. **2015**, *2*, 578-583.
9. Millar, David P. Time-resolved fluorescence spectroscopy. *Curr. Opin. Struct. Biol*.

1996, *6*, 637-642.

10. Farwell, D. G.; Meier, J. D.; Park, J.; Sun, Y.; Coffman, H.; Poirier, B.; Marcu, L. Time-resolved fluorescence spectroscopy as a diagnostic technique of oral carcinoma: validation in the hamster buccal pouch model. *Arch. Otolaryngology Head Neck Surg*. **2021**, *136*, 126-133.
11. Cosci, A.; Nogueira, M. S.; Pratavieira, S.; Takahama, A.; de Souza Azevedo, R.; Kurachi, C. Time-resolved fluorescence spectroscopy for clinical diagnosis of actinic cheilitis. *Biomed. Opt. Express* **2016**, *7*, 4210-4219.
12. Diamandis, E. P. Immunoassays with time-resolved fluorescence spectroscopy: principles and applications. *Clin. Biochem*. **1998**, *21*, 139-150.
13. Bastiaens, P.; Squire, A. Fluorescence lifetime imaging microscopy: spatial resolution of biochemical processes in the cell. *Trends Cell Biol*. **1999**, 48-52.
14. Becker, W. Fluorescence lifetime imaging–techniques and applications. *J. Microsc*. **2012**, *247*, 119-136.

Chapter 3

Thermodynamically and kinetically controlled crystallization of $MAPbBr_3$ microcrystals

Abstract

Photovoltaics and next-generation optical devices are emerging applications for halide perovskites. While perovskite single crystals exhibit consistent optoelectronic characteristics, sample characteristics, and device performances are impacted by notable crystal size and density fluctuations, anisotropy, photoluminescence, defects, and carrier lifetime. With the use of the ideal concentration of *N*-cyclohexyl-2-pyrrolidone (CHP), the crystal nucleation-growth processes are thermodynamically separated and kinetically controlled to yield uniform size and shape FA/$MAPbBr_3$ single microcrystals (MCs), the size of the crystals, size distributions, and the PL lifetime are all determined. The crystal growth rate is evaluated by detecting lead concentration in the precursor solution. By carefully adding the pyrrolidone derivative, homogeneous size distribution MCs with high-density cubic shape, high PL intensities, and long PL lifetimes are prepared at high temperatures in minutes. In contrast, the crystal size increases nonlinearly with time at low temperatures. The maximum PL intensity and longest PL lifetime is obtained from the crystals synthesized at 190 °C and 20 % CHP. This technique provides a way to synthesize highly isotropic and high-quality $MAPbBr_3$ perovskite microcrystals.

3.1 Introduction

The distinct bandgap and excitonic characteristics of organic-inorganic halide perovskites (HPs) make them a viable substitute for traditional semiconductors.[1-8] Scaling from micrometer to millimeter, outstanding and consistent characteristics such as low trap densities and long carrier lifetimes are shown by HP single crystals. HP single crystals have been produced in large quantities for use in various devices.[9-10] High-grade HP single crystals with regulated size and shape are essential for photodetectors,[11] wearable devices[12], lasers,[13] LEDs,[14-15] and solar cells[16-17]. The quality and reproducibility of fabricated devices are affected by the disparities in defect densities, carrier lifetimes, and inhomogeneous crystal sizes and shapes found in HPs synthesized using traditional methods.

Typical techniques used to prepare perovskite single crystals include antisolvent vapor-assisted crystallization (AVC), room temperature crystallization (RTC) and inverse temperature crystallization (ITC) methods. Using silicon oil and a room-temperature liquid diffusion-separation-induced crystallization technique, Yao et al. produced a massive $MAPbBr_3$ single crystal. The solvent in the precursor reduces and leads to an increase in precursor concentration. The synthesized single crystals exhibit a 92 % photoluminescence quantum yield, a low reap density, and an extended photoluminescence lifetime (1 μs).[18] Saidaminov et al. utilized the ITC method to prepare millimeter-size $MAPbBr_3$ and $MAPbI_3$ single crystals; high-quality crystals were obtained by this method. The AVC method is used to fabricate 100 mm^3 crack-free $MAPbBr_3$ single crystals, as reported by Shi et al.[19] For the AVC method, precursor solubility was reduced by antisolvent vapor diffusion in a precursor solution, which allowed perovskite crystallization to proceed. The synthesized large single crystals show a long carrier diffusion length and low trap density. Even though a variety of perovskite crystallization techniques based on the techniques mentioned above have been published, the microcrystal (MC) samples produced by these techniques vary greatly in terms of size,

shape, particle density, PL intensities, defects, and PL lifetimes. These characteristics adversely affect perovskite device performance and reproducibility.

N-cyclohexyl-2-pyrrolidone (CHP), an additive that controls the HP crystal shape, has been used in perovskite crystallization, according to reports from several groups.[20-22] Jeon et al. used CHP as an agent to adjust the crystal shape and create a homogenous perovskite film.[22] Garcia-Aboal et al. used the spin-coating method and the addition of CHP to show how to synthesize $MAPbBr_3$ crystals with uniform size and shape.[20] According to these reports, CHP is a great additive for managing the shape of perovskite crystals, because of its unique physical properties. CHP slows the rate at which solvent evaporation induces crystallization, which affects crystal growth. The precise mechanism by which CHP regulates the form of perovskite microcapsules is still unknown. Furthermore, the correlation between the CHP ratio, temperature, crystal size, crystal defect density, PL intensity, and PL lifetime is still unknown.

This chapter introduces the ITC method with CHP to synthesize FA/$MAPbBr_3$ MCs with uniform sizes, cubic shapes, low defect densities and long PL lifetimes. I looked into how the crystal growth temperature and CHP concentration affect the crystal density, size, shape, and PL quality. Additionally, I present a comparative analysis of the dimensions and morphology of $MAPbBr_3$ MCs with other halide perovskite bulk crystallization techniques. I expanded this method to other halide perovskites like $MAPbI_3$, $FAPbBr_3$, and $FAPbI_3$. I described how the CHP ratio and the reaction temperature affect the nucleation and growth rates of crystals, resulting in precisely controlled halide perovskite microcrystals concerning size, shape, and optical properties.

3.2 Results and discussion

3.2.1 $MAPbBr_3$ microcrystal preparation by conventional methods

Various conventional methods such as ITC, AVC, and RTC help synthesize large $MAPbBr_3$ single crystals. The synthesis details are given in chapter 2. The morphologies of as-synthesized crystals were measured using the optical microscope. The PL images

were collected by exciting the crystals using a picosecond laser (1 MHz, 45 ps, 460 nm). The PL decay and PL spectra were collected by a time-correlated single-photon counting (TCSPC) system and a fiber spectrometer (Ocean Optics-QE65 Pro).

The optical microscope and PL images reveal the crystal morphologies of conventional synthesis methods are irregular and inhomogeneous. As shown in Figure

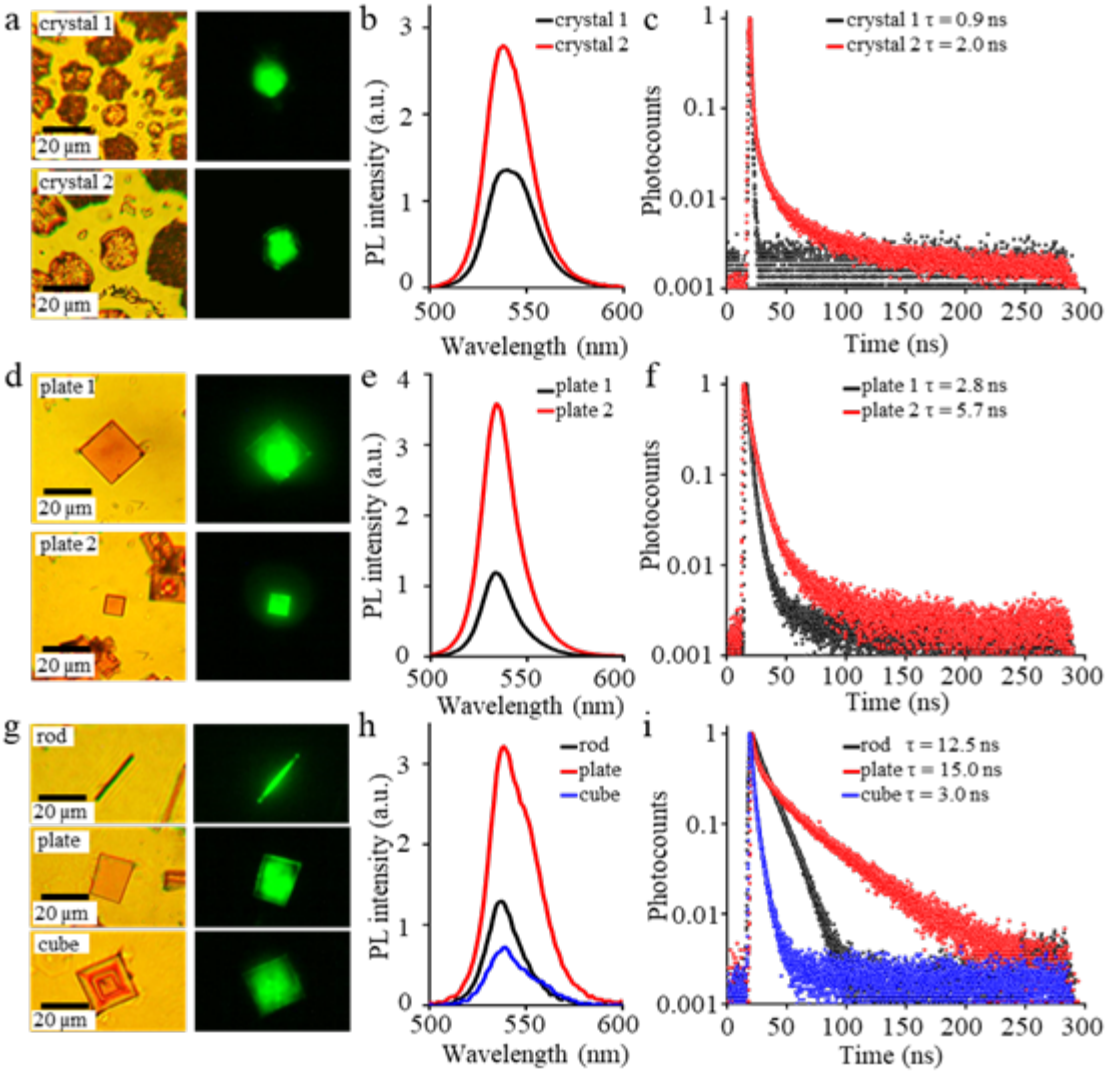

Figure 3.1. $MAPbBr_3$ crystals synthesized without CHP. (a, d, g) Optical and microscope images. (b, e, h) PL spectra and (c, f, i) PL decays of $MAPbBr_3$ MCs prepared by the ITC, AVC and RTC methods, respectively.

3.1a, the crystal shapes are irregular for those prepared by the ITC method; among all the irregular crystals, I selected two crystals for the optical and PL decay measurement; both crystals show green emission at 540 and 538 nm, respectively (Figure 3.1b). Figure 3.1c shows the PL lifetimes of both crystals (1 and 2); the longer PL lifetime (2.0 ns) for crystal 2 corresponds with its intense PL, and crystal 1 shows a shorter PL lifetime (0.9 ns) and weaker PL intensity. Figure 3.1d shows two microplates obtained from the AVC method; the sizes of the plates ranged from 5 to 30 μm. The PL spectra and lifetimes of plates 1 and 2 are shown in Figure 3.1e, f; the longer PL lifetime (5.7 ns) for plate 2 corresponds to its intense PL emission. The shorter lifetime (2.8 ns) for plate 1 is consistent with its weak PL intensity; both plates show the PL maxima at 533 nm. The RTC methods provided MCs with rod, cube and plate shapes, and they exhibited the PL spectral maximum at around 538 nm (Figure 3.1h). The microcrystals prepared by this method show variations in the PL intensities and lifetimes (Figure 3.1h, i); the longest PL lifetime was from a microplate (15 ns), the shortest from a microcube (3 ns), and 12.5 ns was for a microrod.

3.2.2 Correlation between CHP concentration with the crystal size and density

To investigate the correlation between the additive's (CHP) concentration with the crystal size and density, I synthesized $MAPbBr_3$ single crystals by a modified ITC method at various CHP concentrations (0, 2, 5, 10, 20). The crystal size increased with the increase in CHP concentration (Figure 3.2), and the crystal density decreased with the rise in CHP concentration. This is because the high boiling point and low vapor pressure of CHP induce the slow crystallization speed; the slower crystallization speed helps form fewer nuclei and crystals and a lower crystal density.

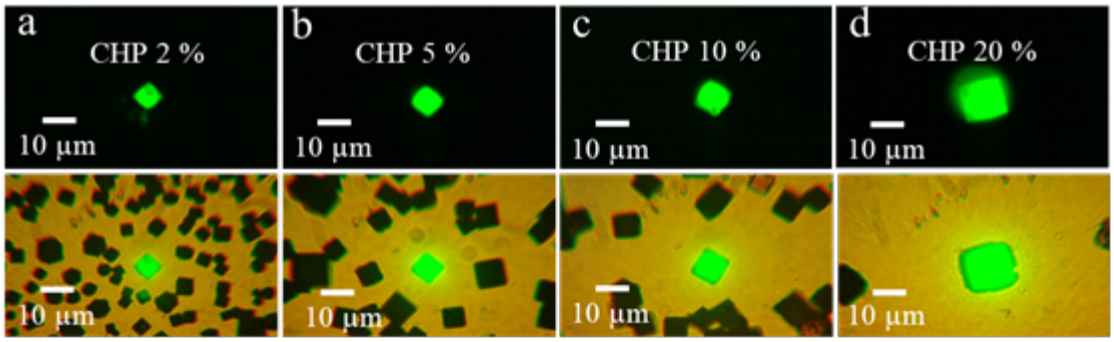

Figure 3.2. $MAPbBr_3$ crystals synthesized by different CHP concentrations. (a–d) PL and optical images of $MAPbBr_3$ MCs.

The average crystal size (d_{mean}) is increased from 5.8 to 17.9 µm with the CHP concentration increase from 2 to 20 %, and a broad size distribution CV=25.4% was calculated from 2 % CHP condition. In contrast, a narrow size distribution (CV=14.1%) was obtained with 20% CHP. Due to the increase in crystal size, the crystal density decreased from 6×10^9 m^{-2} to 4.3×10^8 m^{-2} (Figure 3.3).

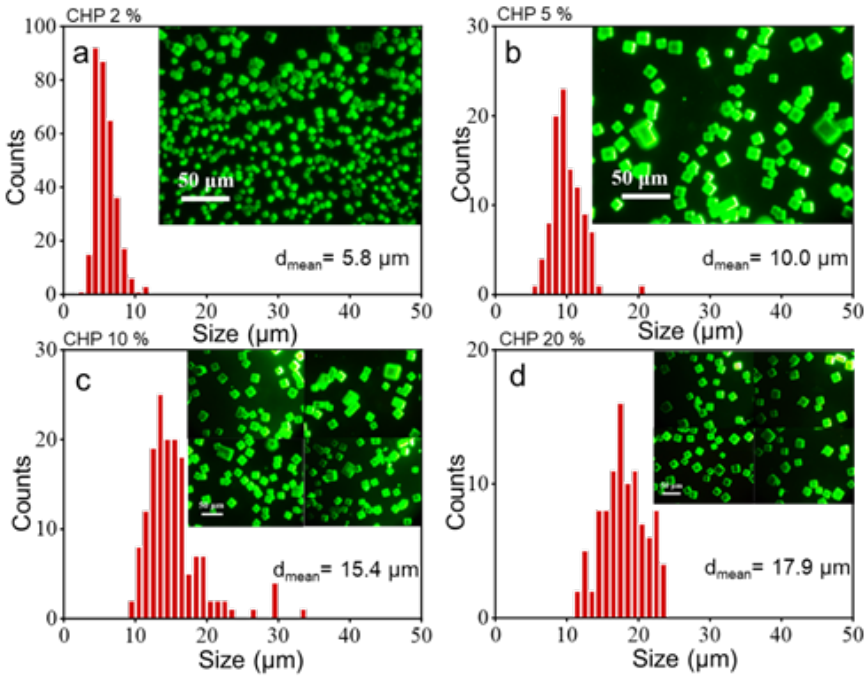

Figure 3.3. $MAPbBr_3$ crystals synthesized by adding different CHP concentrations. (a–d) Size distribution of MCs obtained by the ITC method with 2%, 5%, 10%, and 20% CHP (in DMF).

3.2.3 The influence of CHP concentration on the PL intensity and lifetime

I studied the influence of CHP concentration on the PL intensity and PL lifetime of MCs. Figure 3.4a shows the PL intensity vibration with different CHP concentrations; the crystals prepared with 20% CHP 20 showed the highest PL intensity and most extended lifetime compared with other crystals. Figure 3.4b, c shows the average PL lifetimes collected from three different crystals for each condition. The τ_{av} of crystals obtained from 0% CHP condition is 1.7 ns (Figure 3.4b, d). The crystal shape and size were completely different in the 0-10% range CHP concentration, but the PL lifetimes were in the range 1.6-1.8 ns (Figure 3.4c, d). The PL properties, such as quantum efficiency, charge carrier lifetime, and diffusion lengths of perovskite MCs, is significantly reduced by nonradiative recombination in defects, like vacancies, line defects, anti-sites, interstitials, impurities, or grain boundaries.[23-30]

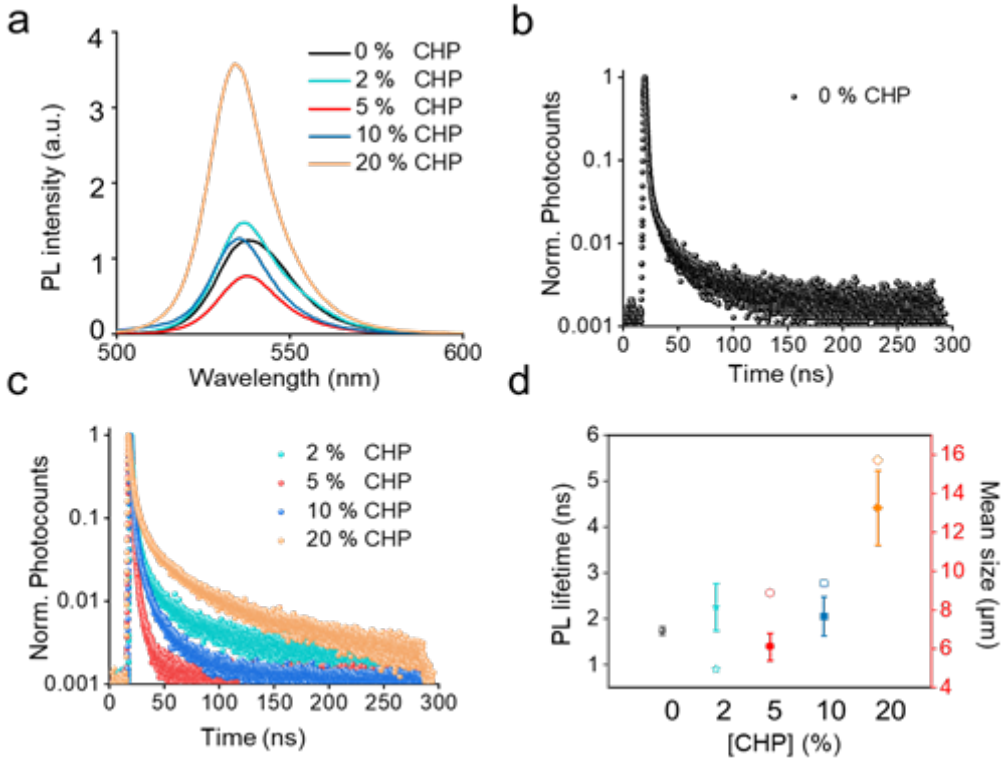

Figure 3.4. (a) PL spectra and (b, c) decays of $MAPbBr_3$ MCs. (d) The correlation between average particle size and PL lifetimes.

3.2.4 The crystallization model and kinetics

The crystallization process is divided into three stages: before nucleation, nucleation-growth, and crystal growth, according to LaMer's crystal nucleation and growth theory.[31-34] Modified LaMer diagrams for $MAPbBr_3$ MC formation are displayed in Figure 3.5a. Throughout the $MAPbBr_3$ crystallization process, the reaction temperature remained constant. Larger (<4 mL) sample volumes were used to reduce solvent evaporation by heating, which is the primary cause of the precursor concentration increase. When the concentration of the precursor reaches the critical concentration, C_{su}, nucleation begins. Following a decrease in the concentration due to nucleation below the critical concentration, the main process in crystal growth. Precursor diffusion allowed crystal growth to continue after nucleation ceased as the precursor concentration fell below the nucleation threshold C_n. The growth-dissolution (C_s) processes eventually came to an equilibrium.

The correlation between the k_n and ΔG_c is displayed in eq. (1) and (2),

$$k_n = \mathrm{A}\exp\left(\frac{-\triangle G_c}{k_B T}\right) \quad (1)$$

$$\triangle G_c = \left(\frac{16}{3}\right)\Pi\left(\frac{\triangle_\mu}{V_M}\right)^2\gamma^3 \quad (2)$$

In equation (1), A is a constant, T is the reaction temperature, k_B is the Boltzmann constant, and k_n is the nucleation speed. In equation (2), V_M refers to the crystal nucleus' molar volume, Δ_μ represents the discrepancies of precursor solutes and nucleus on the chemical potential. γ is the specific surface energy of the solid-liquid interface. k_n and T have a positive relationship. These equations suggest that high-speed nucleation occurs at higher temperatures.

The ΔG_s and k_g are calculated using eq. (3) and (4),

$$k_g = Bexp\left(\frac{-\triangle G_s}{k_B T}\right) \quad (3)$$

$$\triangle G_s = E_A - E_s \quad (4)$$

In equation (3), k_g is the crystal growth speed, B is a constant, T is the temperature.

In equation (4), ΔG_s is the free energy barrier height, E_A and E_S are the surface energies of crystal growth in different directions.

The surface energy at E_{s1} and E_{s2} correspond to crystal growth along the normal and lateral sides, as shown in Figure 3.5b. So that $\Delta G_{S2} - \Delta G_{S1} = E_{S2} - E_{S1}$. The crystal growth rate ratio (k_{gS2}/k_{gS1}) is given by eq. (5),

$$\frac{k_{gs2}}{k_{gs1}} = exp\frac{E_{s2}-E_{S1}}{k_B T} \qquad (5)$$

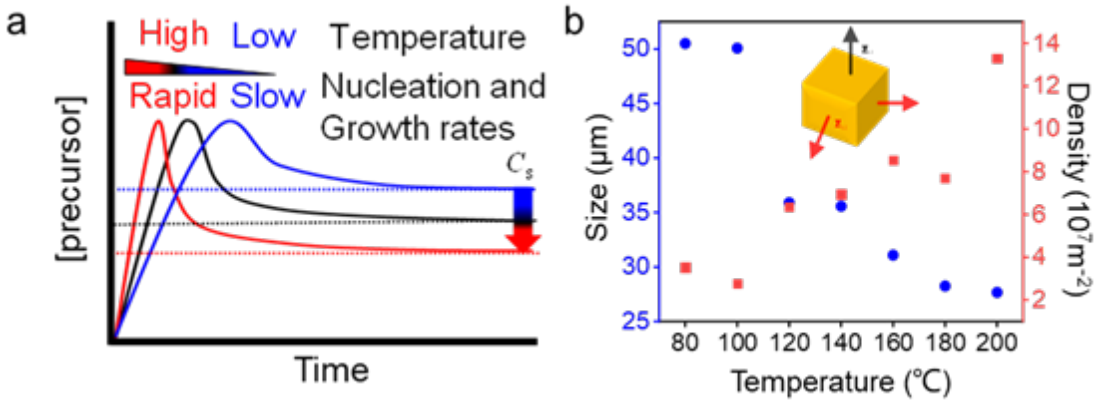

Figure 3.5. (a) Modified LaMer diagrams for $MAPbBr_3$ MC crystallization under different temperatures. (b) The relationship between the reaction temperature with crystal size and density. Inset is a scheme of the crystal growth on normal and lateral sides.

In the case of surface energy showing a huge difference and a low temperature [($E_{S2} - E_{S1}$)>>k_BT], the crystal growth speed is very large [k_{gS2}/k_{gS1}>>1]. As a result, the crystallization process at low temperatures produces anisotropic crystals like rods and plates. Conversely, at high temperatures and less difference between the two surface energy components [($E_{S2} - E_{S1}$)<<k_BT], the crystal growth speed becomes equal [$k_{gS2}/k_{gS1} \simeq e^0$]. Adding CHP creates a higher reaction temperature (>80 °C); therefore, cubic $MAPbBr_3$ MCs form. The microcrystal size and density are correlated with the CHP ratio and temperature.

I used the commercial Pb^{2+} sensor PAR (4-(2-pyridylazo) resorcinol) to measure the correlation between the reaction time and crystal formation rate at various temperatures. The relationship of the Pb^{2+} reaction product with the PAR (4-(2-pyridylazo) resorcinol) sensor is displayed in Figures 3.6a, b. As the Pb^{2+} concentration rises, the product's absorbance increases linearly.

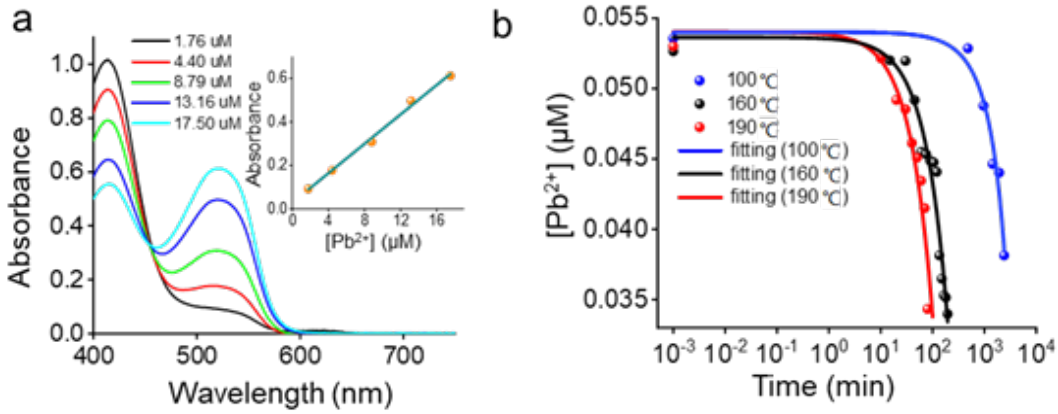

Figure 3.6. (a) The correlation of PAR sensor absorbance with an increasing Pb^{2+} concentration; inset: the calibration curve for detecting Pb^{2+} concentration in standard $Pb(NO_3)_2$ solutions using the PAR sensor. (b) The relationship of reaction time with Pb^{2+} concentrations.

I employed standard Pb^{2+} solutions to standardize the ion sensing by PAR, and the resulting linear absorption-Pb^{2+} concentration relation is displayed in the inset of Figure3.6a. Pb^{2+} concentration decreases as reaction time increases, as seen in Figure 3.6b. For a 4 mL precursor solution, the crystallization process takes 40 hours at a low temperature of 100 °C; however, at 190 °C, the crystallization process takes 80 minutes to complete. Due to Pb^{2+} consumption by the nuclei and crystal formation, the Pb^{2+} concentration in the reaction solution decreases as the reaction time increases. Additionally, as the reaction time increased, the Pb^{2+} concentration dropped, indicating that CHP has a thermodynamic and kinetic impact on the crystallization process.

3.2.5 The universality of the modified ITC method

To investigate the other types of perovskites, I measured the crystal morphology and PL spectra of $FAPbBr_3$, $FAPbI_3$, and $MAPbI_3$ MCs, all with or without CHP. In the presence of 10% to 20% CHP, iodide ($FAbI_3$ and $MAPbI_3$) perovskite MCs did not form cubic microcrystals, but $FAPbBr_3$ formed cuboid crystals (Figure 3.7a). On the other hand, the PL intensity was enhanced by CHP in all the samples (Figure 3.7b–d).

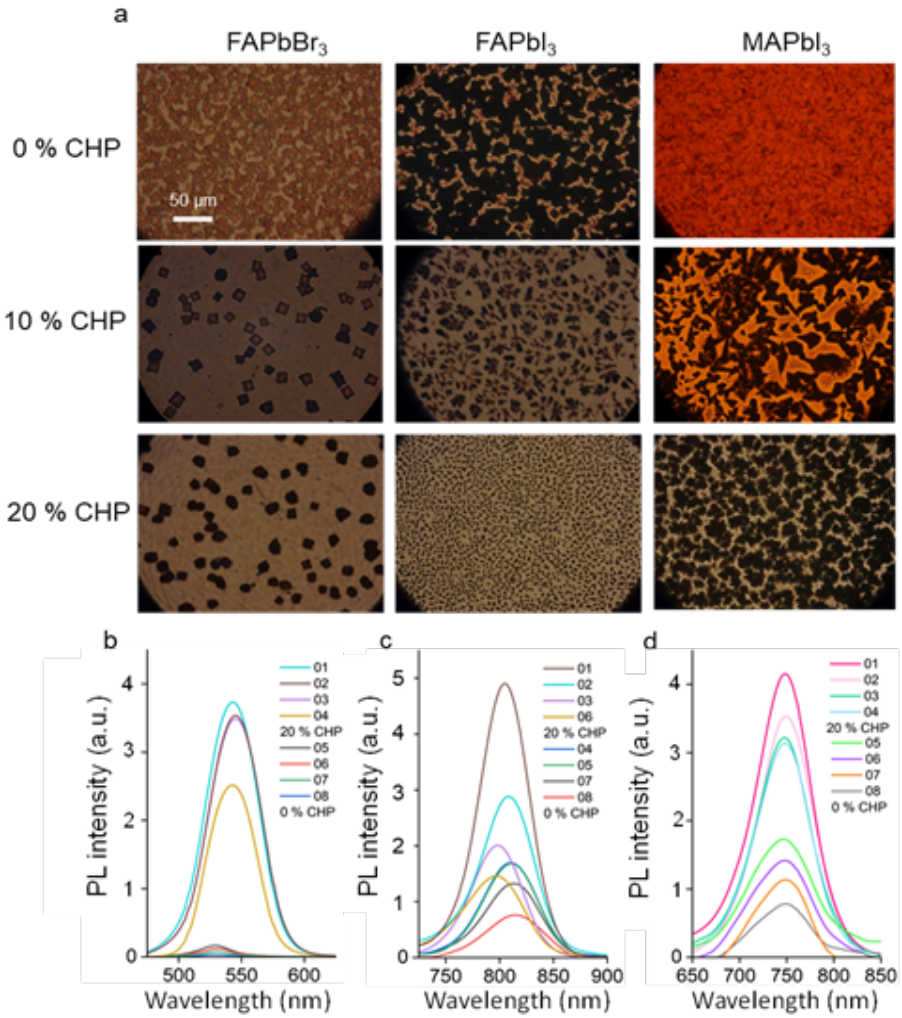

Figure 3.7. (a) Optical microscope images of $FAPbBr_3$, $FAbI_3$, and $MAPbI_3$ MCs prepared without and with CHP in DMF. (b)-(d) PL spectra of $FAPbBr_3$, $FAbI_3$, and $MAPbI_3$ MCs prepared without and with 20% CHP.

3.3 Conclusions

I demonstrate the effective use of a finite amount of CHP to regulate the thermodynamics of crystal nucleation and kinetics of crystal growth, influencing the size, shape, density, and defects of $MAPbBr_3$ MCs. The conventional methods, like AVC produce perovskite microplates; the RTC method yields mixed shape crystals (cuboid, plate, and rod), and ITC without CHP results in irregular microcrystals. By incorporating CHP into the ITC method, uniform perovskite MCs with extended PL lifetimes are synthesized. The nucleation and growth of perovskite crystals are systematically controlled by adjusting temperature and CHP ratio. Crystallization at low temperatures or with a low CHP ratio leads to anisotropic samples due to slow nucleation and fast crystal growth kinetics. Conversely, fast nucleation followed by slow crystal growth, achieved through high-temperature crystallization with 20% CHP, produces high-density, homogeneous, cubic crystals with fewer defects. This approach enables the fabrication of high-quality perovskite crystals for devices using isotropic single crystals that are kinetically and thermodynamically controlled.

References

1. Tong, X.; Lin, F.; Wu, J.; Wang, Z. M. High Performance Perovskite Solar Cells. *Adv. Sci.* **2016**, *3*, 1500201.
2. Zhao, L.; Luo, D.; Wu, J.; Hu, Q.; Zhang, W.; Chen, K.; Liu, T.; Liu, Y.; Zhang, Y.; Liu, F.; Russell, T. P.; Snaith, H. J.; Zhu, R.; Gong, Q. High-Performance Inverted Planar Heterojunction Perovskite Solar Cells Based on Lead Acetate Precursor with Efficiency Exceeding 18%. *Adv. Funct. Mater.* **2016**, *26*, 3508–3514.
3. Chen, X.; Yang, S.; Zheng, Y. C.; Chen, Y.; Hou, Y.; Yang, X. H.; Yang, H. G. Multifunctional Inverse Opal-Like TiO_2 Electron Transport Layer for Efficient Hybrid Perovskite Solar Cells. *Adv. Sci.* **2015**, *2*, 1500105.
4. Zhong, Y.; Xu, L.; Li, C.; Zhang, B.; Wu, W. Needle Coke: A Predominant Carbon Black Alternative for Printable Triple Mesoscopic Perovskite Solar Cells. *Carbon* **2019**, *153*, 602–608.
5. He, H.; Yang, Z.; Xu, Y.; Smith, A. T.; Yang, G.; Sun, L. Perovskite Oxides as Transparent Semiconductors: A Review. *Nano Converg.* **2020**, *7*, 32.
6. Kour, R.; Arya, S.; Verma, S.; Gupta, J.; Bandhoria, P.; Bharti, V.; Datt, R.; Gupta, V. Potential Substitutes for Replacement of Lead in Perovskite Solar Cells: A Review. *Glob. Chall.* **2019**, *3*, 1900050.
7. Zhang, C.; Shen, T.; Guo, D.; Tang, L.; Yang, K.; Deng, H. Reviewing and Understanding the Stability Mechanism of Halide Perovskite Solar Cells. *InfoMat.* **2020**, *2*, 1034–1056.
8. Wang, Z.; Shi, Z.; Li, T.; Chen, Y.; Huang, W. Stability of Perovskite Solar Cells: A Prospective on the Substitution of the A Cation and X Anion. *Angew. Chem. Int. Ed.* **2017**, *56*, 1190–1212.

9. Hussain, I.; Tran, H. P.; Jaksik, J.; Moore, J.; Islam, N.; Uddin, M. J. Functional Materials, Device Architecture, and Flexibility of Perovskite Solar Cell. *Emergent Mater*. **2018**, *1*, 133–154.

10. Cai, M.; Wu, Y.; Chen, H.; Yang, X.; Qiang, Y.; Han, L. Cost-Performance Analysis of Perovskite Solar Modules. *Adv. Sci.* **2017**, *4*, 1600269.

11. Liu, D.; Yu, B. B.; Liao, M.; Jin, Z.; Zhou, L.; Zhang, X.; Wang, F.; He, H.; Gatti, T.; He, Z. Self-Powered and Broadband Lead-Free Inorganic Perovskite Photodetector with High Stability. *ACS Appl. Mater. Interfaces* **2020**, *12*, 30530–30537.

12. Hu, X.; Li, F.; Song, Y. Wearable Power Source: A Newfangled Feasibility for Perovskite Photovoltaics. *ACS Energy Lett*. **2019**, *4*, 1065–1072.

13. Eaton, S. W.; Lai, M.; Gibson, N. A.; Wong, A. B.; Dou, L.; Ma, J.; Wang, L. W.; Leone, S. R.; Yang, P. Lasing in Robust Cesium Lead Halide Perovskite Nanowires. *Proc. Natl. Acad. Sci.* **2016**, *113*, 1993–1998.

14. Zhang, S.; Yi, C.; Wang, N.; Sun, Y.; Zou, W.; Wei, Y.; Cao, Y.; Miao, Y.; Li, R.; Yin, Y.; Zhao, N.; Wang, J.; Huang, W. Efficient Red Perovskite Light-Emitting Diodes Based on Solution-Processed Multiple Quantum Wells. *Adv. Mater.* **2017**, *29*, 1606600.

15. Cho, C.; Zhao, B.; Tainter, G. D.; Lee, J. Y.; Friend, R. H.; Di, D.; Deschler, F.; Greenham, N. C. The Role of Photon Recycling in Perovskite Light-Emitting Diodes. *Nat. Commun.* **2020**, *11*, 611.

16. Im, J.-H.; Jang, I. H.; Pellet, N.; Grätzel, M.; Park, N.-G. Growth of $CH_3NH_3PbI_3$ Cuboids with Controlled Size for High-Efficiency Perovskite Solar Cells. *Nat. Nanotechnol.* **2014**, *9*, 927–932.

17. Haruyama, J.; Sodeyama, K.; Han, L.; Tateyama, Y. Surface Properties of $CH_3NH_3PbI_3$ for Perovskite Solar Cells. *Acc. Chem. Res*. **2016**, *49*, 554–561.

18. Yao, F.; Peng, J.; Li, R.; Li, W.; Gui, P.; Li, B.; Liu, C.; Tao, C.; Lin, Q.; Fang, G. Room-Temperature Liquid Diffused Separation Induced Crystallization for High-Quality Perovskite Single Crystals. *Nat. Commun.* **2020,** *11*, 1194.

19. Saidaminov, M. I.; Abdelhady, A. L.; Murali, B.; Alarousu, E.; Burlakov, V. M.; Peng, W.; Dursun, I.; Wang, L.; He, Y.; Maculan, G.; Goriely, A.; Wu, T.; Mohammed, O. F.; Bakr, O. M. High-Quality Bulk Hybrid Perovskite Single Crystals within Minutes by Inverse Temperature Crystallization. *Nat. Commun.* **2015**, *6*, 7586.

20. García-Aboal, R.; Fenollosa, R.; Ramiro-Manzano, F.; Rodríguez, I.; Meseguer, F.; Atienzar, P. Single Crystal Growth of Hybrid Lead Bromide Perovskites Using a Spin-Coating Method. *ACS Omega* **2018**, *3*, 5229–5236.

21. Okamoto, T.; Shahjahan, Md.; Biju, V. Shape-Dependent Kinetics of Halide Vacancy Filling in Organolead Halide Perovskites. *Adv. Opt. Mater.* **2021**, *9*, 2100355.

22. Jeon, Y. J.; Lee, S.; Kang, R.; Kim, J. E.; Yeo, J. S.; Lee, S. H.; Kim, S. S.; Yun, J. M.; Kim, D. Y. Planar Heterojunction Perovskite Solar Cells with Superior Reproducibility. *Sci. Rep.* **2014**, *4*, 6953.

23. Phung, N.; Al-Ashouri, A.; Meloni, S.; Mattoni, A.; Albrecht, S.; Unger, E. L.; Merdasa, A.; Abate, A. The Role of Grain Boundaries on Ionic Defect Migration in Metal Halide Perovskites. *Adv. Energy Mater*. **2020**, *10*, 1903735.

24. Sherkar, T. S.; Momblona, C.; Gil-Escrig, L.; Ávila, J.; Sessolo, M.; Bolink, H. J.; Koster, L. J. A. Recombination in Perovskite Solar Cells: Significance of Grain

Boundaries, Interface Traps, and Defect Ions. *ACS Energy Lett*. **2017**, *2*, 1214–1222.

25. Kaiser, W.; Hussain, K.; Singh, A.; Alothman, A. A.; Meggiolaro, D.; Gagliardi, A.; Mosconi, E.; De Angelis, F. Defect Formation and Healing at Grain Boundaries in Lead-Halide Perovskites. *J. Mater. Chem. A* **2022**, *10*, 24854–24865.
26. Ochoa-Martinez, E.; Ochoa, M.; Ortuso, R. D.; Ferdowsi, P.; Carron, R.; Tiwari, A. N.; Steiner, U.; Saliba, M. Physical Passivation of Grain Boundaries and Defects in Perovskite Solar Cells by an Isolating Thin Polymer. *ACS Energy Lett.* **2021**, *6*, 2626–2634.
27. Shan, W.; Saidi, W. A. Segregation of Native Defects to the Grain Boundaries in Methylammonium Lead Iodide Perovskite. *J. Phys. Chem. Lett*. **2017**, *8*, 5935–5942.
28. Mattoni, A.; Meloni, S. Defect Dynamics in $MAPbI_3$ Polycrystalline Films: The Trapping Effect of Grain Boundaries. *Helv. Chim. Acta.* **2020**, *103*, e2000110.
29. Knight, A. J.; Patel, J. B.; Snaith, H. J.; Johnston, M. B.; Herz, L. M. Trap States, Electric Fields, and Phase Segregation in Mixed-Halide Perovskite Photovoltaic Devices. *Adv. Energy Mater.* **2020**, *10*, 1903488.
30. Wang, F.; Bai, S.; Tress, W.; Hagfeldt, A.; Gao, F. Defects Engineering for High-Performance Perovskite Solar Cells. *npj Flex. Electron.* **2018**, *2*, 22.
31. LaMer, V. K.; Dinegar, R. H. Theory, Production and Mechanism of Formation of Monodispersed Hydrosols. *J. Am. Chem. Soc*. **1950**, *72*, 4847–4854.
32. Yoreo, J. J. D.; Vekilov, P. G. Principles of Crystal Nucleation and Growth. *Rev. Mineral. Geochem*. **2003**, *54*, 57–93.
33. Chen, Y.; Zeng, H.; Ma, P.; Chen, G.; Jian, J.; Sun, X.; Li, X.; Wang, H.; Yin, W.; Jia, Q.; Zou, G. Overcoming the Anisotropic Growth Limitations of Free-Standing

Single-Crystal Halide Perovskite Films. *Angew. Chem. Int. Ed.* **2021**, *60*, 2629–2636.

34. Whitehead, C. B.; Özkar, S.; Finke, R. G. LaMer's 1950 Model for Particle Formation of Instantaneous Nucleation and Diffusion-Controlled Growth: A Historical Look at the Model's Origins, Assumptions, Equations, and Underlying Sulfur Sol Formation Kinetics Data. *Chem. Mater*. **2019**, *31*, 7116–7132.

Chapter 4
Light-soaking-induced halide ion migration and trap healing

Abstract

Halide perovskite microcrystals are expected to be the candidate for fabricating brilliantly luminescent, cost-effective, and stable perovskite light-emitting diodes because of low defects and tunable bandgaps. $MAPbBr_3$ microcrystals are directly synthesized on indium-coated tin oxide glass plates at room temperature using a doctor-blading method. The synthesized samples show micron-sized cubic single crystals. The crystals emit bright green photoluminescence under a 465 nm laser irradiation and green electroluminescence with continuous blinking at 3 V. Considering a relation between halogen vacancies and luminescence blinking, I investigate the optical activation of $MAPbBr_3$ microcrystals to increase the anion diffusion rate, vacancy redistribution, and blinking suppression. The light-soaking effect on electroluminescence blinking is studied by photoactivating the crystals with a light intensity below the threshold for photoluminescence while biased with 3 V or larger potentials. Electroluminescence intensity trajectories are collected for more than 100 single crystals before, during, and after real-time light-soaking. The electroluminescence ON and OFF probabilities are separately analyzed for the same single crystals during the three stages. In addition, the thermal effect on the EL blinking is also studied by heating the crystals with an optically transparent hot plate set at 50 ℃ to understand the role of the photothermal effect on halogen migration, vacancy redistribution, and electroluminescence blinking. Furthermore, the light-soaking effect on the PL lifetime is investigated. An increase in the ON time, a decrease in the OFF time, and an increased electroluminescence intensity are observed under light-soaking, suggesting light-induced halide ion migration redistributes halogen vacancies and increases the probability of radiative carrier

recombination. Also, an increase in the photoluminescence lifetime is detected for the light-soaked crystals during lifetime measurement. Finally, the mechanism of the light-soaking effect on electroluminescence blinking and the photoluminescence lifetime is discussed from the viewpoint of light-induced halide ion migration and transient trap healing.

4.1 Introduction

Halide perovskites, with narrow and adjustable emission wavelengths[1-14] are a new breed of solar cell,[15-18] which can also be applied to light-emitting diodes (PeLEDs),[19-22] photodetectors,[23-26] lasers,[27-30] and other devices. Significant advancements in the performance of PeLEDs have been achieved in recent years. For example, the blue, red, and green colored LEDs external quantum efficiencies (EQEs) have been increased to 20%, 20%, and 10%, respectively.[31] After only a few years of development, the certified PCE of perovskite solar cells has reached >26%, matching the PCE record of single-crystal silicon solar cells. Nonetheless, perovskites' optoelectronic performance and practical applications still suffer from instability[32-35] and efficiency roll-off.[36-38] For solar cells and PeLEDs, numerous factors, such as ion migration,[39-40] Joule heating,[41] moisture,[42] and imbalanced carrier injection[43] have been connected to these drawbacks.

The ionic species in halide perovskites may migrate under some specific conditions, such as light irradiation, bias, or heating, and the activation energy determines the migration of the species (Figure 4.1).[44-46] The activation energy of different species has been experimentally measured. Generally, A-site cations and halide ions have a lower activation energy than B-site cations.[47] The ion migration can play positive and negative roles in the performance of halide perovskites. The ion migration-induced degradation of halide perovskite under light-soaking has been reported. Bastos et al. reported the degradation is correlated with the addition of 4-t-butyl pyridine, which is important to the hole transport layer of perovskite solar cells.[48] Zhao et al. revealed that the structure change under light illumination causes halide perovskite solar cells to be degraded.[49] Domanski et al. reported the reversible performance losses of perovskite solar cells induced by the cations' migration.[50] In contrast, Wu et al. suggested that light-soaking can passivate the interfacial traps to improve carrier transport efficiency.[51] Chen et al. found that continuous light illumination on $MAPbBr_3$ perovskite solar cells causes photoluminescence (PL) improvement and PL quenching at higher-intensity

illumination.[52] The reduction of trap density of perovskites during light illumination improves these efficiencies. In addition, thermal heating caused ion migration, PL, and electroluminescence (EL) quenching, and the improvement strategy has been investigated and reported. Liu et al. claimed that a post-synthesis fluoride treatment improves thermal stability and efficient charge injection of $CsPbBr_3$ perovskite nanocrystals. Compared with pristine nanocrystals, the treated nanocrystals show a low turn-on voltage and high external quantum efficiency (EQE).[53]

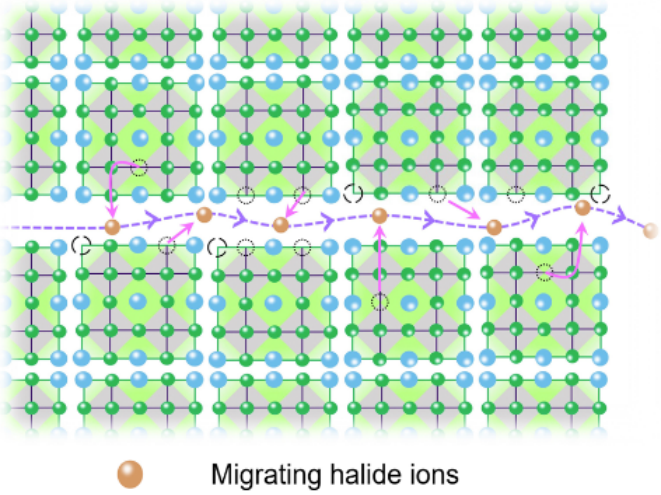

Figure 4.1. Halide ion migration by vacancy and grain boundary.[44]

However, the influence of light-soaking and thermal heating-induced ion migration on the EL and PL of perovskites has not yet been explored. In this chapter, I investigate the PL and EL enhancement induced by light-soaking and thermal heating, which are investigated in terms of EL blinking suppression under light irradiation with different power densities, with or without heating. Finally, I discuss the relationship among halogen vacancies, halide migration, and EL blinking.

4.2 Results and discussion

4.2.1 The structure-composition and energy diagram of devices

The bandgap of perovskite $MAPbBr_3$ is regarded as 2.36 eV. The minimum excitation

wavelength is calculated using Eg = 1240/λg (eV), resulting in 525 nm. Therefore, I utilized a 470-490 nm bandpass filter to extract the light for light-soaking, just above the bandgap energy. The EL device structure and the energy levels of individual components are shown in Figure 4.2.

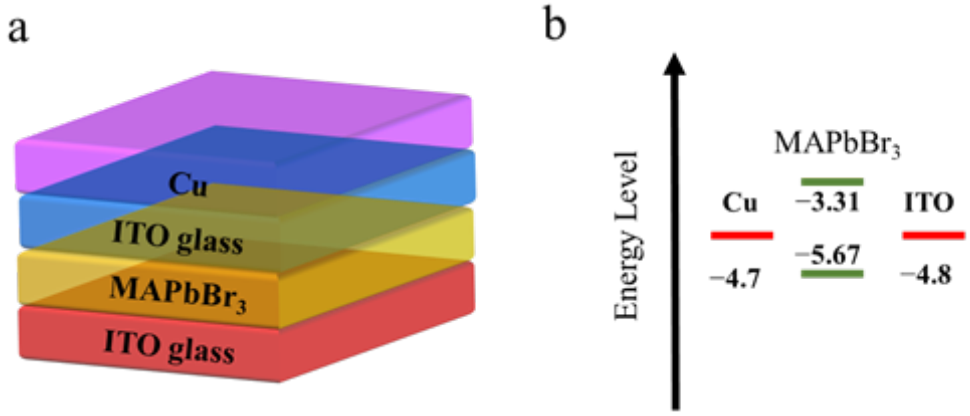

Figure 4.2. (a) Structure of the EL device. (b) Energy diagram of the device with the band positions of its components relative to the vacuum level.

4.2.2 $MAPbBr_3$ microcrystals preparation and characterization

The synthesis of perovskite $MAPbBr_3$ microcrystals is performed by a doctor-blading method at room temperature. In detail, equal volumes of 1 M MABr and 1 M $PbBr_3$ solutions in GBL are mixed to prepare a $MAPbBr_3$-GBL precursor solution. Then I dropped 20 µL $MAPbBr_3$-GBL precursor solution on an ITO glass, immediately blade-coated by another ITO to make a thin solution film on two ITO glass plates, repeated the

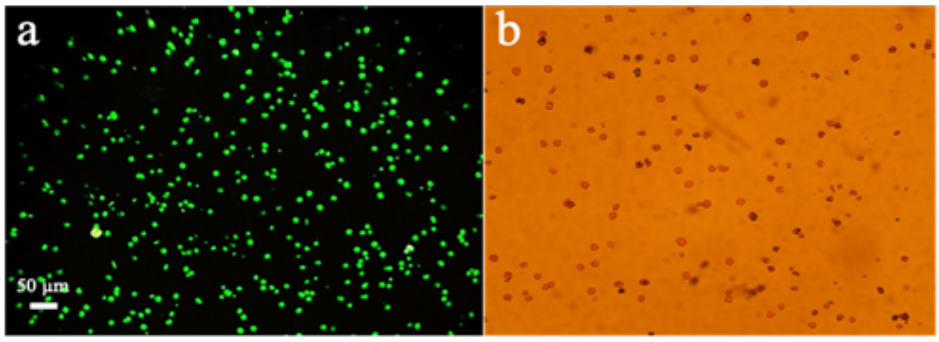

Figure 4.3. (a) PL and (b) microscope optical images of $MAPbBr_3$ MCs.

blading process to make sure there were no air bubbles within the two ITO plates, and waited for 30 minutes to complete crystallization.

The as-synthesized $MAPbBr_3$ crystals showed micron-sized single crystals (Figure 4.3); the crystal size ranged from 5 to 30 μm. When excited with a 465 nm picosecond laser, the crystals showed intense green emission. Figure 4.4a shows the PL and EL spectra collected from the as-synthesized $MAPbBr_3$ single crystals; it showed a PL maximum at 534 nm and an EL maximum at 538 nm. The slight peak shift is attributed to reabsorption-emission, depending on the EL center. Here, the PL was collected by exciting the crystal from the bottom and the emitted photons were collected through the same excitation objective lens, ruling out the possibility of reabsorption emission on the spectral shape or maximum. Conversely, the EL center can be anywhere within the crystal an emitting center vertically displaced from the objective lens causes reabsorption-emission-induced spectral redshift, which is reflected in the EL spectrum (Figure 4.4a). Figure 4.4b shows the green EL of the device operated at 5 V; the enlarged image shows individual EL crystals.

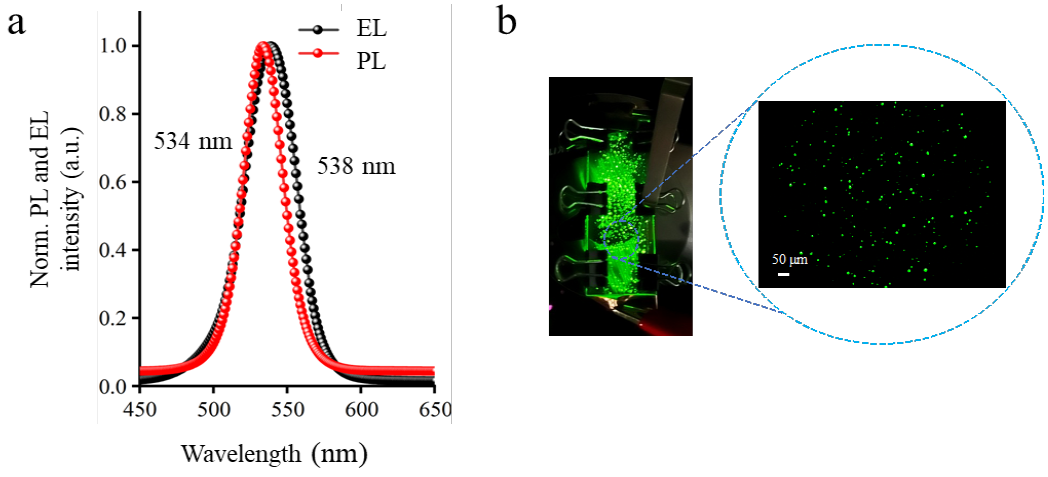

Figure 4.4. (a) PL and EL spectra collected from as-synthesized $MAPbBr_3$ MCs. The PL spectrum was collected by exciting crystals with a 465 nm picosecond laser, and the EL spectrum was collected by applying 5 V. (b) An EL image of the entire LED device and an enlarged EL image showing MCs in the device under 5 V.

Then, I investigated the light-soaking effect on the PL lifetime, which was recorded without or with light-soaking (405 nm LED) from two crystals. The results are shown in Figure 4.5. With light-soaking, the PL lifetime was increased from 1.8 to 3.3 ns for crystal 1 (Figure 4.5a) and from 2.2 to 5.1 ns for crystal 2 (Figure 4.5b). PL lifetime increase by photoactivation is reported for perovskites, which was attributed to increased ion mobility and halide vacancy filling.[54]

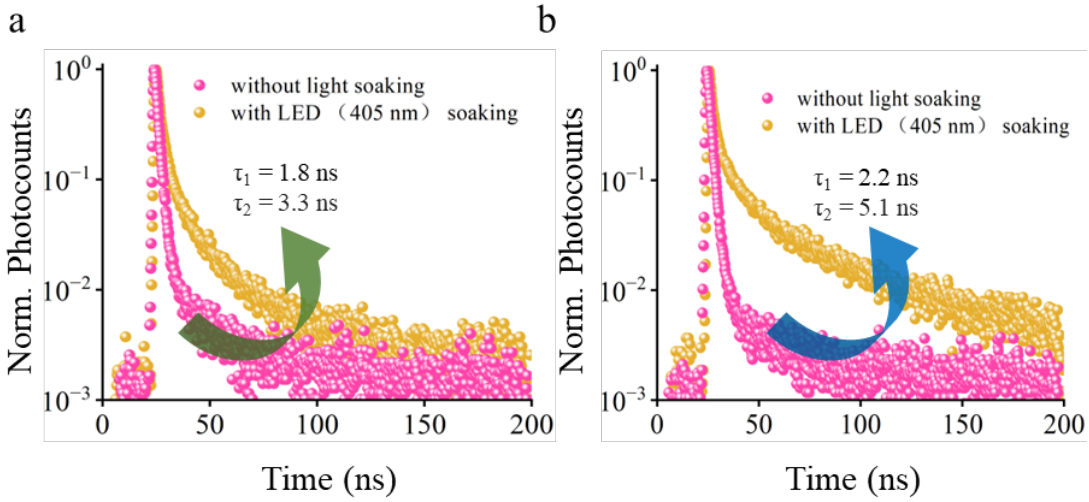

Figure 4.5. PL decays with and without light-soaking (405 nm cw LED) collected from two $MAPbBr_3$ MCs by exciting with 460 nm ps laser pulses (1 MHz, 45 ps).

I used a 405 nm LED as the light source, which is sufficient to excite the crystals from the ground state to the excited state. The light-induced halide ion migration and vacancy filling might have occurred under this condition, redistributing halide ions and vacancies, and increasing the PL lifetime.

Next, I investigated the light-soaking effect on EL blinking. Figure 4.6 shows three typical EL blinking trajectories with and without light soaking. The total recording time scale is 180 s, and the EL blinking trajectory is divided into three equal periods: 0-60 s and 120-180s are without light-soaking, and 60-120 s is with light-soaking. The long OFF time and low ON probability without light-soaking periods can be seen in all three time-windows. In contrast, the higher ON probability can be seen in the time window with light-soaking for all three trajectories in Figure 4.6. The increased intensity and ON

occurrences during the light-soaking period of the EL trajectory suggest that light-induced ion migration and vacancy filling can reduce the trap-assisted nonradiative recombination.

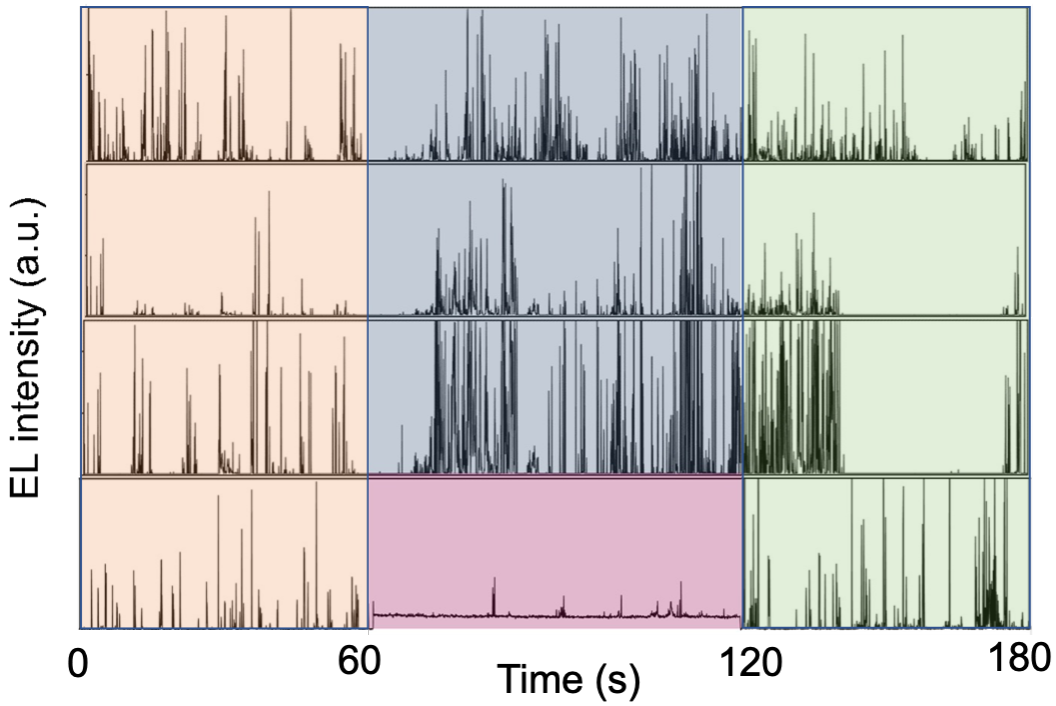

Figure 4.6. Three EL trajectories collected in 180 s under 5 V. The 0-60 and 120-180 s windows are without light-soaking, and the 60-120 s window is with light-soaking with 470-490 nm bandpass filtered light (5 mW cm^{-2}).

As light activation and electrical bias can induce healing the crystals, I also investigated the thermal effect on the EL blinking trajectory. I recorded EL blinking trajectories of the same single crystals at room temperature and 50 ℃. As shown in Figure 4.7, the 0-60 s and 120-180 s are the two blinking periods at room temperature, and 60-120 s is the blinking period at 50 ℃. From the result, the ON probability is increased during the thermal heating (50 ℃) compared with room temperature. Further, the thermal stability of the PL intensity and lifetime are studied, and it is found that the PL lifetime and intensity increase with the increase in temperature from 25 to 50 ℃, which is consistent with the literature.[55]

Further, I analyzed the ON and OFF times distribution for >100 single MCs to understand the statistics of the light-soaking effect. I set threshold intensities in each

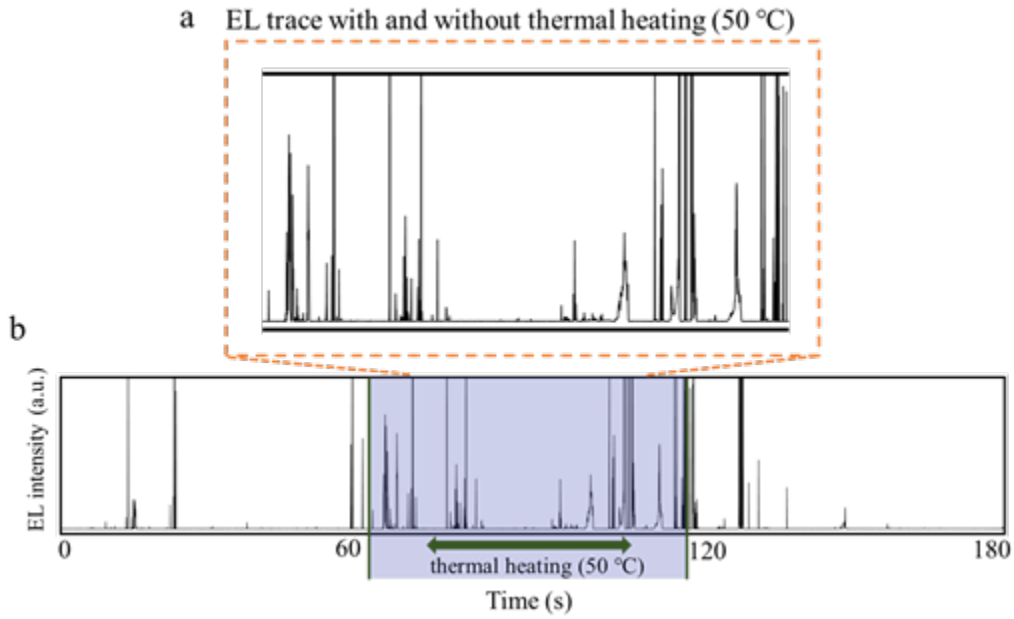

Figure 4.7. (b) An EL intensity trajectory of an MC at 5 V and at (0-60 s) room temperature, (60-120 s) 50 °C, and (120-180 s) room temperature. (a) The enlarged part of the trajectory in b during 60-120 s.

trajectory to determine the ON and OFF levels. If the intensity value is larger than the threshold value, it is determined as an ON event. In contrast, if the intensity value is smaller than the threshold, it is determined as an OFF event. The ON and OFF times are calculated by combining the continuously occurring events. The ON and OFF probability distribution is calculated using the following equation.

$$P(\tau_{ON/OFF}) = \frac{N(\tau_{ON/OFF})}{N^{tot}_{ON/OFF}} \frac{1}{\delta\tau_{ON/OFF}}$$

The ON and OFF probability distribution is plotted with a truncated power law:

$$P(\tau) = A_0 \tau^{-\alpha} e^{-\frac{\tau}{\tau_c}} \quad (1)$$

In this equation, A_0 stands for a constant, α refers to the power law coefficient, and τ_c stands for the truncation time.

$$P(\tau) = \frac{2N_i}{\tau_{i+1}} - (\tau_i + \tau_{i-1}) \quad (2)$$

Equation (2) is for the probability distribution calculation. In this equation, N_i refers

to i^{th} time's occurrence, and τ stands for the time.

To understand the effect of light-soaking on the EL blinking of $MAPbBr_3$ MCs, I plotted the statistic ON and OFF probability distribution from 110 EL blinking trajectories of single crystals with a truncated power law. Figure 4.8 shows the ON time truncation τ_c value is increased from 0.13 to 0.23, corresponding to the time without and with light-soaking, and the ON probability value $P\tau_{ON}$ is also increased. In contrast, the OFF-truncation time τ_c value is decreased from 2.91 to 2.13, corresponding to the time without and with light-soaking. The third part is that after the light-soaking period, both ON and OFF truncation times recovered to values close to the initial ones. The result suggests that the nonradiative recombination rate is decreased during the light-soaking and radiative recombination is increased. The light-induced halide ion migration and the trap healing by the migrated halide ions can be the dominant reasons for these changes to the ON and OFF times.[56]

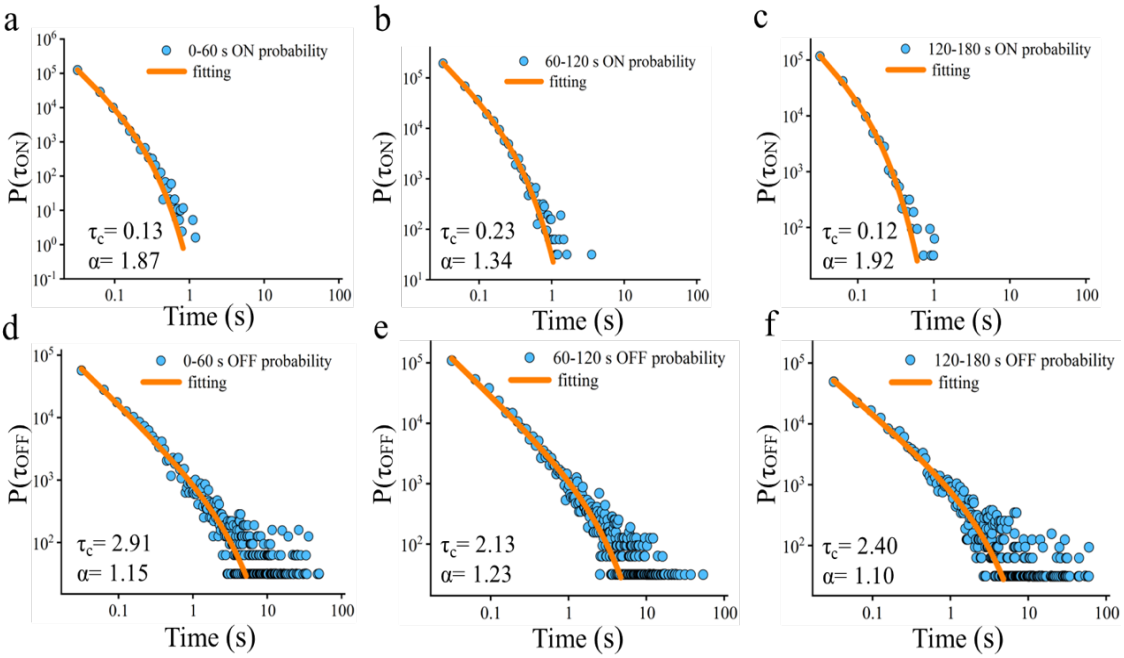

Figure 4.8. (a,b,c) ON and (d,e,f) OFF probability distributions for EL blinking (b,e) with and (a,c,d,f) without light-soaking.

4.2.3 The mechanism of charge carrier recombination

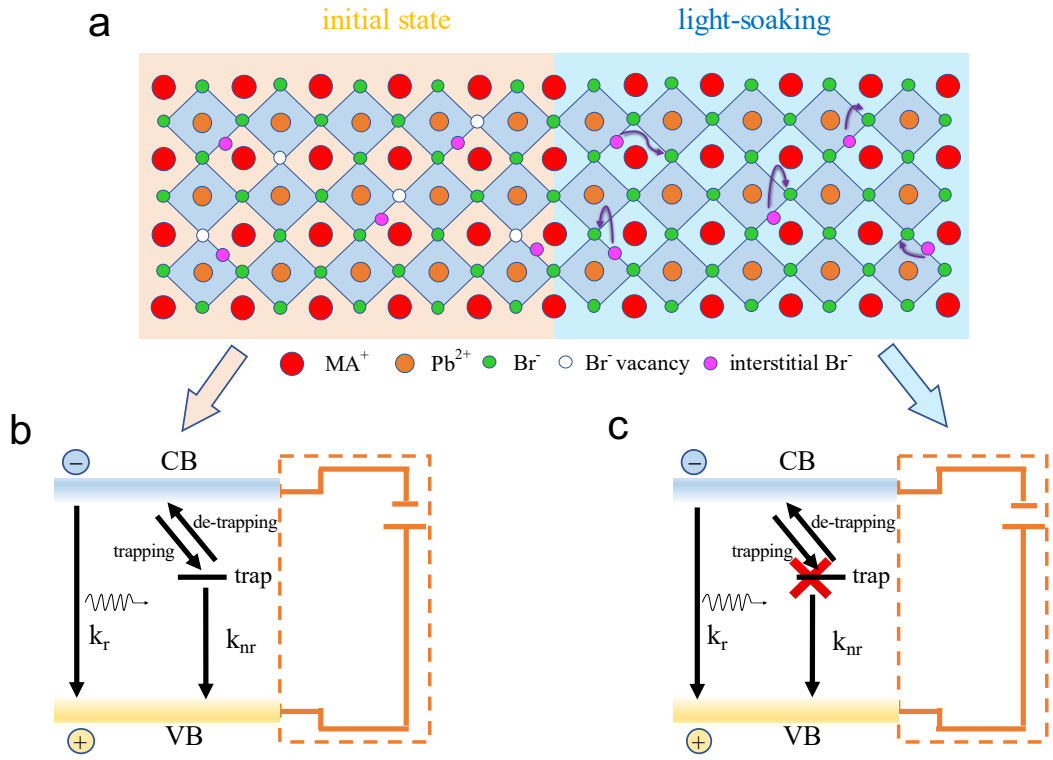

Figure 4.9. (a) The scheme of light-induced halide ion migration with and without light-soaking. (b) The scheme of charge carrier recombination and trapping-de-trapping-assisted nonradiative recombination under an electrical bias, without light-soaking. (c) The scheme of charge carrier recombination and trapping-de-trapping nonradiative recombination suppression under light illumination.

Without light illumination, the injected electrons and holes recombine radiatively or nonradiatively. Localized and mobile trap states assist the nonradiative recombination. The trap-assisted nonradiative recombination contributed to EL blinking. However, under light-soaking, the migration of bromide ions from the interstitial position to the vacancies (Figure 4.9) increases ion mobility, decreasing the probability of continuous nonradiative recombination in localized traps. In other words, under light illumination, the trap-assisted nonradiative recombination is suppressed,[54,56] decreasing the OFF time and increasing the ON time.

4.3 Conclusions

This chapter demonstrates the light-soaking effect on PL decay and EL blinking of $MAPbBr_3$ single microcrystals. I prepared micron-sized $MAPbBr_3$ single crystals at room temperature using a doctor-blading method, which are used for fabricating an LED device. The PL lifetime is increased by irradiating the crystal with a low-intensity 405 nm LED, which increases ion mobility in the crystals. The EL device shows continuous green emission with blinking at different applied voltages. The EL blinking ON and OFF probability distribution plots were analyzed from more than 100 single crystals before, during, and after light-soaking. The results show that the ON probability and ON time are increased, and the OFF probability and OFF time are decreased by light-soaking. When the weak excitation light above the bandgap energy for ion mobility increasing was turned off, the crystals showed increased blinking or an increase in the OFF probability and a decrease in the ON probability. Overall, the light-soaking experiments and results showed increased PL lifetime and suppressed EL blinking.

References

1. Roh, K.; Zhao, L.; Rand, B. P. Tuning Laser Threshold within the Large Optical Gain Bandwidth of Halide Perovskite Thin Films. *ACS Photon.* **2021**, *8*, 2548–2554.

2. Li, Y. F.; Feng, J.; Sun, H. B. Perovskite Quantum Dots for Light-Emitting Devices. *Nanoscale* **2019**, *11*, 19119–19139.

3. Xie, M.; Zhu, Y.; Wang, R.; Tian, J. High Efficiency and Narrow Emission Band Pure-Red Perovskite Colloidal Quantum Wells. *J. Phys. Chem. Lett*. **2021**, *12*, 10735–10741.

4. Jiang, J.; Chu, Z.; Yin, Z.; Li, J.; Yang, Y.; Chen, J.; Wu, J.; You, J.; Zhang, X. Red Perovskite Light-Emitting Diodes with Efficiency Exceeding 25% Realized by Co-Spacer Cations. *Adv. Mater.* **2022,** *34*, 2204460.

5. Mei, S.; Liu, X.; Zhang, W.; Liu, R.; Zheng, L.; Guo, R.; Tian, P. High-Bandwidth White-Light System Combining a Micro-LED with Perovskite Quantum Dots for Visible Light Communication. *ACS Appl. Mater. Interfaces* **2018**, *10*, 5641–5648.

6. Sun, G.; Liu, X.; Liu, Z.; Liu, D.; Meng, F.; Li, Z.; Chu, L.; Qiu, W.; Peng, X.; Xie, W.; Shen, C.; Chen, J.; Yip, H.; Su, S. Emission Wavelength Tuning via Competing Lattice Expansion and Octahedral Tilting for Efficient Red Perovskite Light-Emitting Diodes. *Adv. Funct. Mater.* **2021**, *31*, 2106691.

7. Wang, J.; Xiao, S.; Qian, W.; Zhang, K.; Yu, J.; Xu, X.; Wang, G.; Zheng, S.; Yang, S. Self-Driven Perovskite Narrowband Photodetectors with Tunable Spectral Responses. *Adv. Mater.* **2021**, *33*, 2005557.

8. Chen, L. J.; Dai, J. H.; Lin, J. D.; Mo, T. S.; Lin, H. P.; Yeh, H. C.; Chuang, Y. C.; Jiang, S. A.; Lee, C. R. Wavelength-Tunable and Highly Stable Perovskite-Quantum-Dot-Doped Lasers with Liquid Crystal Lasing Cavities. *ACS Appl. Mater. Interfaces* **2018**, *10*, 33307–33315.

9. Xing, G.; Mathews, N.; Lim, S. S.; Yantara, N.; Liu, X.; Sabba, D.; Grätzel, M.; Mhaisalkar, S.; Sum, T. C. Low-Temperature Solution-Processed Wavelength-Tunable Perovskites for Lasing. *Nat. Mater.* **2014**, *13*, 476–480.

10. Zhu, Z. Y.; Yang, Q. Q.; Gao, L. F.; Zhang, L.; Shi, A. Y.; Sun, C. L.; Wang, Q.; Zhang, H. L. Solvent-Free Mechanosynthesis of Composition-Tunable Cesium Lead Halide Perovskite Quantum Dots. *J. Phys. Chem. Lett*. **2017**, *8*, 1610–1614.

11. Wang, H.; Wei, H.; Zeng, X.; Zhou, J.; Zhu, Y. Conductive Path Mechanism for Bipolar Resistive Switching Characteristics in Lead-Free Perovskite $CsSnBr_3$-Based Nonvolatile Memories. *Phys. Status Solidi* **2021**, *218*, 2100501.

12. Lee, S.; Wolfe, S.; Torres, J.; Yun, M.; Lee, J. K. Asymmetric Bipolar Resistive Switching of Halide Perovskite Film in Contact with TiO_2 Layer. *ACS Appl. Mater. Interfaces* **2021**, *13*, 27209–27216.

13. Das, U.; Nyayban, A.; Paul, B.; Barman, A.; Sarkar, P.; Roy, A. Compliance Current-Dependent Dual-Functional Bipolar and Threshold Resistive Switching in All-Inorganic Rubidium Lead-Bromide Perovskite-Based Flexible Device. *ACS Appl. Electron. Mater*. **2020**, *2*, 1343–1351.

14. Shin, H.; Ryu, W.; Park, M.; Jung, K.; Kim, H.; Lee, J. Multilayered, Bipolar, All-Solid-State Battery Enabled by a Perovskite-Based Biphasic Solid Electrolyte. *ChemSusChem* **2018**, *11*, 3184–3190.

15. Rong, Y.; Hu, Y.; Mei, A.; Tan, H.; Saidaminov, M. I.; Seok, S. I.; McGehee, M. D.; Sargent, E. H.; Han, H. Challenges for Commercializing Perovskite Solar Cells. *Science* **2018**, *361*, eaat8235.

16. Jung, H. S.; Park, N. Perovskite Solar Cells: From Materials to Devices. *Small* **2015**, *11*, 10–25.

17. Kim, J. Y.; Lee, J. W.; Jung, H. S.; Shin, H.; Park, N. G. High-Efficiency Perovskite

Solar Cells. *Chem. Rev*. **2020**, *120*, 7867–7918.

18. Park, N. G. Perovskite Solar Cells: An Emerging Photovoltaic Technology. *Mater. Today* **2015**, *18*, 65–72.

19. Yuan, M.; Quan, L. N.; Comin, R.; Walters, G.; Sabatini, R.; Voznyy, O.; Hoogland, S.; Zhao, Y.; Beauregard, E. M.; Kanjanaboos, P.; Lu, Z.; Kim, D. H.; Sargent, E. H. Perovskite Energy Funnels for Efficient Light-Emitting Diodes. *Nat. Nanotech.* **2016**, *11*, 872–877.

20. Zou, W.; Li, R.; Zhang, S.; Liu, Y.; Wang, N.; Cao, Y.; Miao, Y.; Xu, M.; Guo, Q.; Di, D.; Zhang, L.; Yi, C.; Gao, F.; Friend, R. H.; Wang, J.; Huang, W. Minimising Efficiency Roll-off in High-Brightness Perovskite Light-Emitting Diodes. *Nat. Commun.* **2018**, *9*, 608.

21. Zhang, L.; Yang, X.; Jiang, Q.; Wang, P.; Yin, Z.; Zhang, X.; Tan, H.; Yang, Y.; Wei, M.; Sutherland, B. R.; Sargent, E. H.; You, J. Ultra-Bright and Highly Efficient Inorganic Based Perovskite Light-Emitting Diodes. *Nat. Commun.* **2017**, *8*, 15640.

22. Tian, Y.; Zhou, C.; Worku, M.; Wang, X.; Ling, Y.; Gao, H.; Zhou, Y.; Miao, Y.; Guan, J.; Ma, B. Highly Efficient Spectrally Stable Red Perovskite Light-Emitting Diodes. *Adv. Mater.* **2018**, *30*, 1707093.

23. Wang, F.; Zou, X.; Xu, M.; Wang, H.; Wang, H.; Guo, H.; Guo, J.; Wang, P.; Peng, M.; Wang, Z.; Wang, Y.; Miao, J.; Chen, F.; Wang, J.; Chen, X.; Pan, A.; Shan, C.; Liao, L.; Hu, W. Recent Progress on Electrical and Optical Manipulations of Perovskite Photodetectors. *Adv. Sci.* **2021**, *8*, 2100569.

24. Tian, W.; Zhou, H.; Li, L. Hybrid Organic–Inorganic Perovskite Photodetectors. *Small* **2017**, *13,* 1702107.

25. Jing, H.; Peng, R.; Ma, R. M.; He, J.; Zhou, Y.; Yang, Z.; Li, C. Y.; Liu, Y.; Guo,

X.; Zhu, Y.; Wang, D.; Su, J.; Sun, C.; Bao, W.; Wang, M. Flexible Ultrathin Single-Crystalline Perovskite Photodetector. *Nano Lett*. **2020**, *20*, 7144–7151.

26. Saidaminov, M. I.; Adinolfi, V.; Comin, R.; Abdelhady, A. L.; Peng, W.; Dursun, I.; Yuan, M.; Hoogland, S.; Sargent, E. H.; Bakr, O. M. Planar-Integrated Single-Crystalline Perovskite Photodetectors. *Nat. Commun.* **2015**, *6*, 8724.

27. Zhang, Q.; Su, R.; Du, W.; Liu, X.; Zhao, L.; Ha, S. T.; Xiong, Q. Advances in Small Perovskite-Based Lasers. *Small Methods* **2017**, *1*, 1700163.

28. Shang, Q.; Li, M.; Zhao, L.; Chen, D.; Zhang, S.; Chen, S.; Gao, P.; Shen, C.; Xing, J.; Xing, G.; Shen, B.; Liu, X.; Zhang, Q. Role of the Exciton–Polariton in a Continuous-Wave Optically Pumped $CsPbBr_3$ Perovskite Laser. *Nano Lett*. **2020,** *20*, 6636–6643.

29. Li, Z.; Moon, J.; Gharajeh, A.; Haroldson, R.; Hawkins, R.; Hu, W.; Zakhidov, A.; Gu, Q. Room-Temperature Continuous-Wave Operation of Organometal Halide Perovskite Lasers. *ACS Nano* **2018**, *12*, 10968–10976.

30. Chen, J.; Du, W.; Shi, J.; Li, M.; Wang, Y.; Zhang, Q.; Liu, X. Perovskite Quantum Dot Lasers. *InfoMat.* **2020**, *2*, 170–183.

31. Lin, K.; Xing, J.; Quan, L. N.; De Arquer, F. P. G.; Gong, X.; Lu, J.; Xie, L.; Zhao, W.; Zhang, D.; Yan, C.; Li, W.; Liu, X.; Lu, Y.; Kirman, J.; Sargent, E. H.; Xiong, Q.; Wei, Z. Perovskite Light-Emitting Diodes with External Quantum Efficiency Exceeding 20 percent. *Nature* **2018**, *562*, 245–248.

32. Conings, B.; Drijkoningen, J.; Gauquelin, N.; Babayigit, A.; D'Haen, J.; D'Olieslaeger, L.; Ethirajan, A.; Verbeeck, J.; Manca, J.; Mosconi, E.; Angelis, F. D.; Boyen, H. Intrinsic Thermal Instability of Methylammonium Lead Trihalide Perovskite. *Adv. Energy Mater.* **2015**, *5*, 1500477.

33. Straus, D. B.; Guo, S.; Abeykoon, A. M.; Cava, R. J. Understanding the Instability

of the Halide Perovskite $CsPbI_3$ through Temperature-Dependent Structural Analysis. *Adv. Mater.* **2020**, *32*, 2001069.

34. Schutt, K.; Nayak, P. K.; Ramadan, A. J.; Wenger, B.; Lin, Y.; Snaith, H. J. Overcoming Zinc Oxide Interface Instability with a Methylammonium-Free Perovskite for High-Performance Solar Cells. *Adv. Funct. Mater.* **2019**, *29*, 1900466.

35. Slavney, A. H.; Smaha, R. W.; Smith, I. C.; Jaffe, A.; Umeyama, D.; Karunadasa, H. I. Chemical Approaches to Addressing the Instability and Toxicity of Lead–Halide Perovskite Absorbers. *Inorg. Chem*. **2017**, *56*, 46–55.

36. Zou, W.; Li, R.; Zhang, S.; Liu, Y.; Wang, N.; Cao, Y.; Miao, Y.; Xu, M.; Guo, Q.; Di, D.; Zhang, L.; Yi, C.; Gao, F.; Friend, R. H.; Wang, J.; Huang, W. Minimising Efficiency Roll-off in High-Brightness Perovskite Light-Emitting Diodes. *Nat. Commun.* **2018**, *9*, 608.

37. Yang, M.; Wang, N.; Zhang, S.; Zou, W.; He, Y.; Wei, Y.; Xu, M.; Wang, J.; Huang, W. Reduced Efficiency Roll-Off and Enhanced Stability in Perovskite Light-Emitting Diodes with Multiple Quantum Wells. *J. Phys. Chem. Lett*. **2018**, *9*, 2038–2042.

38. Zhang, D.; Chao, L.; Jin, G.; Xing, Z.; Hong, W.; Chen, Y.; Wang, L.; Chen, J.; Ma, D. Highly Efficient Red Perovskite Light-Emitting Diodes with Reduced Efficiency Roll-Off Enabled by Manipulating Crystallization of Quasi-2D Perovskites. *Adv. Funct. Mater.* **2022**, *32*, 2205707.

39. Yuan, Y.; Huang, J. Ion Migration in Organometal Trihalide Perovskite and Its Impact on Photovoltaic Efficiency and Stability. *Acc. Chem. Res*. **2016**, *49*, 286–293.

40. Calado, P.; Telford, A. M.; Bryant, D.; Li, X.; Nelson, J.; O'Regan, B. C.; Barnes,

P. R. F. Evidence for Ion Migration in Hybrid Perovskite Solar Cells with Minimal Hysteresis. *Nat. Commun.* **2016**, *7*, 13831.

41. Adams, G. R.; Adhikari, N.; Parker, H.; Okoli, O. Flexible Wire-Shaped Perovskite Photodetector via Joule Heating for Improved Crystallization and Performance. *Adv. Mater. Interfaces* **2018**, *5*, 1800082.

42. Salado, M.; Contreras-Bernal, L.; Caliò, L.; Todinova, A.; López-Santos, C.; Ahmad, S.; Borras, A.; Idígoras, J.; Anta, J. A. Impact of Moisture on Efficiency-Determining Electronic Processes in Perovskite Solar Cells. *J. Mater. Chem. A* **2017**, *5*, 10917–10927.

43. Xie, M.; Tian, J. Operational Stability Issues and Challenges in Metal Halide Perovskite Light-Emitting Diodes. *J. Phys. Chem. Lett*. **2022,** *13*, 1962–1971.

44. Liu, C.; Fan, J.; Zhang, X.; Shen, Y.; Yang, L.; Mai, Y. Hysteretic Behavior upon Light Soaking in Perovskite Solar Cells Prepared via Modified Vapor-Assisted Solution Process. *ACS Appl. Mater. Interfaces* **2015**, *7*, 9066–9071.

45. Leijtens, T.; Eperon, G. E.; Pathak, S.; Abate, A.; Lee, M. M.; Snaith, H. J. Overcoming Ultraviolet Light Instability of Sensitized TiO_2 with Meso-Superstructured Organometal Tri-Halide Perovskite Solar Cells. *Nat. Commun.* **2013**, *4*, 2885.

46. Eames, C.; Frost, J. M.; Barnes, P. R. F.; O'Regan, B. C.; Walsh, A.; Islam, M. S. Ionic Transport in Hybrid Lead Iodide Perovskite Solar Cells. *Nat. Commun.* **2015**, *6*, 7497.

47. Meloni, S.; Moehl, T.; Tress, W.; Franckevičius, M.; Saliba, M.; Lee, Y. H.; Gao, P.; Nazeeruddin, M. K.; Zakeeruddin, S. M.; Rothlisberger, U.; Graetzel, M. Ionic Polarization-Induced Current–Voltage Hysteresis in $CH_3NH_3PbX_3$ Perovskite Solar Cells. *Nat. Commun.* **2016**, *7*, 10334.

48. Bastos, J. P.; Paetzold, U. W.; Gehlhaar, R.; Qiu, W.; Cheyns, D.; Surana, S.; Spampinato, V.; Aernouts, T.; Poortmans, J. Light-Induced Degradation of Perovskite Solar Cells: The Influence of 4-Tert-Butyl Pyridine and Gold. *Adv. Energy Mater.* **2018**, *8*, 1800554.

49. Zhao, C.; Chen, B.; Qiao, X.; Luan, L.; Lu, K.; Hu, B. Revealing Underlying Processes Involved in Light Soaking Effects and Hysteresis Phenomena in Perovskite Solar Cells. *Adv. Energy Mater.* **2015**, *5*, 1500279.

50. Domanski, K.; Roose, B.; Matsui, T.; Saliba, M.; Turren-Cruz, S.-H.; Correa-Baena, J.-P.; Carmona, C. R.; Richardson, G.; Foster, J. M.; De Angelis, F.; Ball, J. M.; Petrozza, A.; Mine, N.; Nazeeruddin, M. K.; Tress, W.; Grätzel, M.; Steiner, U.; Hagfeldt, A.; Abate, A. Migration of Cations Induces Reversible Performance Losses over Day/Night Cycling in Perovskite Solar Cells. *Energy Environ. Sci*. **2017**, *10*, 604–613.

51. Wu, X.; Wang, J.; Yeow, E. K. L. Ultralong Perovskite Microrods: One- versus Two-Step Synthesis and Enhancement of Hole-Transfer During Light Soaking. *J. Phys. Chem. C* **2016**, *120*, 12273–12283.

52. Chen, S.; Wen, X.; Huang, S.; Huang, F.; Cheng, Y.; Green, M.; Ho-Baillie, A. Light Illumination Induced Photoluminescence Enhancement and Quenching in Lead Halide Perovskite. *Solar RRL* **2017**, *1*, 1600001.

53. Liu, M.; Wan, Q.; Wang, H.; Carulli, F.; Sun, X.; Zheng, W.; Kong, L.; Zhang, Q.; Zhang, C.; Zhang, Q.; Brovelli, S.; Li, L. Suppression of Temperature Quenching in Perovskite Nanocrystals for Efficient and Thermally Stable Light-Emitting Diodes. *Nat. Photon.* **2021**, *15*, 379–385.

54. Ghosh, S.; Shi, Q.; Pradhan, B.; Mushtaq, A.; Acharya, S.; Karki, K. J.; Pullerits, T.; Pal, S. K. Light-Induced Defect Healing and Strong Many-Body Interactions in Formamidinium Lead Bromide Perovskite Nanocrystals. *J. Phys. Chem. Lett*. **2020**,

11, 1239–1246.

55. Li, J.; Yuan, X.; Jing, P.; Li, J.; Wei, M.; Hua, J.; Zhao, J.; Tian, L. Temperature-Dependent Photoluminescence of Inorganic Perovskite Nanocrystal Films. *RSC Adv*. **2016**, *6*, 78311–78316.

56. Ghosh, S.; Pal, S. K.; Karki, K. J.; Pullerits, T. Ion Migration Heals Trapping Centers in $CH_3NH_3PbBr_3$ Perovskite. *ACS Energy Lett*. **2017**, *2*, 2133–2139.

Chapter 5
Time-resolved electroluminescence of $MAPbBr_3$ microcrystals

Abstract

Perovskite LEDs have been widely investigated due to their cost-effective and straightforward fabrication in multiple colors. In this chapter, I introduce the time-resolved photoluminescence and electroluminescence of $MAPbBr_3$ perovskite single-crystal LEDs under the effect of halide vacancy filling. First, I show the electroluminescence spectra and lifetimes of commercial LEDs (blue, green, red) under 3-5.7 V. Next, I show the photoluminescence and electroluminescence spectra and decays of $MAPbBr_3$ microcrystals with or without halide vacancy filling using MABr. Increases in the photoluminescence and electroluminescence intensities and lifetimes of crystals treated with MABr suggest halide vacancy filling-induced suppression of nonradiative recombination. Although there have been several studies using steady-state and time-resolved fluorescence spectroscopy and steady-state electroluminescence spectroscopy on halide vacancy filling, the work in this chapter introduces time-resolved electroluminescence studies of halide vacancy filling in perovskites for the first time. Increases in the photoluminescence intensity, electroluminescence intensity, photoluminescence lifetime, and electroluminescence lifetime are all consistent with halide vacancy filling, which is expected to have important implications in the progress of perovskite LEDs and lasers.

5.1 Introduction

Halide perovskites have been regarded as the most promising next-generation optoelectronic materials owing to their excellent optoelectronic properties.[1-16] The comprehension of charge carrier recombination dynamic in halide perovskites is crucial for improving the optoelectronic properties and stability of halide perovskites devices. The photoexcited charge carrier recombination dynamic in halide perovskites has been widely investigated in the past decade. Mondal et al. utilized a combined femtosecond transient absorption (TA) spectroscopy and photoluminescence (PL) spectroscopy to study the transient states during charge carrier recombination in perovskite nanocrsytals.[17] Song et al. investigated the role of humidity on the charge carrier recombination dynamic of photoexcited perovskites and related it to the degradation of $MAPbBr_3$ and $MAPbI_3$ films under high humidity.[18] Meng et al. doped $CsPbCl_3$ perovskite QDs with manganese and found that the PL quantum yield (QY) can be increased by increasing the manganese concentration to a certain level, beyond which the PLQY decreased due to the formation of interstitial deep traps.[19] Dane et al. revealed that intergrain connectivity leads to charge carrier diffusion randomly in different directions in perovskite film.[20] Shajahan at al.,[21] Ghimre et al.,[22] and Okamoto et al.[23] demonstrated halide vacancy filling-induced increases in the PL lifetimes and PLQY of perovskite microcrystals and nanocrystals. The above studies studies and other reports suggested various doping methods to suppress nonradiative carrier losses in photoexcited or electrically biased halide perovskite solar cells or LEDs, one of which is halide vacancy filling. Although many steady-state and time-resolved PL studies have been conducted to understand the effects of dopants such as halide precursors on nonradiative losses, the time-resolved electroluminescence (EL) method has yet to be established.

Since 2014 Friend at al. first fabricated a perovskite LED thin film,[24] the halide perovskites based on EL devices have attracted much attention and are widely studied. With the attribution of perovskite LEDs' color purity,[25-29] tunable band,[30-34] and cost-

effectiveness,[35] halide perovskite LEDs emerge into a stage to replace the conventional LEDs. Chen et al. synthesized a low trap density perovskite single crystal by mixing cations, extra ammonium halides, and polyvidone additives. The as-synthesized single crystals showed a high PLQY (28.3%). Additionally, this report showed a long device lifetime.[25] Sun et al. obtained a near-infrared emitting perovskite LED, which also showed a high external QY.[36] Ren et at. prepared a stable and high efficiency red color emitting perovskite LED by doping the nanocrystal with KBr. The halide segregation in common mixed halide perovskites can be suppressed by doping.[37] Still perovskite LEDs (PeLEDs) are far from the commercial level due to limited performance efficiency and stability.

Time-resolved spectroscopy is a powerful method to study the ultrafast charge carrier behavior.[38-41] In perovskite, the charge carrier recombination processes are in the sub-microsecond scale.[42-43] Therefore, the time-resolved PL (TRPL) on perovskites has been widely investigated in recent years. Zhan et al., utilized the TRPL technique to indicate the interaction between DHA (1,3-dihydroxypropan-2-one) and perovskite. The addition of DHA improved the device's efficiency and stability.[44] Qiu et al. studied the correlation between carrier recombination dynamics and the structure of printable mesoscopic perovskite solar cells.[45] Bhagyalakshmi et al. applied MABr to $MAPbBr_3$ and studied the effect of halide vacancy filling on the steady-state EL of PeLEDs, demonstrating halide vacancy filling increases the EL intensity and suppresses EL blinking.[46] However, understanding the time-resolved carrier recombination processes by time-resolved EL (TREL) studies is essential for rationalizing nonradiative losses in PeLEDs.

In this chapter, I measured the EL spectra and decay of commercial LEDs (blue, green, red) as standard LED devices as reference samples. $MAPbBr_3$ single crystals were directly grown on ITO glasses using the doctor-blading method. Then, I sandwiched the crystals between two ITO glasses. The device structure is similar to those in Chapter 4. After that, I studied the TRPL and TREL of the single-crystal LEDs. In detail, I measured

the PL and EL spectra of $MAPbBr_3$ MCs to understand the optical properties, followed by recording the PL and EL decays. I used a picosecond laser combined with an optical microscope, a TCSPC module, a photon counter, a delay generator, an avalanche photodiode, a CCD camera, and a fiber-optical spectrometer in the TRPL studies. I replaced the picosecond laser in the TRPL studies with a function generator and an electrical pulse amplifier in the TREL studies. In TRPL studies, evaluation of the real-time effect of MABr on $MAPbBr_3$ has been possible,[23, 46] whereas due to the closed structure of PeLEDs, I followed the post-synthesis MABr treatment on $MAPbBr_3$ in TREL studies. I found increases in the EL lifetimes for MABr-treated samples, consistent with the PL and EL intensity and PL lifetime increases. Finally, the mechanism of the halide vacancy filling-induced EL lifetime increase is discussed.

5.2 Results and discussion

5.2.1 The scheme of instrument setting for TRPL and TREL measurements

The TRPL and TREL measurement instrument scheme is displayed in Figure 5.1. For the TRPL measurement, a 465 nm picosecond laser with 1 MHz power and 45 ps pulse width was used as the excitation source. For TREL measurements, the laser was replaced by a function generator (FG) with 40 ns pulse width and 200 kHz to 1 MHz repletion rate (green line part). The maximum voltage reached 5.7 V without the amplifier. Therefore, the FG alone (without the pulse amplifier) was used in the final measurements.

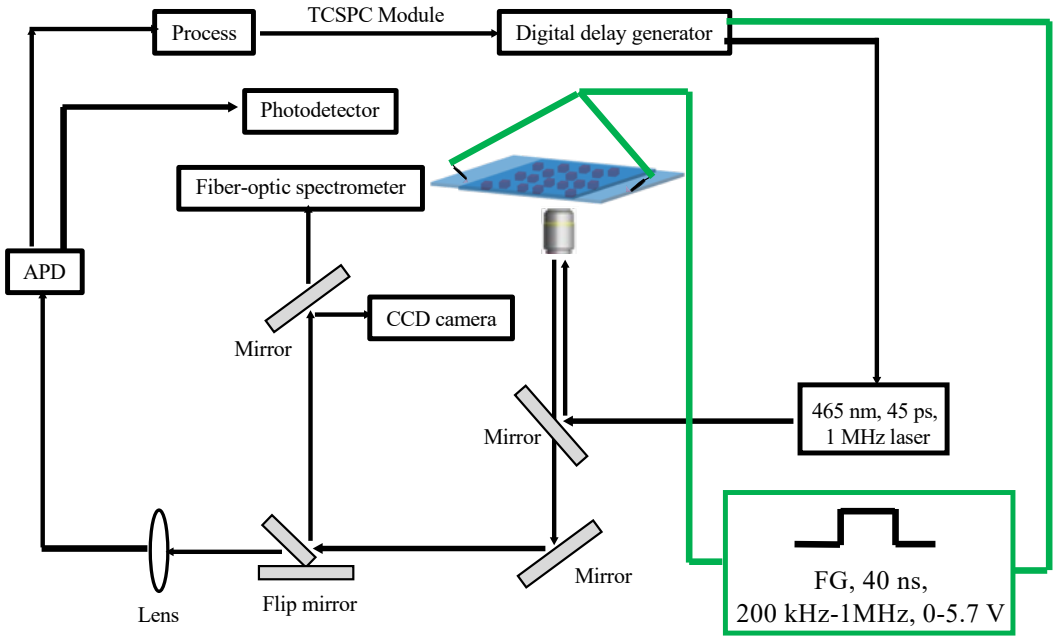

Figure 5.1. The scheme of the instrument setting for TRPL and TREL measurements.

5.2.2 Time-resolved electroluminescence of commercial LEDs

LEDs have been widely employed in many aspects of daily life, including room lighting, display screens, LCD panels, and indication lights. The three most prevalent hues of LEDs are blue, green, and red. GaN and AlInGaP are the primary materials used to make them. Figure 5.2 displays the EL spectra of three different commercial LEDs of different colors. The maximum peak positions of the blue, green, and red LEDs are at 483, 514, and 654 nm, respectively.

In TREL measurements, first, I measured the EL decays of the commercial LEDs as the references to test the instrument's reliability. Figure 5.3 shows the EL decay curves and lifetimes of blue, green, and red LEDs. The green LED has the longest EL lifetime, which is 15 ns. The blue LED showed the shortest EL lifetime (4 ns). The red LED (6 ns) showed an intermediate lifetime value. These values are the intrinsic properties of the devices, which are unknown due to the commercia nature of the devices.

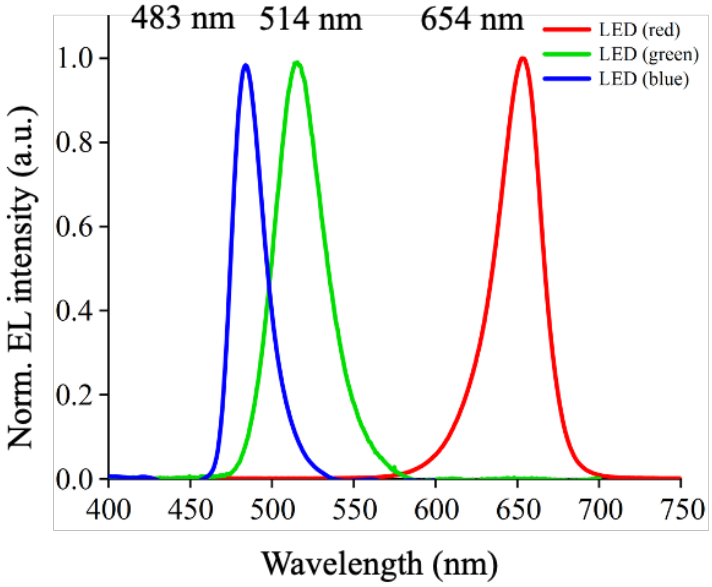

Figure 5.2. The EL spectra of commercial red, green, and blue LEDs under 5.7 V pulsed exciation.

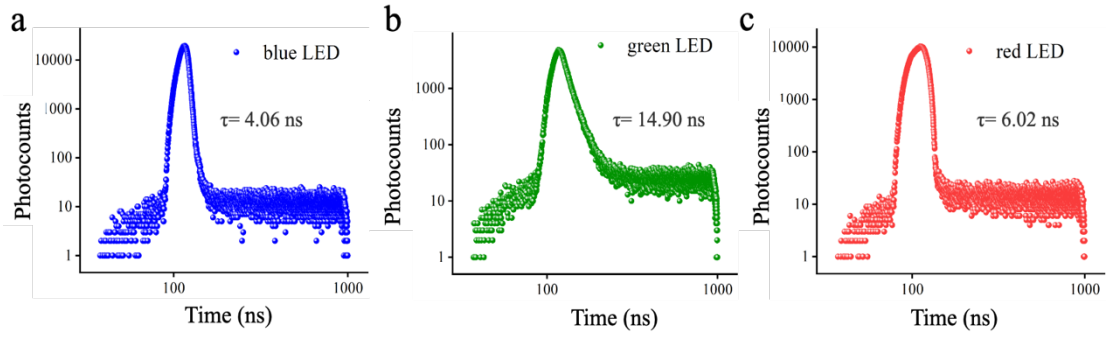

Figure 5.3. EL decays of commercial (a) blue, (b) green, and (c) red LEDs under 5.7 V pulsed excitation.

5.2.3 Preparation of $MAPbBr_3$ halide perovskite microcrystals

The $MAPbBr_3$ MCs were prepared by the doctor-blading method at room temperature. In detail, the 0.5 M $MAPbBr_3$ precursor solution was prepared by mixing equal volumes of 1M MABr and 1 $MPbBr_2$ solutions. Then, the equal volume of the as-synthesized $MAPbBr_3$ precursor solution was mixed with an equal volume of GBL. This solution was labeled as $MAPbBr_3$-GBL precursor solution. After that, I cleaned an ITO glass with

deoxidized water and acetone. 20 μL $MAPbBr_3$-GBL precursor solution was dropped on the ITO-coated side of the glass plate. Another clean ITO glass plate was used to blade the precursor to ensure the precursor fully covered the ITO surface, and there was no bubble in the precursor. The two ITOs with a thin solution film were placed at room temperature for crystallization. A duration of 30 minutes was needed for the crystallization process. The EL device was finished by clipping the two ITO plates using metal clips with $MAPbBr_3$ crystals sandwiched between the ITO plates and attaching copper wires to the ITO-coated sides.

5.2.4 Characterization of $MAPbBr_3$ microcrystals

After synthesizing $MAPbBr_3$ MCs, I studied the morphology and optical properties of the as-synthesized $MAPbBr_3$ crystals in the device. An optical transmission image of the crystals in a device is shown in Figure 5.4a. The crystals were cuboids with 5-30 μm edge lengths. Figure 5.4b shows the EL image of the crystals under a 5 V power supply. The crystals showed bright green emission. The PL and EL spectra of $MAPbBr_3$ MCs are displayed in Figure 5.4c. The PL spectra was collected by exciting crystals with a 465 nm laser, and EL spectra were collected by applying 5 V. The spectra with the PL maximum at 549 nm and the EL maximum at 555 nm are selected here. The slightly redshifted (6 nm) EL peak is attributed to the reabsorption-emission for the emitting center vertically displaced away from the bottom surface of the crystal. In the case of the PL spectrum, the laser excited the sample from the bottom, and spectra was also collected from the bottom, minimizing reabsorption-mission-induced spectral redshift.

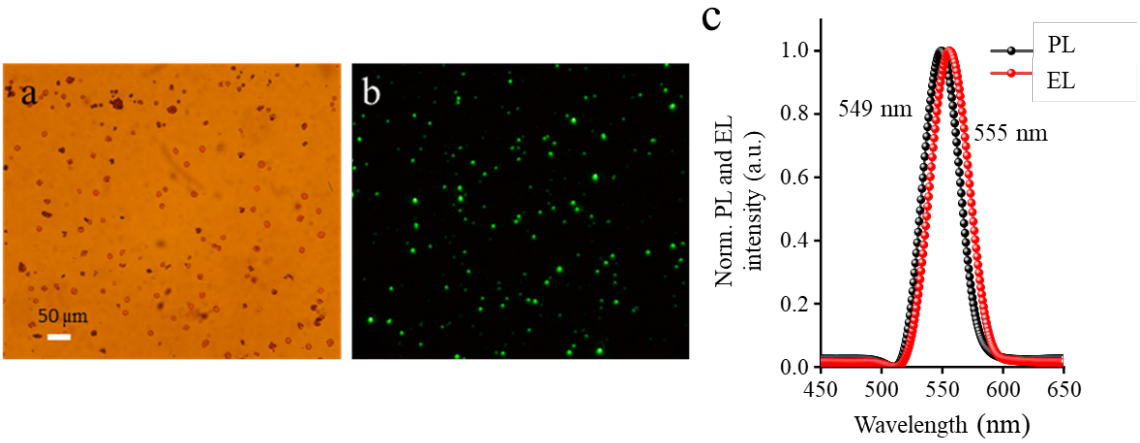

Figure 5.4. (a) An optical transmission image and (b) an EL image of $MAPbBr_3$ MCs in an LED under 5 V. (c) The PL and EL spectra of a $MAPbBr_3$ MC.

5.2.5 Real-time and post-synthesis treatments on $MAPbBr_3$ microcrystals

Halide perovskites have a low formation energy. During the solution processing for halide perovskite crystallization, defects are usually formed as intrinsic and extrinsic defects, such as vacancies and interstitials. Also, impurities and noncoordinated ions can be present at crystal surfaces and grain boundaries.[47, 49-51] There have been various methods to heal these defects. The pre-synthesis method is an effective way to obtain high-quality crystals, like the controlled crystallization speed, closed synthesis environment, and proper precursor concentrations can help with this. Real-time ion passivation is another good way to reduce defects, which helps focus on the defects of the same crystal and observe how the defect density changes within a short time. Real-time treatment method applies to only open samples. Another method is the post-synthesis treatment, which is usually done after crystallization. In this chapter, I performed the real-time and post-synthesis bromide ion treatment methods to reduce the defects in $MAPbBr_3$ MCs, and I recorded how the PL and EL spectra and decays change with Br vacancy filling.

The MABr solution for the real-time and post-treatment of $MAPbBr_3$ MCs was prepared in two ways. For the post-synthsis treatment, I prepare a saturated MABr

solution in isopropanol. It was then mixed (100 µL) with 250 mL toluene. For the real-time treatment, I prepared a saturated MABr solution in isopropanol, then mixed 100 µL this solution with 900 µL 1-hexadecene. The resulting solution was used as the MABr solution for the real-time treatment of $MAPbBr_3$ MCs.

The PL spectra of $MAPbBr_3$ MCs showed a narrow emission peak. To study how the MABr solution affects the PL spectra, I performed the real-time treatment on $MAPbBr_3$ MCs. The as-synthesized $MAPbBr_3$ MCs were placed in the microscope stage, and the PL spectra were recorded from a single isolated crystal by controlling the iris. After that, I dropped 10 µL $MAPbBr_3$ solution on the same single crystal. Then, the PL spectrum was recorded from the same crystal. The result is shown in Figure 5.5a; the PL intensities of treated crystals increased compared with untreated ones. This is because the bromide ions from the MABr solution fill the bromide vacancies. The trap filling enhanced the PL intensity.

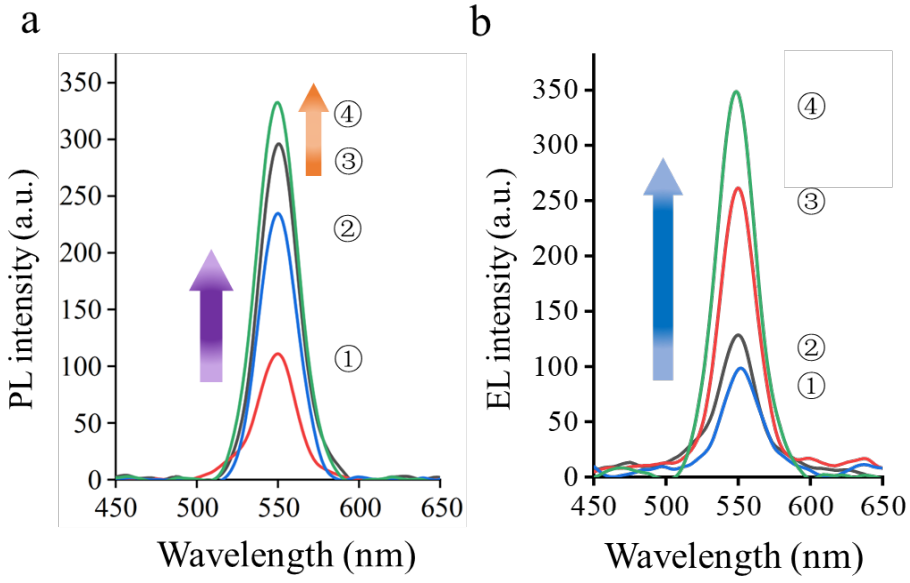

Figure 5.5. (a) The PL spectra of two $MAPbBr_3$ MCs irradiated by a 460 nm laser. ① and ③ are the PL spectra from two untreated crystals, and ② and ④ are the real-time treated PL spectra from the same two crystals. (b) The EL spectra of two $MAPbBr_3$ MCs under 5.7 V. ① and ② are the EL spectra from two untreated crystals, and ③ and ④ are the EL spectra from two different post-treated crystals.

The MABr solution treatment effect on the EL spectra was performed by the post-treatment method because the EL spectra were collected from the LED device under 5.7 V, which is a closed system. In other words, it wasn't easy to introduce an MABr solution to an LED device and perform real-time spectral measurements. Therefore, EL spectra were recorded from different crystals, without or with MABr treatment. I measured the EL spectra from several crystals and confirmed the EL intensity increase for post-synthesis MABr-treated crystals. Figure 5.5b shows four EL spectra for as-synthesized (① and ②) and MABr (③ and ④) crystals.

The PL decay profiles were recorded by exciting $MAPbBr_3$ MCs with a 465 nm picosecond laser to understand the PL lifetime changes under MABr treatment and vacancy filling. The PL decay shows multiexponential kinetics, and the average PL lifetime was calculated by fitting the decays to the third exponential equation. The above real-time MABr-treatment method was carried out to study the effect of MABr solution on PL decays. In the beginning, PL decays were recorded from single crystals, and a 10 µL MABr solution was added to the same crystals and recorded the decays again. Figure

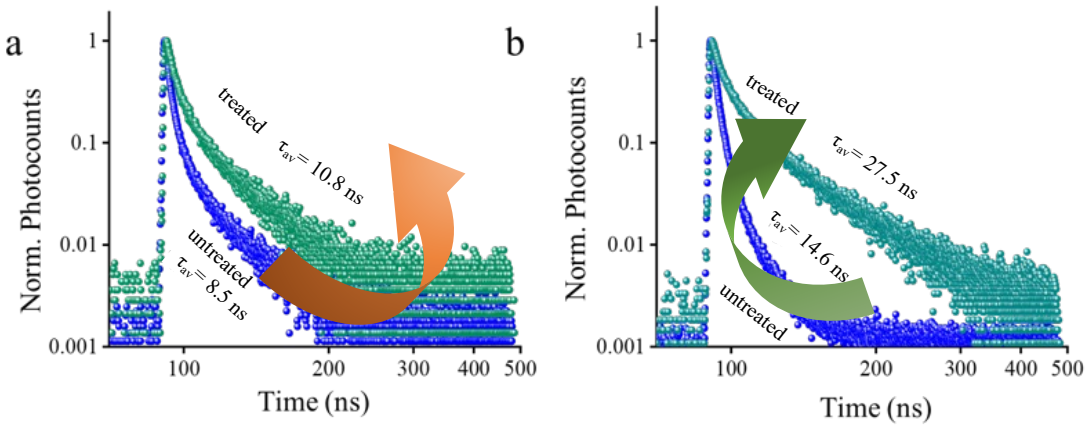

Figure 5.6. The PL decays of two $MAPbBr_3$ MCs untreated (a) and real-time treated (b) with an MABr solution.

5.6 shows the PL decays and lifetimes of untreated and real-time treated from two crystals. The PL lifetimes are increased from 8.5 to 10.8 ns, and 14.6 to 27.5 ns for the two crystals.

This is due to trap-assisted nonradiative recombination suppression by the bromide vacancy filling with MABr.

Next, I studied the EL lifetime change for $MAPbBr_3$ MCs under post-synthesis treatment, as discussed in the EL spectral measurement method above. Typical EL decays of untreated and MABr-treated crystals at 5.7 V are shown in Figure 5.7. The EL lifetime is 52.7 ns for an untreated crystals, which is 135.6 ns for an MABr-treated one. Several such EL decays were collected from single crystals of untreated and MABr-treated samples to obtain a trend in the EL lifetime values. EL lifetimes are always longer than PL lifetimes, which is attributed to the differences in the carrier injection-recombination processes in EL and band-to-band photoexcitation relaxation in PL. The average EL and PL lifetimes with standard derivations are plotted in Figure 5.8. The average PL lifetime increased from 6.3 to 12.0 ns, whereas the average EL lifetime increased from 32.1 to 67.3 ns. The overall increases in the EL and PL lifetimes and intensities suggest Br vacancy filling and increased radiative recombination in $MAPbBr_3$ crystals.[52-53]

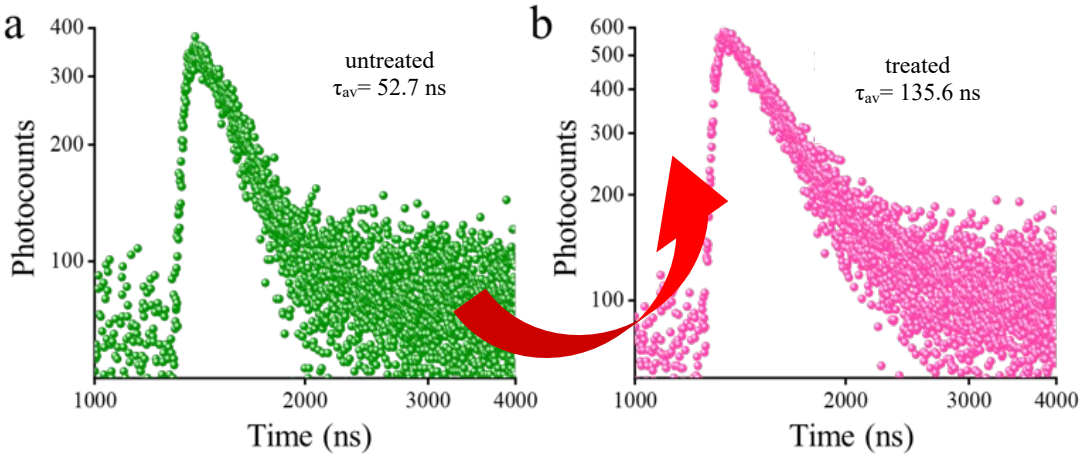

Figure 5.7. The EL decays of two $MAPbBr_3$ MCs (a) untreated and (b) post-treated by MABr solution.

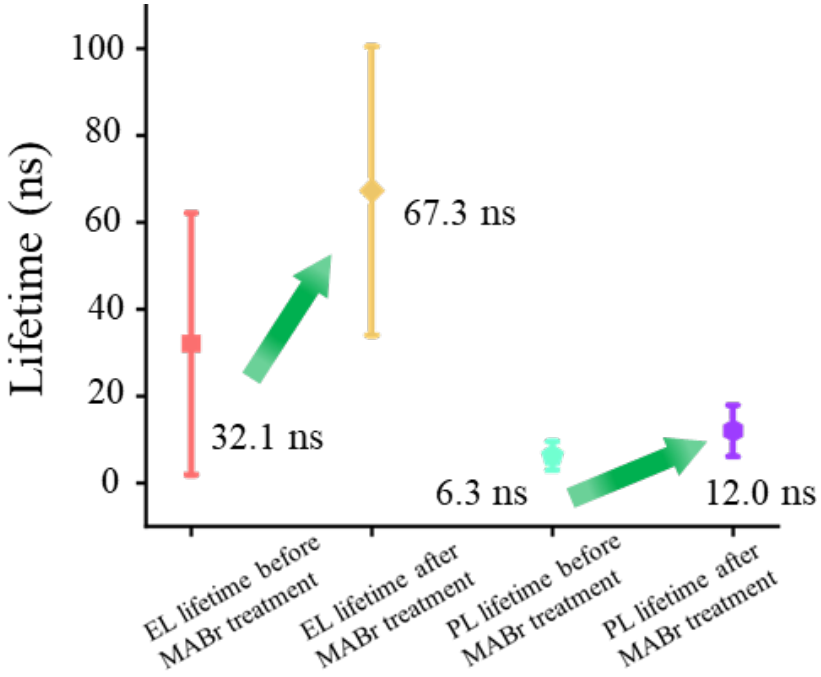

Figure 5.8. The average EL and PL calculated from 10 crystals. The vertical lines show stand deviation.

5.2.6 The mechanism of MABr induced Br vacancy filling in microcrystals

The bromide vacancies in $MAPbBr_3$ MCs formed during the crystallization process act as the shallow traps in the band gap. The trap-assisted nonradiative carrier recombination *via* the trapping-detrapping cycle lowers the PL and EL QYs. The bromide vacancies were filled in both cases of real-time and post-synthesis treatment by MABr solution for both photo-excited and electronic-excited charge carrier recombination process as shown in Figure 5.9. As a result, nonradiative carrier recombination is suppressed. Therefore, the PL and EL intensity and lifetime were increased.

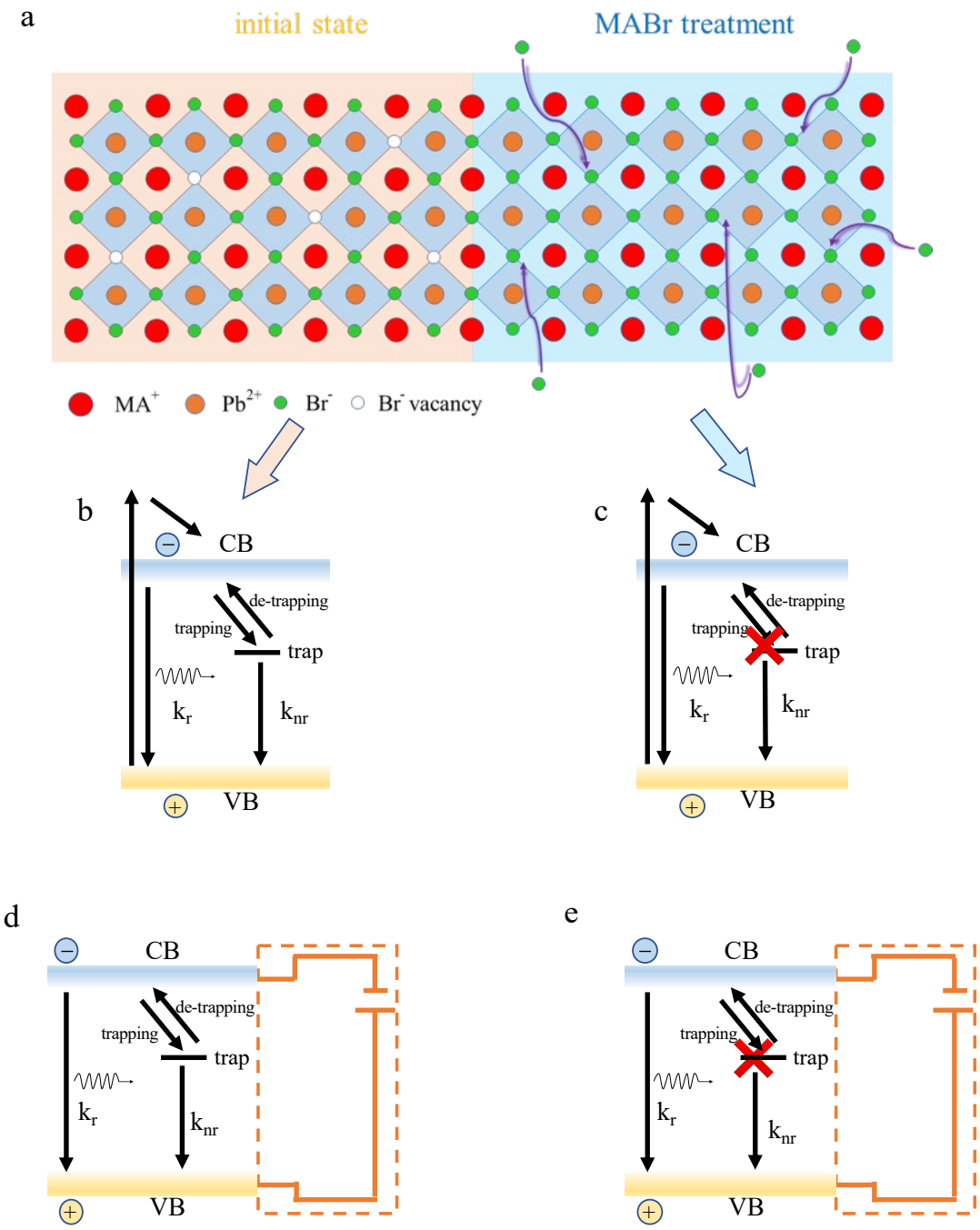

Figure 5.9. (a) The scheme of bromide vacancy filling by bromide ions from MABr solution. (b) (c) The trap-assisted nonradiative recombination is suppressed by the bromide ions for the PL lifetime measurement. (d) (e) The trap-assisted nonradiative recombination is suppressed by the bromide ions for the EL lifetime measurement.

5.3 Conclusions

In this chapter, I studied the photoluminescence and electroluminescence properties of three commercial LEDs (blue, green, blue). The electroluminescence spectra and decays recorded for the different colored LEDs helped to standardize certain experimental conditions. After that, I studied the morphology, photoluminescence, and electroluminescence properties of the as-synthesized $MAPbBr_3$ microcrystal, which were synthesized by the blade-coating method at room temperature. The samples showed micron-size cubic crystals with intense green PL and EL. Then, I studied the MABr treatment effect on the PL and EL spectra and lifetimes of $MAPbBr_3$ MCs by real-time and post-synthesis treatment methods. The photoluminescence and electroluminescence intensities were increased after the treatment. For the PL and EL decay studies, real-time and post-synthesis MABr treatments were performed. The PL and EL lifetimes increased after the MABr treatments, confirming vacancies in untreated or as-synthesized crystals and Br vacancy filling-induced nonradiative carrier recombination suppression in treated crystals.

References

1. Liang, H.; Yuan, F.; Johnston, A.; Gao, C.; Choubisa, H.; Gao, Y.; Wang, Y.; Sagar, L. K.; Sun, B.; Li, P.; Bappi, G.; Chen, B.; Li, J.; Wang, Y.; Dong, Y.; Ma, D.; Gao, Y.; Liu, Y.; Yuan, M.; Saidaminov, M. I.; Hoogland, S.; Lu, Z.; Sargent, E. H. High Color Purity Lead-Free Perovskite Ligh-Emitting Diodes via Sn Stabilization. *Adv. Sci.* **2020**, *7*, 1903213.
2. Fu, Y.; Zhu, H.; Chen, J.; Hautzinger, M. P.; Zhu, X.-Y.; Jin, S. Metal Halide Perovskite Nanostructures for Optoelectronic Applications and the Study of Physical Properties. *Nat. Rev. Mater.* **2019**, *4*, 169–188.
3. Docampo, P.; Bein, T. A Long-Term View on Perovskite Optoelectronics. Acc. *Chem. Res*. **2016**, *49*, 339–346.
4. Wenger, B.; Nayak, P. K.; Wen, X.; Kesava, S. V.; Noel, N. K.; Snaith, H. J. Consolidation of the Optoelectronic Properties of $CH_3NH_3PbBr_3$ Perovskite Single Crystals. *Nat. Commun.* **2017**, *8*, 590.
5. Liu, J.; Xue, Y.; Wang, Z.; Xu, Z. Q.; Zheng, C.; Weber, B.; Song, J.; Wang, Y.; Lu, Y.; Zhang, Y.; Bao, Q. Two-Dimensional $CH_3NH_3PbI_3$ Perovskite: Synthesis and Optoelectronic Application. *ACS Nano* **2016**, *10*, 3536–3542.
6. Kovalenko, M. V.; Protesescu, L.; Bodnarchuk, M. I. Properties and Potential Optoelectronic Applications of Lead Halide Perovskite Nanocrystals. *Science* **2017**, *358*, 745–750.
7. Chen, Q.; Zhou, H.; Fang, Y.; Stieg, A. Z.; Song, T. B.; Wang, H. H.; Xu, X.; Liu, Y.; Lu, S.; You, J.; Sun, P.; McKay, J.; Goorsky, M. S.; Yang, Y. The Optoelectronic Role of Chlorine in $CH_3NH_3PbI_3$(Cl)-Based Perovskite Solar Cells. *Nat. Commun*. **2015**, *6*, 7269.

8. Khadka, D. B.; Shirai, Y.; Yanagida, M.; Ryan, J. W.; Miyano, K. Exploring the Effects of Interfacial Carrier Transport Layers on Device Performance and Optoelectronic Properties of Planar Perovskite Solar Cells. J. *Mater. Chem. C* **2017**, *5*, 8819–8827.
9. Pazoki, M.; Edvinsson, T. Metal Replacement in Perovskite Solar Cell Materials: Chemical Bonding Effects and Optoelectronic Properties. *Sustain. Energy Fuels.* **2018**, *2*, 1430–1445.
10. Li, W. G.; Rao, H. S.; Chen, B. X.; Wang, X. D.; Kuang, D. B. A Formamidinium–Methylammonium Lead Iodide Perovskite Single Crystal Exhibiting Exceptional Optoelectronic Properties and Long-Term Stability. *J. Mater. Chem. A* **2017**, 5, 19431–19438.
11. Abdi-Jalebi, M.; Andaji-Garmaroudi, Z.; Pearson, A. J.; Divitini, G.; Cacovich, S.; Philippe, B.; Rensmo, H.; Ducati, C.; Friend, R. H.; Stranks, S. D. Potassium- and Rubidium-Passivated Alloyed Perovskite Films: Optoelectronic Properties and Moisture Stability. *ACS Energy Lett*. **2018**, *3*, 2671–2678.
12. Li, X.; Hoffman, J. M.; Kanatzidis, M. G. The 2D Halide Perovskite Rulebook: How the Spacer Influences Everything from the Structure to Optoelectronic Device Efficiency. *Chem. Rev*. **2021**, *121*, 2230–2291.
13. Nagane, S.; Ghosh, D.; Hoye, R. L. Z.; Zhao, B.; Ahmad, S.; Walker, A. B.; Islam, M. S.; Ogale, S.; Sadhanala, A. Lead-Free Perovskite Semiconductors Based on Germanium–Tin Solid Solutions: Structural and Optoelectronic Properties. *J. Phys. Chem. C* **2018**, *122*, 5940–5947.
14. Ren, X.; Yang, Z.; Yang, D.; Zhang, X.; Cui, D.; Liu, Y.; Wei, Q.; Fan, H.; Liu, S. (Frank). Modulating Crystal Grain Size and Optoelectronic Properties of Perovskite

Films for Solar Cells by Reaction Temperature. *Nanoscale* **2016**, *8*, 3816-3822.

15. Chen, J.; Zhou, S.; Jin, S.; Li, H.; Zhai, T. Crystal Organometal Halide Perovskites with Promising Optoelectronic Applications. *J. Mater. Chem. C* **2016**, 4, 11–27.
16. Zhao, Y.; Zhu, K. Organic–Inorganic Hybrid Lead Halide Perovskites for Optoelectronic and Electronic Applications. *Chem. Soc. Rev*. **2016**, *45*, 655–689.
17. Mondal, N.; Samanta, A. Complete Ultrafast Charge Carrier Dynamics in Photo-Excited All-Inorganic Perovskite Nanocrystals ($CsPbX_3$). *Nanoscale* **2017**, *9*, 1878-1885.
18. Song, Z.; Shrestha, N.; Watthage, S. C.; Liyanage, G. K.; Almutawah, Z. S.; Ahangharnejhad, R. H.; Phillips, A. B.; Ellingson, R. J.; Heben, M. J. Impact of Moisture on Photoexcited Charge Carrier Dynamics in Methylammonium Lead Halide Perovskites. *J. Phys. Chem. Lett*. **2018**, *9*, 6312–6320.
19. Meng, J.; Lan, Z.; Abdellah, M.; Yang, B.; Mossin, S.; Liang, M.; Naumova, M.; Shi, Q.; Gutierrez Alvarez, S. L.; Liu, Y.; Lin, W.; Castelli, I. E.; Canton, S. E.; Pullerits, T.; Zheng, K. Modulating Charge-Carrier Dynamics in Mn-Doped All-Inorganic Halide Perovskite Quantum Dots through the Doping-Induced Deep Trap States. *J. Phys. Chem. Lett*. **2020**, *11*, 3705–3711.
20. deQuilettes, D. W.; Jariwala, S.; Burke, S.; Ziffer, M. E.; Wang, J. T. W.; Snaith, H. J.; Ginger, D. S. Tracking Photoexcited Carriers in Hybrid Perovskite Semiconductors: Trap-Dominated Spatial Heterogeneity and Diffusion. *ACS Nano* **2017**, *11*, 11488–11496.
21. Shahjahan, M. D.; Okamoto, T.; Chouhan, L.; Sachith, B. M.; Pradhan, N.; Misawa, H.; Biju, V. Halide Perovskite Single Crystals and Nanocrystal Films as Electron Donor-Acceptor Heterojunctions. *Angew. Chem. Int. Edit*. **2022**, *62*, e202215947.

22. Ghimire, S.; Khatun, M. F.; Sachith, B. M.; Okamoto, T.; Sobhanan, J.; Subrahmanyam, C.; Biju, V. Highly Luminescent and Stable Halide Perovskite Nanocrystals by Interfacial Defect Passivation and Amphiphilic Ligand Capping. *ACS Appl. Mater. Interfaces* **2023**, *15*, 41081–41091.

23. Okamoto, T.; Shahjahan, Md.; Biju, V. Shape-Dependent Kinetics of Halide Vacancy Filling in Organolead Halide Perovskites. *Adv. Opt. Mater*. **2021**, *9*, 2100355.

24. Tan, Z. K.; Moghaddam, R. S.; Lai, M. L.; Docampo, P.; Higler, R.; Deschler, F.; Price, M.; Sadhanala, A.; Pazos, L. M.; Credgington, D.; Hanusch, F.; Bein, T.; Snaith, H. J.; Friend, R. H. Bright Light-Emitting Diodes Based on Organometal Halide Perovskite. *Nat. Nanotech.* **2014**, *9*, 687–692.

25. Chen, W.; Huang, Z.; Yao, H.; Liu, Y.; Zhang, Y.; Li, Z.; Zhou, H.; Xiao, P.; Chen, T.; Sun, H.; Huang, J.; Xiao, Z. Highly Bright and Stable Single-Crystal Perovskite Light-Emitting Diodes. *Nat. Photon*. **2023**, *17*, 401–407.

26. Yang, J. N.; Chen, T.; Ge, J.; Wang, J. J.; Yin, Y. C.; Lan, Y. F.; Ru, X. C.; Ma, Z. Y.; Zhang, Q.; Yao, H. B. High Color Purity and Efficient Green Light-Emitting Diode Using Perovskite Nanocrystals with the Size Overly Exceeding Bohr Exciton Diameter. *J. Am. Chem. Soc*. **2021**, *143*, 19928–19937.

27. Liang, D.; Peng, Y.; Fu, Y.; Shearer, M. J.; Zhang, J.; Zhai, J.; Zhang, Y.; Hamers, R. J.; Andrew, T. L.; Jin, S. Color-Pure Violet-Light-Emitting Diodes Based on Layered Lead Halide Perovskite Nanoplates. *ACS Nano* **2016**, *10*, 6897–6904.

28. Zhang, Z.; Sun, L.; Devakumar, B.; Liang, J.; Wang, S.; Sun, Q.; Dhoble, S. J.; Huang, X. Novel Highly Luminescent Double-Perovskite $Ca_2GdSbO_6:Eu^{3+}$ Red Phosphors with High Color Purity for White LEDs: Synthesis, Crystal Structure, and Photoluminescence Properties. *J. Lumin.* **2020**, *221*, 117105.

29. Fan, F.; Zhao, L.; Shang, Y.; Liu, J.; Chen, W.; Li, Y. Thermally Stable Double-Perovskite $Ca^{3+}TeO_6:Eu^{3+}$ Red-Emitting Phosphors with High Color Purity. *J. Lumin*. **2019**, *211*, 14–19.

30. Wang, K.-H.; Peng, Y.; Ge, J.; Jiang, S.; Zhu, B.-S.; Yao, J.; Yin, Y.-C.; Yang, J.-N.; Zhang, Q.; Yao, H.-B. Efficient and Color-Tunable Quasi-2D $CsPbBr_xCl_{3-x}$ Perovskite Blue Light-Emitting Diodes. *ACS Photonics* **2019**, *6*, 667–676.

31. Deng, W.; Huang, L.; Xu, X.; Zhang, X.; Jin, X.; Lee, S. T.; Jie, J. Ultrahigh-Responsivity Photodetectors from Perovskite Nanowire Arrays for Sequentially Tunable Spectral Measurement. *Nano Lett*. **2017**, *17*, 2482–2489.

32. Pathak, S.; Sakai, N.; Wisnivesky Rocca Rivarola, F.; Stranks, S. D.; Liu, J.; Eperon, G. E.; Ducati, C.; Wojciechowski, K.; Griffiths, J. T.; Haghighirad, A. A.; Pellaroque, A.; Friend, R. H.; Snaith, H. J. Perovskite Crystals for Tunable White Light Emission. *Chem. Mater.* **2015**, *27*, 8066–8075.

33. Qin, Z.; Song, D.; Xu, Z.; Qiao, B.; Huang, D.; Zhao, S. Filterless Narrowband Photodetectors Employing Perovskite/Polymer Synergetic Layers with Tunable Spectral Response. *Org. Electron.* **2020**, *76*, 105417.

34. Yang, C.; Zhuang, B.; Lin, J.; Wang, S.; Liu, M.; Jiang, N.; Chen, D. Ultrastable Glass-Protected All-Inorganic Perovskite Quantum Dots with Finely Tunable Green Emissions for Approaching Rec. 2020 Backlit Display. *Chem. Eng. J.* **2020**, *398*, 125616.

35. Kulkarni, S. A.; Mhaisalkar, S. G.; Mathews, N.; Boix, P. P. Perovskite Nanoparticles: Synthesis, Properties, and Novel Applications in Photovoltaics and LEDs. *Small Methods* **2019**, *3*, 1800231.

36. Sun, Y.; Ge, L.; Dai, L.; Cho, C.; Ferrer Orri, J.; Ji, K.; Zelewski, S. J.; Liu, Y.;

Mirabelli, A. J.; Zhang, Y.; Huang, J.-Y.; Wang, Y.; Gong, K.; Lai, M. C.; Zhang, L.; Yang, D.; Lin, J.; Tennyson, E. M.; Ducati, C.; Stranks, S. D.; Cui, L.-S.; Greenham, N. C. Bright and Stable Perovskite Light-Emitting Diodes in the near-Infrared Range. *Nature* **2023**, *615*, 830–835.

37. Ren, X.; Hu, H. L.; Chen, Z. Y.; Gao, L. X.; Hao, H.; Liu, Y.; Jiang, F. L. Highly Stable Perovskite Nanocrystals with Pure Red Emission for Displays. *ACS Appl. Nano Mater*. **2023**, *6*, 6092–6102.
38. Holzwarth, A. R. Time-Resolved Fluorescence Spectroscopy. *Methods In Enzymology*. **1995**, *246*, 334-362.
39. Stolow, A.; Bragg, A. E.; Neumark, D. M. Femtosecond Time-Resolved Photoelectron Spectroscopy. *Chem. Rev*. **2004**, *104*, 1719–1758.
40. Suhling, K.; French, P. M. W.; Phillips, D. Time-Resolved Fluorescence Microscopy. *Photochem. Photobiol. Sci.* **2005**, *4*, 13–22.
41. Van Stokkum, I. H. M.; Larsen, D. S.; Van Grondelle, R. Global and Target Analysis of Time-Resolved Spectra. *Biochim. Biopyhs. Acta*. **2004**, *1657*, 82–104.
42. Yang, B.; Han, K. Charge-Carrier Dynamics of Lead-Free Halide Perovskite Nanocrystals. *Acc. Chem. Res*. **2019**, *52*, 3188–3198.
43. Herz, L. M. Charge-Carrier Dynamics in Organic-Inorganic Metal Halide Perovskites. Annu. *Rev. Phys. Chem.* **2016**, *67*, 65–89.
44. Zhan, J.; Li, M.; Zhou, Z. Effective Surface Passivation via Intermolecular Interactions for High-Performance Perovskite Solar Cells. *Solar RRL* **2022**, *6*, 2200082.
45. Qiu, C.; Lin, X.; Wang, Y.; Feng, G.; Ling, C.; Liu, J.; Du, J.; Xiao, X.; Wang, X.; Zeng, P.; Liu, M.; Liang, W.; Hu, Y.; Han, H. Exploring the Charge Dynamics and

Energy Loss in Printable Mesoscopic Perovskite Solar Cells. *Adv. Energy Mater*. **2022**, *12*, 2202813.

46. Chouhan, L.; Ito, S.; Thomas, E. M.; Takano, Y.; Ghimire, S.; Miyasaka, H.; Biju, V. Real-Time Blinking Suppression of Perovskite Quantum Dots by Halide Vacancy Filling. *ACS Nano* **2021**, *15*, 2831–2838.
47. Aydin, E.; De Bastiani, M.; De Wolf, S. Defect and Contact Passivation for Perovskite Solar Cells. *Adv. Mater.* **2019**, *31*, 1900428.
48. Bhagyalakshmi, S. B.; Zhang, D.; Biju, V. Electroluminescence of Halide Perovskite Single Crystals Showing Stochastically Active Multiple Emitting Centers. *J. Phys. Chem. C* **2022**, *126*, 17826-17835.
49. Qiu, L.; He, S.; Ono, L. K.; Qi, Y. Progress of Surface Science Studies on ABX_3 -Based Metal Halide Perovskite Solar Cells. *Adv. Energy Mater.* **2020**, *10*, 1902726.
50. Ono, L. K.; Liu, S. (Frank); Qi, Y. Reducing Detrimental Defects for High-Performance Metal Halide Perovskite Solar Cells. *Angew. Chem. Int. Ed*. **2020**, *59*, 6676–6698.
51. Li, B.; Ferguson, V.; Silva, S. R. P.; Zhang, W. Defect Engineering toward Highly Efficient and Stable Perovskite Solar Cells. *Adv. Mater. Interace* **2018**, *5*, 1800326.
52. Ghosh, S.; Shi, Q.; Pradhan, B.; Mushtaq, A.; Acharya, S.; Karki, K. J.; Pullerits, T.; Pal, S. K. Light-Induced Defect Healing and Strong Many-Body Interactions in Formamidinium Lead Bromide Perovskite Nanocrystals. *J. Phys. Chem. Lett*. **2020**, *11*, 1239–1246.
53. Ghosh, S.; Pal, S. K.; Karki, K. J.; Pullerits, T. Ion Migration Heals Trapping Centers in $CH_3NH_3PbBr_3$ Perovskite. *ACS Energy Lett*. **2017**, *2*, 2133–2139.

General conclusions

In this thesis, I studied the size-, shape- and quality-controlled synthesis of $MAPbBr_3$ microcrystals using additives. First, I synthesized crystals at various CHP concentrations to understand the role of additive ratio effects on the crystal size, density, shape, and quality. Also, the temperature-dependent crystal size, shape, and density were studied by synthesizing crystals at various temperatures with a constant CHP concentration. The results showed a high CHP concentration and reaction temperature, which helped to obtain isotropic and high-quality crystals. This is due to the high CHP concentration and temperature, creating a slow crystallization condition, which leads to a slow nucleation speed and forms less defective uniformly sized and shaped crystals.

To study the light-soaking effect on the electroluminescence blinking and photoluminescence decay. I prepared the perovskite $MAPbBr_3$ microcrystals directly on ITO using the blade-coating method at room temperature. For the study of light-soaking on electroluminescence blinking and photoluminescence lifetime, the crystals were irradiated by 470-490 nm light and 405 nm LED, respectively. The photoluminescence decay profile is obtained, and the lifetime is calculated. The results show that PL lifetime is increased under light-soaking. The electroluminescence blinking ON and OFF probability distribution plot is prepared from three periods: before light-soaking, during light-soaking, and after light-soaking, and analyzed for over 100 blinking single crystals. The results show that the ON probability and ON time are increased, and the OFF probability and OFF time are decreased at the light-soaking period compared with the initial non-light-soaking period. The second non-light-soaking period shows a recovery effect after light-soaking. The ON probability and ON time, OFF probability, and OFF time recover to the values before light soaking. These effects are attributed to the light-induced halide ion migration from the interstitial position to halide vacancies and the trap healing by the migrated halide ions.

For the time-resolved electroluminescence of $MAPbBr_3$ microcrystals study, I prepared the $MAPbBr_3$ microcrystals directly on ITO at room temperature. To confirm the instrument's reliability, first, I measured the electroluminescence spectra and decay of commercial blue-, green-, and red-colored LEDs. To obtain the time-resolved electroluminescence decay of $MAPbBr_3$ MCs, I used the function generator as the electrical excitation power source to replace the picosecond laser. To study the role of halide ion vacancies on the electroluminescence spectra and decay, photoluminescence spectra and decay for $MAPbBr_3$ MCs, I performed the real-time and post-synthesis treatment of $MAPbBr_3$ MCs with MABr. The results showed both photoluminescence and electroluminescence lifetime enhancement and an increase in photoluminescence and electroluminescence intensity by the MABr solution treatment. The main reason for such decay elongation and luminescence enhancement is attributed to the halide ion vacancy filling by MABr. As a result, the halogen-vacancy-assisted carrier trapping and de-trapping processes could be suppressed, and I improved the quality of $MAPbBr_3$ MCs.

List of achievements

Publications

1. Thermodynamically and Kinetically Controlled Nucleation and Growth of Halide Perovskite Single Crystals.

   Zhang, D.; Okamoto, T.; Biju, V. *Small* **2023**, 2304900.

2. Electroluminescence of Halide Perovskite Single Crystals Showing Stochastically Active Multiple Emitting Centers.

   Bhagyalakshmi, S. B.; **Zhang, D**.; Biju, V. *J. Phys. Chem. C* **2022**, *126*, 17826−17835.

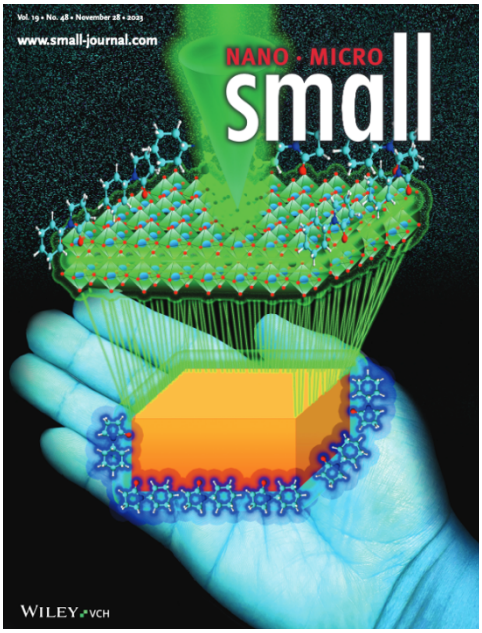

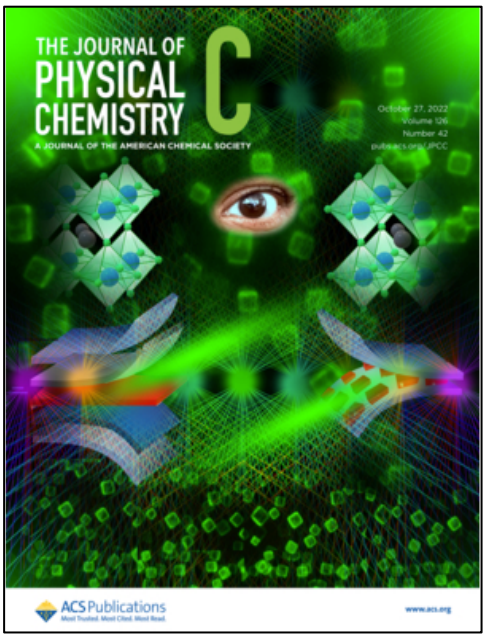

Presentations

1. Thermodynamically Controlled Nucleation and Growth of Halide Perovskite Single Crystals

   Dong Zhang, Takuya Okamoto, Vasudevanpillai Biju.

   Annual Meeting of the Japan Chemical Society of Japan, oral, Sep, 2023.

2. Thermodynamically and kinetically controlled nucleation and growth of halide perovskite single crystals

   Dong Zhang, Takuya Okamoto, Vasudevanpillai Biju.

   The 31st International Conference on Photochemistry, poster, July, 2023.

3. Homogeneous $MAPbBr_3$ Microcrystals Prepared by Controlling the Crystal Growth Thermodynamics

   Dong Zhang, Takuya Okamoto, Vasudevanpillai Biju.

   The Chemical Society of Japan Hokkaido Branch 2023 Winter Research Presentation, oral, Jan, 2023.

4. Optimizing halide perovskite microcrystal shape, dispersion, and optical properties

   Dong Zhang, Takuya Okamoto, Vasudevanpillai Biju.

   The Chemical Society of Japan Hokkaido Branch 2022 Summer Research Presentation, poster, July, 2022.

5. Roles of Additives and Solvent in the Formation of Homogeneous $MAPbBr_3$ Microcrystals

   Dong Zhang, Takuya Okamoto, Vasudevanpillai Biju.

   The 23rd RIES-Hokudai International Symposium, oral, Dec, 2022.

6. Size-controlled synthesis of $MAPbBr_3$ perovskite microcrystals and their optical

properties.

Dong Zhang, Takuya Okamoto, Vasudevanpillai Biju.

The 30st International Conference on Photochemistry, poster, Sep, 2022.

7. Optimizing single crystal-perovskite sizes, shapes, and their roles on electroluminescence blinking

Dong Zhang, Takuya Okamoto, Vasudevanpillai Biju.

Annual Meeting of the Japan Chemical Society of Japan, oral, Mar, 2022.

8. Optimizing single crystal perovskite sizes, shapes, and charge carrier properties for electroluminescence application

Dong Zhang, Takuya Okamoto, Vasudevanpillai Biju.

The Chemical Society of Japan Hokkaido Branch 2022 Winter Research Presentation, poster, Jan, 2022.

9. Homogenous size and shape $MAPbBr_3$ microcrystals and their optical properties

Dong Zhang, Takuya Okamoto, Vasudevanpillai Biju.

22nd RIES-Hokudai International Symposium, poster, Dec, 2021.